Universität Rostock Traditio et Innovatio

Molecular spectroscopy from far-field matter-wave interferometry

Dissertation

zur

Erlangung des akademischen Grades

doctor rerum naturalium (Dr. rer. nat.)

der Mathematisch-Naturwissenschaftlichen Fakultät

der Universität Rostock

vorgelegt von

Dipl.-Phys. Johannes Fiedler

urn:nbn:de:gbv:28-diss2017-0161-6

Gutachter:

1. Gutachter:

Prof. Dr. Stefan Scheel,

Institut für Physik, Universität Rostock

2. Gutachter:

Prof. Dr. Akbar Salam,

Chemistry Department, Wake Forest University

Datum der Einreichung: 29. Mai 2017

Datum der Verteidigung: 26. Oktober 2017

Contents

chapter 1

Introduction

Historical marks on matter–wave interferometry

Until the end of the eighteenth century, two different and independent descriptions were known for physical objects, the particle and the wave pictures. Depending on the problem, one had to choose which method will be useful. The motion of particles can be determined using Newton's equations of motion. The solutions of Newton's equations are trajectories that the particle moves along. This point of view is the cornerstone of the corpuscular hypothesis that traces back to Sir Isaac Newton.

In contrast, the behaviour of waves is determined by different laws, for example electromagnetic waves follow Maxwell's equations. There are two effects that appear when dealing with waves. On the one hand, a wave can be diffracted at a physical barrier, which means that a wave can reach positions located in the geometrical shadow. These points are unreachable for particles described by Newton's equations. On the other hand, waves can interfere with one another, meaning that their respective amplitudes can add coherently. The result can be an amplification or a reduction of the wave amplitude, depending on their relative phase. This perspective is known as wave theory and was mainly represented by Christiaan Huygens and Joseph von Fraunhofer.

Strong support for the wave nature of light was given by the double-slit experiment by Thomas Young in 1807 [TY1807]. Further evidence for the wave picture was provided by Dominique-François-Jean Arago in 1818, who showed that light could illuminate regions behind objects that particles cannot penetrate. This effect is today known as Arago- or Poisson spot.

A rethink of this strict separation had to happen in order to explain the photoelectric effect. This effect was first measured by H. Hertz [HH1887] in 1887, who illuminated a metallic surface with ultraviolet light and observed that electrons were ejected from the surface. The physical explanation was given by A. Einstein only in 1905 [AE1905], who suggested that light behaves as a particle as well as a wave [AE1905]. Einstein's description of the photoelectric effect defined the starting point of quantum mechanics. Another cornerstone in the development of quantum mechanics was the explanation of blackbody radiation by M. Planck in 1900 [MP1900]. His idea was to consider the mode density of the electromagnetic fields inside a blackbody of finite size with the assumption that the mode energies are proportional to the frequency $E_n = hf_n = hc/\lambda_n$, where h denotes the Planck constant (Planck denoted this quantity as "Hilfsgröße"). In order to satisfy the boundary conditions at the surfaces of the blackbody, only a discrete set of wavenumbers can exist; $\lambda_n = n\lambda_0$.

Quantum mechanics stipulates that particles also have a wave nature and can thereby build up interference. The de Broglie wavelength connects the property of the particle, its momentum p, with a wavelength [LdB1923] $\lambda = h/p$. This relation has a wide range of applications. For example, as the resolution of a microscope is limited by the wavelength used due to the Abbe limit[1] [EA1873], a new source of radiation with shorter wavelength was necessary. This led to the development of the electron microscope by E. Ruska and M. Knoll in 1931 [ER32]. Because of the wave-particle duality, accelerated electrons with momentum p correspond to a wave with wavelength $\lambda = h/p$.

The visible range of the electromagnetic spectrum is between 380 and 780 nm and hence the resolution of an optical microscope is in the same range. By the use of electrons, a resolution of a few picometers can be achieved [ERKD09]. The De Broglie wavelength is inversely proportional to the momentum of the particle. A typical transmission electron microscope has a voltage source in the range of 100 to 300 kV, which yields a wavelength of around $\lambda = 2 \cdots 4\,\mathrm{pm}$. It is interesting to ask if the de Broglie relation is also valid for particles with larger mass m, for example a tennis ball. It has a mass of about 57 g and can be accelerated up to a velocity of about $200\,\mathrm{km\,h^{-1}}$. This yields a de Broglie wavelength of $\lambda \approx 2 \cdot 10^{-34}\,\mathrm{m}$. The fundamental question is whether a particle shows interference at this length scale.

The first experimental verification of wave-particle duality via double slit experiments with electrons was performed in 1927 by C. Davisson and L.H. Germer.

[1] A optical microscope with a resolution below the Abbe limit was reached in 2006 by E. Betzig *et al.* using photoactivated localization microscopy [EB06, SH08, WM1989]. E. Betzig, S. Hell and W.E. Moerner received the Nobel Prize in chemistry in 2014 for their development.

After that, experiments with increasing particle mass started with the interference of atoms by I. Estermann and O. Stern [OS30] and of neutrons in 1936 [HP1936]. The next big step in increasing the mass of the particles ensued in 1999 in the group of Anton Zeilinger at the University of Vienna, where the interference of fullerenes, C_{60} with a mass of 720 atomic mass units (a.m.u.) was shown [MA99]. From then on, the development of sources, detectors and even diffraction gratings continued, until recently the interference of particles with a mass of up to 10,000 a.m.u. was shown [SE13]. Until now, a limit at which quantum mechanics fails to hold has not been found, hence the development of new interference experiments still continues.

However, interference of truly macroscopic objects has not been observed yet. The reason is that the increasing number of degrees of freedom results in a stronger coupling with the environment that destroys the interference. This effect is known as decoherence. Coherence is the ability of a wave to build interference. In quantum mechanics an interference pattern of a double slit experiment can be destroyed by extracting the information of the path chosen by the particle. This means that a measurement of the grating opening, where the particle passes the grating, results in an incoherent interference pattern. Even the mere possibility of retrieving this information provides a source of decoherence. Several experiments have studied the impact of decoherence of matter waves. An example is the electron beam experiment by F. Hasselbach [FH10]. There, an electron beam is diffracted at a biprism. The interfering waves pass a metallic surface, where they induce image currents. By measuring these currents a localisation of the electrons is possible, which leads to decoherence. This effect can be measured by imaging the interference patterns and with closer distances to the surface, the interference fringes wash out.

In an interference experiment with particles the interaction between them and the scattering object has to be taken into account. For example, the relevant interaction between neutral particles and a dielectric grating is the Casimir–Polder force, which is caused by the fluctuations of the ground-state electromagnetic field and occurs when a neutral and polarisable particle comes close to a dielectric surface. This description is firmly rooted in the particle picture. However, the Casimir–Polder interaction then influences the propagation of the matter wave and is imprinted in the interference pattern.

Structure of the thesis

The thematic priority of this thesis is the theoretical description of a typical matter-wave interference experiment. In analogy to interference experiments with light, we assume that a particle beam consisting of neutral and spatially extended particles is created at

a source, accelerated towards a dielectric scatterer and measured at a screen. Due to the choice of neutral particles, the Casimir–Polder interaction plays an important role in such experiments. Thus, we will investigate the impact of the Casimir–Polder interaction on the matter wave, in particular on the interference pattern.

The Casimir–Polder force is a fundamental quantum electrodynamical force. It arises when a polarisable particle comes close to a dielectric surface [CP1948]. In such a case, the ground state fluctuations of the electromagnetic field induce a dipole moment in the particle which then interacts with the dielectric surface by inducing an image dipole. Due to the Coulomb force both dipoles attract each other. Calculations on this fundamental force are not easy to handle, because it involves an enormous amount of information. The complete optical properties of the particle, i.e. the polarisability, are needed, which defines a quantum molecular dynamics problem. The optical response of the macroscopic object has to be taken into account, which is a challenge for solid-state physics in terms of its geometry and optical response. In addition, the geometric shape of the object enters this interaction as a classical scattering problem. All these properties have to be completely known for the calculation of the Casimir–Polder force. Until now, methods only exist for the estimation of simple geometries, such as spheres, infinite cylinders, planar and layered media. In the established theory [SB08, SYB12-I, SYB12-II], a particle is treated as the point-like object, an approximation that fails for extended molecules at very short distances from a surface. The effect of finite temperature is also known [SYB12-II]. This enters the theory via thermally populated particle states and via an environmental temperature.

In order to describe such an interference experiment, we will introduce a method for estimating the scattering properties of a thick, periodic grating by using the Born series expansion of the Green tensor as the fundamental solution of the classical scattering problem. We will analyse the finite-size effects of a molecule and present calculations for an extended and rotating molecule and calculate the influence of this on the interference pattern. We will discuss under which circumstances a rotational averaging or an incoherent superposition of rotational states is appropriate.

The thesis is structured as follows. We will introduce the theoretical description of matter-wave interference experiments, including the description of scattering processes, in chapter 2, and we will present the theory of Casimir–Polder forces in chapter 3. The Born series expansion, which is a method for describing the electromagnetic scattering of a macroscopic object, will be discussed for thick gratings in chapter 4. There, we will introduce a local-field correction method to partially incorporate higher orders in the expansion. The Born series expansion is then used to explain atom-surface reflection data, obtained by the group of Sebastian Slama at the University of Tübingen.

In chapter 5, the theory of Casimir–Polder potentials for extended and rotating molecules is developed. Here, we construct a method to obtain the Casimir–Polder potential of large molecules using a spatially-distributed polarisability.

In chapter 6, we apply this theory to the interference of large organic molecules at dielectric gratings, and compare with experimental data obtained by the group of Markus Arndt at the University of Vienna.

Finally in chapter 7, we will present a possible reconstruction method for the Casimir–Polder potential and the molecular polarisability based on the interference pattern. Here, we will introduce a novel measurement scheme to estimate the spatial phase distribution of the matter wave based on the concept of a Hartmann–Shack sensor. For the determination of the Casimir–Polder potential, we will present an experimentally-realisable tomographic reconstruction method and we combine both methods to show how optical properties such as the molecular polarisability can be retrieved from an interference pattern.

In chapter 8, we give a summary and an outlook towards open questions.

chapter 2

The scattering process of the matter wave

An important aspect of the experiments on matter-wave interference is their diffraction on the grating which can be treated as a scattering process. The scattered wave encodes information about the interaction of the matter wave with the dielectric gratings in the form of the interference pattern. In this chapter, we give a detailed solution of this scattering problem.

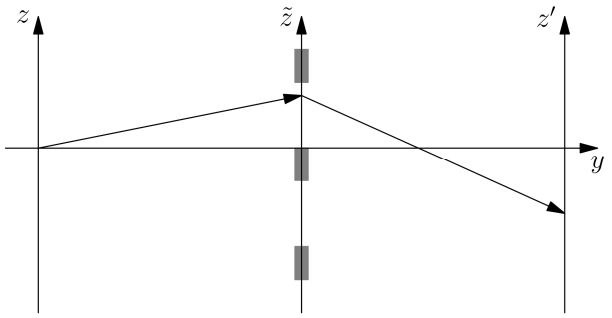

Figure 2.1: Sketch of the scattering on a grating with the propagation direction y and the source plane (x, z), the scattering plane $(\tilde{x}, \tilde{z})$ and the image plane (x', z').

The description of the scattering process will be presented in three different ways. The first is purely quantum mechanical, analysing the quantum behaviour of a single particle inside a Casimir–Polder potential. It uses scattering theory and solves the Schrödinger equation of a particle in a potential. We will focus on the scattering at a point-like body to show the principal behaviour of the interaction potential. Thereafter, a short introduction of the established description of the matter-wave scattering via transversal Wigner functions [EPW1932, WS01] will be discussed. The final approach, which is commonly used for the estimation of the interference pattern, is based on Kirchhoff's diffraction integral, which uses the de Broglie relation to match a wave vector to the matter wave and, consequently, to solve the scattering problem in analogy to classical optics.

Figure 2.1 illustrates a typical diffraction problem. We consider wave propagation

along the y-axis. The arrows illustrate a possible optical path from the source $(0, 0)$ via a point inside the scattering plane to a final point at the screen. The sum over all possible optical paths will yield the interference pattern. We restrict ourselves to a purely coherent superposition and do not contemplate decoherence effects.

2.1 Quantum mechanical approach

The starting point for the description of a scattering process is the time-dependent SCHRÖDINGER equation, which reads in real space [AM14]

$$i\hbar\frac{\partial}{\partial t}\psi(\mathbf{r},t) = -\frac{\hbar^2}{2m}\Delta\psi(\mathbf{r},t) + V(\mathbf{r})\psi(\mathbf{r},t)\,, \tag{2.1}$$

with the time-independent interaction potential $V(\mathbf{r})$. The wavefunction $\psi(\mathbf{r},t)$ describes the probability to find a particle of the matter wave at the point $\mathbf{r}$ at the time t. To solve this equation, an initial condition is needed. Here, a plane wave is used. It is useful to separate the wave equation with respect to amplitude and phase by writing $\psi = A\mathrm{e}^{i\varphi}$, $A, \varphi \in \mathbb{R}$. The SCHRÖDINGER equation separates into a system of two coupled differential equations for the amplitude and the phase

$$\dot{A} = -\frac{\hbar}{2m}\left(2\,\mathbf{grad}\,A\cdot\mathbf{grad}\,\varphi + A\Delta\varphi\right)\,, \tag{2.2}$$

$$\hbar A\dot{\varphi} = \frac{\hbar^2}{2m}\left(\Delta A - A\left[\mathbf{grad}\,\varphi\right]^2\right) - V(\mathbf{r})A\,, \tag{2.3}$$

respectively. Assuming a large distance between the source and the scattering object leads to a plane wave in front of the scatterer. This assumption implies that the gradient of the phase can be neglected, which results in the differential equation for the phase

$$\dot{\varphi} = -\frac{\hbar}{2m}\frac{\Delta A}{A} - \frac{V(\mathbf{r})}{\hbar}\,, \tag{2.4}$$

where the first term corresponds to the geometric phase, which is accumulated by the free propagation, and the second term corresponds to the phase shift accumulated by the interaction with the potential. Therefore, the total phase shift corresponding to the interaction can be obtained by integration over the interaction potential

$$\varphi(\mathbf{r}) = -\frac{1}{\hbar}\int V\left[\mathbf{r}(t)\right]\mathrm{d}t\,, \tag{2.5}$$

which has to be read as an integral over all trajectories. In this connection, the eikonal (or paraxial) approximation is often used, which means that the particle does not move along the transversal direction. It passes the scatterer along straight lines and accumulates only a phase shift. This assumption means that the temporal integral can be rewritten as a spatial integral

$$\varphi(\mathbf{r}) = -\frac{1}{\hbar}\int V\left(\mathbf{r}(t)\right)\mathrm{d}t \approx -\frac{1}{\hbar v_\parallel}\int V(\mathbf{r})\mathrm{d}\mathbf{r}_\parallel\,, \tag{2.6}$$

with the longitudinal velocity $v_{\parallel}$. This result provides the connection of the interaction potential which is given in the particle picture and the wave propagation in the wave picture. Second, by assuming the eikonal approximation, the thickness of the grating is impressed in the integral and leads a projection of the scatterer onto the scattering plane.

2.2 Transverse Wigner function

Figure 2.2 shows the typical measuring configuration for molecular diffraction. From an incoherent source S the molecules are sent to a grating. The WIGNER function is defined by the following expectation value of the density operator $\hat{\varrho}$ [EPW1932, WS01]

$$w\left(z,p_z\right)=\frac{1}{2\pi\hbar}\int \mathrm{e}^{i\frac{p_z s}{\hbar}}\left\langle z-\frac{s}{2}\right|\hat{\varrho}\left|z+\frac{s}{2}\right\rangle \mathrm{d}s\,, \tag{2.7}$$

and is a quasiprobability function that depends on the phase-space coordinates. Here, only its transversal part (in z-direction) appears, i.e. the phase space coordinate z and its corresponding momentum p_z. The WIGNER function is a real function, whose marginals are (proper) probability distributions

$$\int_{-\infty}^{\infty} w(z,p)\,\mathrm{d}p=\langle z|\,\hat{\varrho}\,|z\rangle\ ,\quad \int_{-\infty}^{\infty} w(z,p)\,\mathrm{d}z=\langle p|\,\hat{\varrho}\,|p\rangle\ . \tag{2.8}$$

Returning to the scattering process, the molecular beam (described by the WIGNER function $w_0(\mathbf{q},\mathbf{p})$)[1] will be sent to a first grating G_1, which collimates the molecules directed towards the second grating G_2. There are two ways to ensure that the molecules form a plane wave in front of the second grating. One is to increase the distance between the first and the second grating, L_1, in a way that G_2 is located in the far-field of the first grating. The other method applies to the near field regime and is to perform

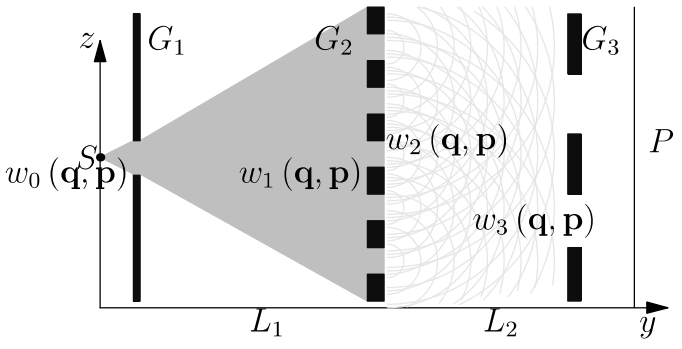

Figure 2.2: Sketch of the transmission through the gratings, with the collimission grating G_1, the transmission grating G_2, the source S, the screen P and the WIGNER function w_i at the initial point ($i=0$) before and after the transmission grating $i=1$ and $i=2$, respectively and in front of the screen ($i=3$).

[1] The transversal coordinates $\mathbf{q}$ and momenta $\mathbf{p}$ are two-dimensional vectors, $\mathbf{q}=(q_x,q_z)$ and $\mathbf{p}=(p_x,p_z)$. For simplicity we consider only the z- and p_z-components.

a velocity selection of the molecules and to move the source S into the TALBOT length from the first grating, [BW99]. This leads to the TALBOT–LAU interferometry [BB02].

A phase shifted and discontinuous wavefront, represented by the WIGNER function $w_2(\mathbf{q}, \mathbf{p})$, exits from this grating, which propagates towards the third grating G_3 and interferes with itself during this propagation. This third grating is only needed in case of heavy molecules or in the near-field regime, because then the emerging interference patterns are so small that they cannot be resolved at the screen. The periodicity of the third grating is equal to the periodicity of the expected interference pattern of the matter wave. By spatially shifting this grating, the interference pattern will be scanned. We consider the far-field regime for our investigations, in which the grating G_3 is redundant. A second consequence of the far-field regime is that the first grating for the beam collimation is not needed either, as due to the large distance between the source and the transmission grating L_1, every incoherent wave becomes approximately a plane wave.

In this section, the formalism using transverse WIGNER functions will be introduced, based on Ref. [NH08]. The advantage of this formulation is that every optical component, such as free propagation, interaction with a scatterer and so on, will be described by a mathematical operator acting on the WIGNER function. Following this line of thought the complete apparatus can be separated into individual devices. It starts with the initialisation, the source of the matter wave, w_0. After that, the matter wave propagates freely through free space along the distance L_1, which yields the WIGNER function w_1, until it passes through the grating and generates the WIGNER function w_2. These processes are again followed by the free propagation along the distance L_2, which yields the WIGNER function before the measurement w_3. And finally, the measurement takes place, yielding the interference pattern $P(z)$. In the following, each process will be investigated separately.

Free propagation

The free propagation of a particle with mass m in the WIGNER formalism can be calculated by the equation of motion in the absence of forces

$$\frac{\partial w(z,p)}{\partial t} = -\frac{p}{m}\frac{\partial w(z,p)}{\partial z}\,, \tag{2.9}$$

which has the solution [WS01]

$$w_t\,(z,p) = w_{\text{in}}\left(z - \frac{t}{m}p, p\right) = \mathrm{T}_t\, w_{\text{in}}\,(z,p)\ . \tag{2.10}$$

Figure 2.3 illustrates this operation. A GAUSSian distributed initial WIGNER function whose contourplot is depicted by dashed lines, is sheared proportional to the momentum without loss of amplitude by such an operation. This behaviour of the WIGNER function has the following advantage: It can serve as the starting point for the quantum-state reconstruction of the WIGNER function w_2 [VW06], which will be considered in detail in chapter 7.

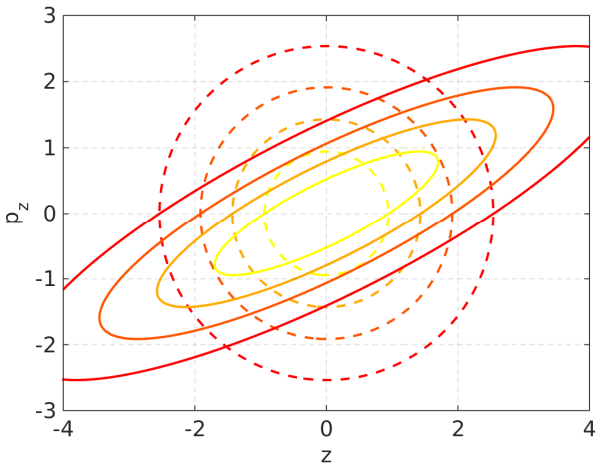

Figure 2.3: Sketch of the WIGNER function before (dashed lines) and after free propagation (solid lines)

The scattering process

In general, the transmission through an arbitrary potential, expressed by the operator $\hat{\mathrm{U}}$, can be described as a convolution [NH08]

$$w_{\mathrm{out}}(z,p) = \int \mathrm{d}z_0 \int \mathrm{d}p_0 K(z,p;z_0,p_0)\, w_{\mathrm{in}}(z_0,p_0) \tag{2.11}$$

with the integral kernel

$$K(z,p;z_0,p_0) = \frac{1}{2\pi\hbar}\int \mathrm{d}s \int \mathrm{d}s' \mathrm{e}^{i\frac{ps+p_0 s'}{\hbar}} \left\langle z-\frac{s}{2}\right| \hat{\mathrm{U}} \left| z_0+\frac{s'}{2}\right\rangle \left\langle z_0-\frac{s'}{2}\right| \hat{\mathrm{U}} \left| z+\frac{s}{2}\right\rangle . \tag{2.12}$$

In case of a grating, the transition matrix element $\langle z|\,\hat{\mathrm{U}}\,|z'\rangle$ can be simplified to $\langle z|\,\hat{\mathrm{U}}\,|z'\rangle = t(z)\,\delta(z-z')$, with a grating transmission function $t(z)$, with $|t(z)| \leq 1$, which is nonzero only in the opening of the grating. Here, we apply the eikonal approximation to reduce the thickness of the grating to its projection onto the scattering plane. The integral kernel decomposes into

$$K(z,p;z_0,p_0) = \delta(z-z_0)\frac{1}{2\pi\hbar}\int \mathrm{d}s\, \mathrm{e}^{is\frac{p-p_0}{\hbar}} t\left(z-\frac{s}{2}\right) t^\star\left(z+\frac{s}{2}\right) . \tag{2.13}$$

The complex transmission function, which is introduced here, can be understood as a product of the classical transmission function $|t(z)|$, varying between 0 and 1 and the phase shift due to the CASIMIR–POLDER potential, Eq. (2.6), yielding

$$t(z) = |t(z)|\,\mathrm{e}^{i\frac{1}{\hbar v}\int U_{CP}(y,z)\mathrm{d}y} . \tag{2.14}$$

As a consequence, the transmission function only depends on the transverse component z, which means that the longitudinal extension of the grating can be neglected and the interaction of the matter wave with the scatterer occurs at a single point. A second aspect of this behaviour is that a rotated grating, as we consider for the reconstruction, yields a marginal distribution of the potential landscape, which results in a RADON transformation for all angles and will be shown in detail in chapter 7.

Measurement

The measurement process at the screen P, which yields the interference pattern $P(z)$, is given by the spatial marginal distribution of the WIGNER function [WS01]

$$P(z) = \int w(z,p)\,\mathrm{d}p\,, \tag{2.15}$$

see Eq. (2.8). Such a marginal distribution is equivalent to a partial trace of the density matrix and is associated with a loss of information. In addition, the probability distribution $P(z)$ means a statistical average over a large number of identically prepared experiments. Hence, a huge number of repetitions are needed [JUA13].

Total propagation through the experimental apparatus

The propagation starts with the initial WIGNER function $w_0(z,p_z)$ propagating to the grating with constant momentum p_y along the distance L_1, which means that the free propagation operator has to be adopted, $w_1(z,p_z) = w_0\left(z - L_1\frac{p_z}{p_y}, p_z\right)$. Next, the wave packet passes the grating and interacts with the CASIMIR–POLDER potential

$$w_2(z,p_z) = \int \mathrm{d}z_0\mathrm{d}p_0\, K(z,p_z,z_0,p_0) w_1(z_0,p_0)\,, \tag{2.16}$$

with the integral kernel defined in Eq. (2.13). The wave packet is spatially split by this interaction, caused by the periodic structure of the grating. The subsequent free propagation over the distance L_2 yields the interference of the split wavepackets, which is again the action of the free propagation operator $w_3(z,p_z) = w_2\left(z - L_2\frac{p_z}{p_y}, p_z\right)$. Eventually, the measurement is described by the projection onto the phase-space coordinate $P(z) = \int \mathrm{d}p_z\, w_3(z,p_z)$.

This method has a more formal character than it is useful for the evaluation of the interference patterns. For calculations of the appearing interference pattern, an estimate of the initial WIGNER function is needed. It is useful for the reconstruction of the WIGNER function w_2, which includes the transverse momentum distribution. However, for calculations of the interference patterns a better approach is KIRCHHOFF's diffraction formula using the wave-particle duality for the estimation of the wave vector.

2.3 Kirchhoff's diffraction

The fundamental concept underlying KIRCHHOFF's diffraction integral is the HUYGENS-FRESNEL principle, which implies that each point of a wave is the starting point of an elementary spherical wave [JDJ02],

$$\psi(\mathbf{r}) \approx \frac{\mathrm{e}^{ikr}}{r}\,, \tag{2.17}$$

with the wavevector $\mathbf{k}$. Figure 2.1 shows the typical arrangement of a scattering experiment with a thin grating. As it was shown above, the thickness of the grating can be neglected and the transmission function only depends on the transverse coordinates, Eq. (2.13). The matter wave propagates along the y-direction, which defines the longitudinal coordinate. It is useful to define three transversal planes orthogonal to this axis, the source plane, denoted by the pair of coordinates (x, z), the object plane $(\tilde{x}, \tilde{z})$, and the screen plane with the primed coordinates (x', z'). The source (a point source) is located at the point (x, z) in the source plane, with the longitudinal coordinate $y = 0$. Now, the spherical wave centred at (x, z) propagates to the object plane at a distance L_1. The wave propagating along an optical path in this plane is given by the spherical wave front

$$\psi(\tilde{x}, \tilde{z}) \approx \frac{\mathrm{e}^{ik\sqrt{L_1^2+(\tilde{x}-x)^2+(\tilde{z}-z)^2}}}{\sqrt{L_1^2+(\tilde{x}-x)^2+(\tilde{z}-z)^2}}\,, \tag{2.18}$$

which denotes the geometric phase of the apparatus, because it is the local phase of the wave at the point $(\tilde{x}, \tilde{z})$ in the object plane. Next, this wave interacts with the grating, which is modelled by a multiplication with the transmission or slit function $t(\tilde{x}, \tilde{z})$. Finally, the wave propagates from the object to the screen plane. Combining all phase distributions, KIRCHHOFF's diffraction formula reads [BW99]

$$P(x', z') = \frac{a_0^2 k^2}{4\pi^2} \times \left| \int t(\tilde{x}, \tilde{z}) \frac{\mathrm{e}^{ik\left(\sqrt{L_1^2+(\tilde{x}-x)^2+(\tilde{z}-z)^2}+\sqrt{L_2^2+(x'-\tilde{x})^2+(z'-\tilde{z})^2}\right)}}{\sqrt{L_1^2+(\tilde{x}-x)^2+(\tilde{z}-z)^2}\sqrt{L_2^2+(x'-\tilde{x})^2+(z'-\tilde{z})^2}} \mathrm{d}\tilde{x}\mathrm{d}\tilde{z} \right|^2\,, \tag{2.19}$$

which is the superposition of straight paths starting at the source (x, z) through all points inside the object plane $\int \mathrm{d}\tilde{x}\mathrm{d}\tilde{z}$ to the final point in the screen plane (x', z') with the amplitude of the wave a_0.

With the introduced transmission function, Eq. (2.14), the estimation of the emerging interference patterns is possible. Before we will discuss the results of the interference experiments, we discuss the particle-surface interaction, the CASIMIR–POLDER force, which will be considered in the following chapter.

chapter 3

CASIMIR–POLDER interaction

The CASIMIR–POLDER interaction describes the interaction of a neutral, polarisable particle with its induced image dipole at a dielectric surface [CP1948]. Its origin is the fluctuations of the ground-state electromagnetic field. These fluctuations induce a dipole moment $\mathbf{d}_{ind}(\omega) = \boldsymbol{\alpha}(\omega) \cdot \mathbf{E}_{fl.}(\omega)$, where the polarisability $\boldsymbol{\alpha}$ is a tensor of rank two. This induced dipole moment $\mathbf{d}_{ind}$ creates an image dipole inside the dielectric surface, where the classical COULOMB interaction between both yields the CASIMIR–POLDER force. For a derivation of the CASIMIR–POLDER potential, the quantised electromagnetic fields in the presence of macroscopic dielectric bodies are needed.

3.1 Quantisation of the electromagnetic field

We start from the microscopic MAXWELL equations [JDJ02]

$$\mathbf{div}\,\mathbf{E} = \frac{\varrho}{\varepsilon_0}\,, \tag{3.1}$$

$$\mathbf{div}\,\mathbf{B} = 0\,, \tag{3.2}$$

$$\mathbf{curl}\,\mathbf{E} = -\dot{\mathbf{B}}\,, \tag{3.3}$$

$$\mathbf{curl}\,\mathbf{B} = \mu_0\varepsilon_0\dot{\mathbf{E}} + \mu_0\mathbf{J}\,, \tag{3.4}$$

with the external sources and currents ϱ and $\mathbf{J}$, respectively, and the HAMILTON function

$$H = \frac{1}{2}\int \mathrm{d}^3r \left[\varepsilon_0\mathbf{E}^2(\mathbf{r},t) + \frac{1}{\mu_0}\mathbf{B}^2(\mathbf{r},t)\right]\,. \tag{3.5}$$

Our setup with neutral, but polarisable particles in a macroscopic environment implies that it is imperative to use the macroscopic Maxwell equations. We separate the current $\mathbf{J}$ and the charge density ϱ into induced and external parts

$$\varrho = \varrho_{ind} + \varrho_{ext}\,, \qquad \mathbf{J} = \mathbf{J}_{ind} + \mathbf{j}_{ext}\,. \tag{3.6}$$

The polarisation of the medium is the source of the induced charge density

$$\mathbf{div}\,\mathbf{P}(\mathbf{r}) = -\varrho_{ind}(\mathbf{r})\,. \tag{3.7}$$

The induced current is associated with the polarisation $\mathbf{P}(\mathbf{r})$ and magnetisation $\mathbf{M}(\mathbf{r})$ of the medium by the relation

$$\mathbf{J}_{ind} = \mathbf{curl}\,\mathbf{M}(\mathbf{r}) + \dot{\mathbf{P}}(\mathbf{r})\,. \tag{3.8}$$

The macroscopic Maxwell equations in the absence of external sources and currents then read

$$\begin{aligned}
\mathbf{div}\,\mathbf{B}(\mathbf{r}) &= 0\,, &(3.9)\\
\mathbf{curl}\,\mathbf{E}(\mathbf{r}) &= -\dot{\mathbf{B}}(\mathbf{r})\,, &(3.10)\\
\mathbf{div}\,\mathbf{D}(\mathbf{r}) &= 0\,, &(3.11)\\
\mathbf{curl}\,\mathbf{H}(\mathbf{r}) &= \dot{\mathbf{D}}(\mathbf{r})\,, &(3.12)
\end{aligned}$$

with the displacement field $\mathbf{D}(\mathbf{r})$ and the magnetic field $\mathbf{H}(\mathbf{r})$, with

$$\mathbf{D}(\mathbf{r}) = \varepsilon_0\mathbf{E}(\mathbf{r}) + \mathbf{P}(\mathbf{r})\,, \qquad \mathbf{H}(\mathbf{r}) = \frac{1}{\mu_0}\mathbf{B}(\mathbf{r}) - \mathbf{M}(\mathbf{r})\,, \tag{3.13}$$

respectively. It is often useful to assume that the medium responds linearly and locally to the externally applied fields. In such cases $\mathbf{P}(\mathbf{r})$ and $\mathbf{M}(\mathbf{r})$ are connected to an external field by

$$\begin{aligned}
\mathbf{P}(\mathbf{r},t) &= \varepsilon_0 \int_0^\infty \chi_e(\mathbf{r},\tau)\mathbf{E}(\mathbf{r},t-\tau)\mathrm{d}\tau + \mathbf{P}_N(\mathbf{r},t)\,, &(3.14)\\
\mathbf{M}(\mathbf{r},t) &= \frac{1}{\mu_0}\int_0^\infty \chi_m(\mathbf{r},\tau)\mathbf{B}(\mathbf{r},t-\tau)\mathrm{d}\tau - \mathbf{M}_N(\mathbf{r},t)\,. &(3.15)
\end{aligned}$$

The noise polarisation and magnetisation $\mathbf{P}_N(\mathbf{r},t)$ and $\mathbf{M}_N(\mathbf{r},t)$ are a consequence of the fluctuation-dissipation theorem. Equations (3.14) and (3.15) connect the polarisation and magnetisation with external electric and magnetic fields via the electric and magnetic susceptibilities χ_e and χ_m, respectively. Hence, they denote linear response functions. Consequently, the autocorrelation of the polarisation and magnetisation is proportional to the imaginary part the electric and magnetic susceptibilities. Because

of the vanishing correlation of the electric field one has to add the noise polarisation and magnetisation to satisfy the fluctuation-dissipation theorem. This macroscopic description is known as the LANGEVIN noise [LR00, SB08, SYB12-I] and is equivalent to the microscopic description that traces back to HUTTNER and BARNETT, see Refs. [SB08, SYB12-I, HB92a, HB92b, JH58]

By applying the temporal FOURIER transform to MAXWELL's equations (3.9)-(3.12) and inserting the relations (3.14) and (3.15) we obtain

$$\begin{aligned}
\mathbf{div}\,\mathbf{B}(\mathbf{r},\omega) &= 0\,, && (3.16)\\
\mathbf{curl}\,\mathbf{E}(\mathbf{r},\omega) &= i\omega\mathbf{B}(\mathbf{r},\omega)\,, && (3.17)\\
\varepsilon_0\,\mathbf{div}\,[\varepsilon(\mathbf{r},\omega)\mathbf{E}(\mathbf{r},\omega)] &= \varrho_N(\mathbf{r},\omega)\,, && (3.18)\\
\mathbf{curl}\,[\kappa(\mathbf{r},\omega)\mathbf{B}(\mathbf{r},\omega)] + i\frac{\omega}{c^2}\varepsilon(\mathbf{r},\omega)\mathbf{E}(\mathbf{r},\omega) &= \mu_0\mathbf{j}_N(\mathbf{r},\omega)\,, && (3.19)
\end{aligned}$$

with the noise charge density and the noise current density

$$\varrho_N(\mathbf{r},\omega) = -\,\mathbf{div}\,\mathbf{P}_N(\mathbf{r},\omega)\,, \qquad \mathbf{j}_N(\mathbf{r},\omega) = -i\omega\mathbf{P}_N(\mathbf{r},\omega) + \mathbf{curl}\,\mathbf{M}_N(\mathbf{r},\omega)\,, \quad (3.20)$$

respectively, and the relative dielectric permittivity and the inverse magnetic permeability

$$\varepsilon(\mathbf{r},\omega) = 1 + \int_0^\infty \chi_e(\mathbf{r},\tau)\mathrm{e}^{i\omega\tau}\mathrm{d}\tau\,, \qquad \kappa(\mathbf{r},\omega) = 1 - \int_0^\infty \chi_m(\mathbf{r},\tau)\mathrm{e}^{i\omega\tau}\mathrm{d}\tau\,, \quad (3.21)$$

respectively. By substituting FARADAY's law of induction, Eq. (3.17), into AMPÉRE's law, Eq. (3.19) one finds the vector HELMHOLTZ equation for the electric field

$$\mathbf{curl}\,[\kappa(\mathbf{r},\omega)\,\mathbf{curl}\,\mathbf{E}(\mathbf{r},\omega)] - \frac{\omega^2}{c^2}\varepsilon(\mathbf{r},\omega)\mathbf{E}(\mathbf{r},\omega) = i\omega\mu_0\mathbf{j}_N(\mathbf{r},\omega)\,. \quad (3.22)$$

In the following we restrict ourselves to purely electric interaction and neglect magnetic interaction due to the weakness of the magnetic response of typical materials. Therefore, we set $\kappa = 1$. The HELMHOLTZ equation can be formally solved by

$$\mathbf{E}(\mathbf{r},\omega) = i\omega\mu_0 \int \mathbf{G}(\mathbf{r},\mathbf{r}',\omega)\cdot\mathbf{j}_N(\mathbf{r}',\omega)\mathrm{d}^3r'\,. \quad (3.23)$$

with the dyadic GREEN function $\mathbf{G}$ that satisfies

$$\mathbf{curl}\,\mathbf{curl}\,\mathbf{G}(\mathbf{r},\mathbf{r}',\omega) - \frac{\omega^2}{c^2}\varepsilon(\mathbf{r},\omega)\mathbf{G}(\mathbf{r},\mathbf{r}',\omega) = \boldsymbol{\delta}(\mathbf{r}-\mathbf{r}')\,. \quad (3.24)$$

The GREEN tensor includes all information about the system, i.e. the optical properties, via the permittivity $\varepsilon(\mathbf{r},\omega)$, and the geometric shape of the scattering objects. Together with the boundary conditions of this differential equation,

$$\lim_{|\mathbf{r}-\mathbf{r}'|\to\infty} \mathbf{G}(\mathbf{r},\mathbf{r}',\omega) = 0\,, \quad (3.25)$$

the Helmholtz equation, Eq. (3.24), has a unique solution. The geometric shape of the scatterer enters this equation via continuity conditions for the electric and magnetic field at the surface of such an object, which can be converted into continuity conditions for the dyadic Green function, for details see Refs. [SB08, SYB12-I, SYB12-II, WCC95].

In order to quantise the electric field, we apply the second quantisation scheme, where canonical variables have to be found that can be quantised and the associated Poisson brackets defines the commutator. First, we substitute the noise currents with the relation [SB08, LK01, HTD03]

$$\mathbf{j}_N(\mathbf{r},\omega) = \sqrt{\frac{\hbar\varepsilon_0}{\pi}}\omega\sqrt{\mathrm{Im}\varepsilon(\mathbf{r},\omega)}\mathbf{f}(\mathbf{r},\omega)\,. \tag{3.26}$$

The quantisation of the field quantities $\mathbf{f}$ and $\mathbf{f}^*$ results in the commutator relation

$$\left[\hat{\mathbf{f}}(\mathbf{r},\omega),\hat{\mathbf{f}}^\dagger(\mathbf{r}',\omega')\right] = \boldsymbol{\delta}(\mathbf{r}-\mathbf{r}')\delta(\omega-\omega')\,, \tag{3.27}$$

and lead us to identify the operators $\hat{\mathbf{f}}$ and $\hat{\mathbf{f}}^\dagger$ as the bosonic ladder operators for the electromagnetic fields in the presence of macroscopic objects. The electric field operator for a spatially local, isotropic and inhomogeneous dielectric medium becomes

$$\hat{\mathbf{E}}(\mathbf{r},\omega) = i\sqrt{\frac{\hbar}{\pi\varepsilon_0}}\frac{\omega^2}{c^2}\int\sqrt{\mathrm{Im}\,\chi(\mathbf{r}',\omega)}\mathbf{G}(\mathbf{r},\mathbf{r}',\omega)\cdot\hat{\mathbf{f}}(\mathbf{r}',\omega)\,\mathrm{d}^3r'\,. \tag{3.28}$$

This equation means that the quantised electric field at the point $\mathbf{r}$ consists of all current excitations at the points $\mathbf{r}'$ propagating to $\mathbf{r}$ expressed by the bosonic ladder operators. The Hamiltonian reads

$$\hat{\mathrm{H}} = \int\hbar\omega\,\hat{\mathbf{f}}^\dagger(\mathbf{r},\omega)\cdot\hat{\mathbf{f}}(\mathbf{r},\omega)\,\mathrm{d}^3r\,\mathrm{d}\omega\,, \tag{3.29}$$

and the equation of motion $\left[\hat{\mathbf{f}}(\mathbf{r},\omega),\hat{\mathrm{H}}\right] = i\omega\hat{\mathbf{f}}(\mathbf{r},\omega)$ is satisfied. Note, that the total electric field is given by

$$\hat{\mathbf{E}}(\mathbf{r}) = \int_0^\infty \mathrm{d}\omega\,\hat{\mathbf{E}}(\mathbf{r},\omega) + \text{ h.c.}\,. \tag{3.30}$$

Consistant with the quantisation of the electromagnetic fields in vacuum, the commutator between the electric and magnetic field is equal to

$$\left[\hat{\mathbf{E}}(\mathbf{r}),\hat{\mathbf{B}}(\mathbf{r}')\right] = -\frac{i\hbar}{\varepsilon_0}\,\mathbf{curl}\,\boldsymbol{\delta}^\perp(\mathbf{r}-\mathbf{r}')\,, \tag{3.31}$$

with $\boldsymbol{\delta}^\perp$ the transversal δ-function.

One finds the expectation values for the ground-state field correlations

$$\left\langle\hat{\mathbf{E}}(\mathbf{r},\omega)\hat{\mathbf{E}}(\mathbf{r}',\omega')\right\rangle = \mathbf{0}\,, \tag{3.32}$$

$$\left\langle\hat{\mathbf{E}}(\mathbf{r},\omega)\hat{\mathbf{E}}^\dagger(\mathbf{r}',\omega')\right\rangle = \frac{\hbar}{\pi\varepsilon_0}\frac{\omega^2}{c^2}\mathrm{Im}\mathbf{G}(\mathbf{r},\mathbf{r}',\omega)\delta(\omega-\omega')\,, \tag{3.33}$$

where the integral relation involving products of GREEN functions [SB08]

$$\frac{\omega^2}{c^2}\int \mathrm{Im}\varepsilon(\mathbf{s},\omega)\mathbf{G}(\mathbf{r},\mathbf{s},\omega)\cdot\mathbf{G}^*(\mathbf{s},\mathbf{r}',\omega)\,\mathrm{d}^3s = \mathrm{Im}\mathbf{G}(\mathbf{r},\mathbf{r}',\omega)\,, \tag{3.34}$$

has been used. These correlators denote the fluctuations of the electric field and Eq. (3.33) is consistent with the fluctuation-dissipation theorem. In fact, Eq. (3.28) can be read as linear response relation for the electric field with the dyadic GREEN function $\mathbf{G}$ as linear response function. Another consequence of Eq. (3.33) is that the imaginary part of the dyadic GREEN function for equal positions $\mathbf{r} = \mathbf{r}'$ can be interpreted as the local mode density of the electric field, which is important for the interpretation of the CASIMIR–POLDER force discussed in the following. The left hand side of Eq. (3.33) is proportional to the spectral energy density of the electromagnetic field, which is itself proportional to the spectral mode density.

3.2 Linear response functions

The optical response functions[1], the susceptibility of the medium, $\chi(\omega)$, and the polarisability of the particle, $\boldsymbol{\alpha}(\omega)$, play an important role for the CASIMIR–POLDER force. These functions describe the response of the particle and the medium to an external electric field $\mathbf{E}$, which can be expressed by the temporal convolution [see Eq. (3.14)]. In this section we concentrate on scalar linear response functions. All properties can be generalised to tensorial linear response functions.

As $\chi(t)$ is a real function, its FOURIER transform $\chi(\omega)$ fulfils

$$\chi^*(\omega) = \chi(-\omega)\,. \tag{3.35}$$

This is known as the SCHWARZ reflection principle [SB08, SYB12-I]. As a consequence, the real part of $\chi(\omega)$ is an even function of the frequency and its imaginary part is an odd function.

Due to the fact that these response functions have no poles in the upper complex half plane, they are holomorphic (analytic) [BS08]. In addition, their values vanish for $|\omega| \to \infty$.[2]

Causality means that the response at time t should vanish for $t < 0$. This allows us to write

$$\chi(t) = \chi(t)\Theta(t)\,, \tag{3.36}$$

[1] Linear response functions depend on time t and space $\mathbf{r}$. For simplicity, we also call their FOURIER transform a response function.

[2] There are still response functions that do not vanish at infinity, such as the dielectric function $\varepsilon(\omega)$. By substracting these divergences the functions are still holomorphic and fulfil all relations.

with the Heaviside function $\Theta(t)$. Applying the Fourier transform to both sides of this equation, yields the Kramers-Kronig relation [BS08, SB08]

$$\chi(\omega) = \frac{1}{i\pi}\mathcal{P}\int_{-\infty}^{\infty}\frac{\chi(\omega')}{\omega-\omega'}\mathrm{d}\omega' \,, \tag{3.37}$$

where $\mathcal{P}\int$ denotes the Cauchy principal value. Summarising, causality (in temporal space) and the validity of the Kramers-Kronig relation (in frequency space) are equivalent.

By applying the Schwarz reflection principle and using the property that a symmetric integral over an odd function vanishes, the Kramers-Kronig relation connects the real and the imaginary part of the linear response function, which reads as

$$\mathrm{Re}\,\chi(\omega) = \frac{2}{\pi}\mathcal{P}\int_{0}^{\infty}\frac{\omega'\mathrm{Im}\,\chi(\omega')}{\omega'^2-\omega^2}\mathrm{d}\omega' \,, \qquad \mathrm{Im}\,\chi(\omega) = -\frac{2\omega}{\pi}\mathcal{P}\int_{0}^{\infty}\frac{\mathrm{Re}\,\chi(\omega')}{\omega'^2-\omega^2}\mathrm{d}\omega' \,. \tag{3.38}$$

After emphasising some general properties, we want to present some models to approximate an optical response function. The Drude–Lorentz model,

$$\chi(\omega) = \frac{\omega_p^2}{\omega_1^2-\omega^2-i\beta\omega} \,, \tag{3.39}$$

with the plasma frequency ω_p and the damping constant β, describes the response of a damped harmonic oscillator.

Another model is the Drude model,

$$\chi(\omega) = \frac{\omega_p^2}{-\omega^2-i\beta\omega} \,, \tag{3.40}$$

which equals the other model with vanishing eigenfrequency $\omega_1 = 0$. Both models describe an electron gase. The Drude model is applicable for free electrons. And the Drude–lorentz is for bounded electrons and describes a harmonic perturbation. Hence, it is based on the idea that an electron is elastically bound to an atomic core inside a solid, which is periodically driven by an external electric field with the frequency ω. The interaction between the electron and the atomic core then can be describe by an harmonic oscillator. The response function shows the amplitude of the electron's motion for different excitations ω. The plasma frequency ω_p scales the amplitude in the absence of the electric field. It is proportional to the strength of the binding to the core $\omega_p = \sqrt{\frac{n_e e^2}{\varepsilon_0 m_e}}$, with the electronic density n_e, the elementary charge e and the electronic mass m_e.

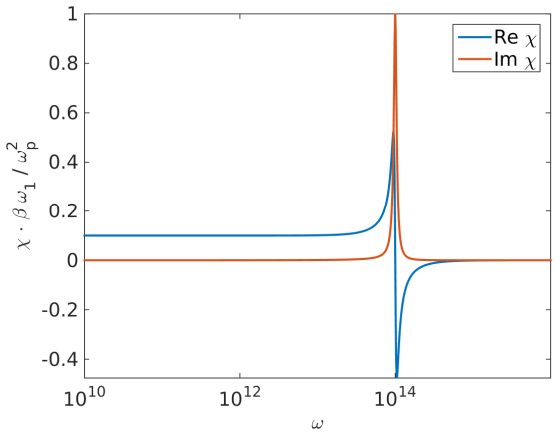

Figure 3.1: Sketch of the Lorentz model with the resonance frequency $\omega_1 = 1 \times 10^{14}\,\mathrm{rad\,s^{-1}}$ and a damping constant $\beta = 1 \times 10^{13}\,\mathrm{rad\,s^{-1}}$.

In order to approximate the optical response of a real material with more than one resonance, one has to sum over N different LORENTZ oscillators

$$\chi(\omega) = \sum_{i=1}^{N} \frac{\omega_{p,i}^2}{\omega_{1,i}^2 - \omega^2 - i\beta_i\omega}\,, \tag{3.41}$$

where each resonance has its own parameters: plasma frequency $\omega_{p,i}$, eigenfrequency $\omega_{1,i}$ and damping constant β_i. In practice, a fitting method will often be used for their estimation.

Figure 3.1 illustrates the behaviour of the LORENTZ function with the resonance frequency $\omega_1 = 1 \times 10^{14}\,\mathrm{rad\,s^{-1}}$ and a damping constant $\beta = 1 \times 10^{13}\,\mathrm{rad\,s^{-1}}$ normalised to the strength at the resonance $\mathrm{Re}\,\chi(\omega_1)$. One observes that its imaginary part follows the LORENTZ distribution function. By applying the KRAMERS-KRONIG relation its real part can be obtained.

In order to understand the CASIMIR–POLDER force and the spectroscopic reconstruction method, which will be introduced later, a discussion of the optical response properties for imaginary frequency arguments is useful. Recalling the LORENTZ model, we can separate it into its real part

$$\mathrm{Re}\,\chi(\omega) = \frac{\omega_p^2\left(\omega_1^2 - \omega^2\right)}{\left(\omega_1^2 - \omega^2\right)^2 + \beta^2\omega^2}\,, \tag{3.42}$$

and its imaginary part

$$\mathrm{Im}\,\chi(\omega) = \frac{\omega_p^2\beta\omega}{\left(\omega_1^2 - \omega^2\right)^2 + \beta^2\omega^2}\,. \tag{3.43}$$

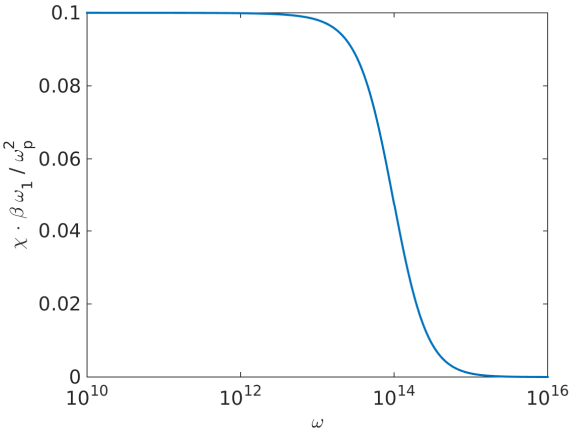

Figure 3.2: Sketch of the LORENTZ model for imaginary frequencies with the resonance frequency $\omega_1 = 1 \times 10^{14}\,\mathrm{rad\,s^{-1}}$ and a damping constant $\beta = 1 \times 10^{13}\,\mathrm{rad\,s^{-1}}$.

Both parts are connected by the KRAMERS-KRONIG relations, Eq. (3.38), which can be used to transform the response function to purely imaginary arguments. Due to the SCHWARZ reflection principle, the response function is real-valued for imaginary arguments, hence

$$\chi(i\xi) = \mathrm{Re}\,\chi(i\xi) = \frac{2}{\pi}\int_0^\infty \frac{\omega'\mathrm{Im}\,\chi(\omega')}{\omega'^2 + \xi^2}\mathrm{d}\omega'\,. \tag{3.44}$$

Figure 3.2 illustrates the behaviour of the LORENTZ model from Fig. 3.1 for imaginary frequency arguments. One observes that the relatively complicated behaviour for real arguments transforms into a smooth function, where the damping constant β describes the slope at the resonance frequency. Generally, every linear response function decreases monotonically along the imaginary frequency axis, which is advantageous for numerical computations.

3.3 Casimir–Polder interaction at zero temperature

The Casimir–Polder interaction is caused by the vacuum fluctuations of the electromagnetic field, which induces a dipole moment in a polarisable particle. The interaction is governed by the electric-dipole interaction $\hat{\mathrm{H}}_{int} = -\hat{\mathbf{d}} \cdot \hat{\mathbf{E}}$. This section describes the situation, in which the field and the polarisable particle are in their respective ground states, denoted by the ket vectors $|\{0\}\rangle$ and $|0\rangle$, respectively. Excited particles will be dealt with in the next section. The assumption of a nonpolar particle implies that the expectation value of the dipole operator vanishes, $\langle \hat{\mathbf{d}} \rangle = 0$.

The Hamiltonian consists of three parts, the field Hamiltonian $\hat{\mathrm{H}}_F$, Eq. (3.29), which describes the electric field in the presence of an absorbing macroscopic object, the Hamiltonian of the free particle, which is given by the sum over the projections onto the states $|n\rangle$ weighted by the energy of the state,

$$\hat{\mathrm{H}}_A = \sum_n \hbar\omega_n |n\rangle \langle n| \ , \tag{3.45}$$

and the interaction Hamiltonian $\hat{\mathrm{H}}_{int}$. Here, we follow the formalism described in Ref. [SB08]. The Casimir–Polder interaction is typically weak, which means that the Schrödinger equation can be solved by applying perturbation theory. A basis for the unperturbed system with the Hamiltonian

$$\hat{\mathrm{H}}_0 = \hat{\mathrm{H}}_F + \hat{\mathrm{H}}_A \tag{3.46}$$

is given by the tensor product

$$|\varphi\rangle = |\varphi_a\rangle \otimes |\varphi_f\rangle \equiv |\varphi_a, \varphi_f\rangle \ . \tag{3.47}$$

Note that the atom and the field stay in their ground states at low temperatures, $|\varphi_0\rangle = |0, \{0\}\rangle$. The energy shift caused by the interaction of the field with the atom can be obtained as a perturbation

$$\langle \Delta E \rangle = \langle \varphi_0 | \hat{\mathrm{H}}_{int} |\varphi_0\rangle + \sum_{\varphi_I \neq \varphi_0} \frac{\langle \varphi_0 | \hat{\mathrm{H}}_{int} |\varphi_I\rangle \langle \varphi_I | \hat{\mathrm{H}}_{int} |\varphi_0\rangle}{E_{\varphi_0} - E_{\varphi_I}} + \cdots \ , \tag{3.48}$$

with the intermediate state $|\varphi_I\rangle = |k, \mathbf{1}(\mathbf{r}, \omega)\rangle$, which means that the atom is excited in a state $|k\rangle$ and the field contains one elementary excitation $|\mathbf{1}(\mathbf{r}, \omega)\rangle = \hat{\mathbf{f}}^\dagger(\mathbf{r}, \omega) |\{0\}\rangle$. The first term of the perturbation series vanishes, because the field and the atom are in their respective ground states and all diagonal elements of $\hat{\mathrm{H}}_{int}$ vanishes due to its linearity in field and atomic operators. Recalling the field expression (3.28), the transition matrix element can be obtained as

$$\langle 0, \{0\} | \hat{\mathbf{d}} \cdot \hat{\mathbf{E}}(\mathbf{r}_A) |k, \mathbf{1}(\mathbf{r}, \omega)\rangle = i\frac{\omega^2}{c^2}\sqrt{\frac{\hbar}{\pi\varepsilon_0}\mathrm{Im}\varepsilon(\mathbf{r}_A, \omega)}\mathbf{d}_{0k} \cdot \mathbf{G}(\mathbf{r_A}, \mathbf{r}, \omega) \, , \tag{3.49}$$

which yields the energy shift

$$\langle \Delta E \rangle = -\frac{\mu_0}{\pi} \sum_k \int_0^\infty \frac{\omega^2}{\omega_{k0} + \omega} \mathbf{d}_{0k} \cdot \mathrm{Im}\mathbf{G}(\mathbf{r}_A, \mathbf{r}_A, \omega) \cdot \mathbf{d}_{k0} \, \mathrm{d}\omega \,, \tag{3.50}$$

where the integral relation, Eq. (3.34), has been used. It can be seen that the GREEN function entering the energy shift has to be evaluated in the coincidence limit with both spatial arguments being the position of the particle. The propagation of a photon described by the dyadic GREEN function can be separated into two parts, the free propagation and the scattering part due to the environment

$$\mathbf{G}(\mathbf{r}, \mathbf{r}', \omega) = \mathbf{G}^{(0)}(\mathbf{r}, \mathbf{r}', \omega) + \mathbf{G}^{(S)}(\mathbf{r}, \mathbf{r}', \omega) \,. \tag{3.51}$$

Because of the equal positions the free propagating part yields the free space LAMB shift by inserting the imaginary part of the free space GREEN function [SYB12-I]

$$\mathrm{Im}\mathbf{G}(\mathbf{r}, \mathbf{r}, \omega) = \frac{\omega}{6\pi c} \mathbf{1} \,, \tag{3.52}$$

into the CASIMIR–POLDER potential, Eq. (3.50), which provides the local density of state of the electromagnetic field at $\mathbf{r}$ apart from a factor of ω^2 and is assumed to be included in the atomic spectrum. Hence, the remaining part of the GREEN function is its scattering part $\mathbf{G}^{(\mathbf{S})}$. The superscript (S) will be omitted in the remaining text.

By using the atomic polarisability

$$\alpha(\omega) = \frac{2}{\hbar} \lim_{\epsilon \to 0} \sum_k \frac{\omega_{k0} \mathbf{d}_{0k} \otimes \mathbf{d}_{k0}}{\omega_{k0}^2 - \omega^2 - i\omega\epsilon} \,, \tag{3.53}$$

and the SCHWARZ reflection principle [JDJ02] for the dyadic GREEN function

$$\mathbf{G}(\mathbf{r}, \mathbf{r}', -\omega^*) = \mathbf{G}^*(\mathbf{r}, \mathbf{r}', \omega) \,, \tag{3.54}$$

the integration along the real frequency axis can be turned to the imaginary axis by using contour integration along the paths shown in Fig. 3.3, which yields a spatially dependent energy shift, that is interpreted as the CASIMIR–POLDER potential [SB08, SYB12-I]

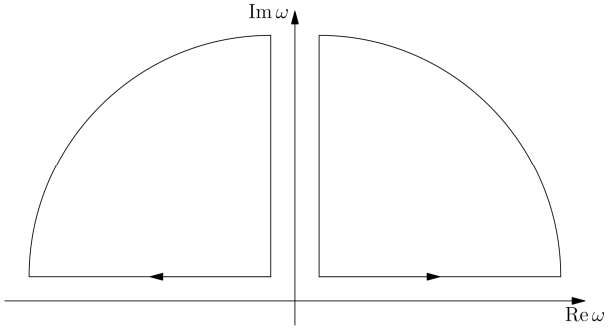

Figure 3.3: Sketch of the paths for the contour integration for the estimation of the CASIMIR–POLDER potential.

$$U_{CP}(\mathbf{r}_A) = \frac{\hbar\mu_0}{2\pi} \int_0^\infty \mathrm{d}\xi \, \xi^2 \, \mathrm{Tr} \left\{ \boldsymbol{\alpha}(i\xi) \mathbf{G}(\mathbf{r}_A, \mathbf{r}_A, i\xi) \right\} \,. \tag{3.55}$$

First, this expression shows the reason for the allocation as a dispersion force, because it varies with the frequency-dependent polarisability of the atom and the optical response of the media, which is included in the scattering Green function via the susceptibility. Second, the fundamental mechanism of the force can be read off: The interaction takes place via an exchange of virtual photons, which are back scattered to the particle. From Eq. (3.50), where the integral is taken along the real axis, the connection of the Casimir–Polder force with the fluctuations of the electromagnetic field can be seen, which induce dipole moments. These dipole moments create image dipoles inside the macroscopic body, which yields a force between both.

3.4 Thermal Casimir–Polder Forces

In the experimental setup, whose results we are discussing in Chapter 6, the molecular beam is created by laser evaporation. Here, the molecules are no longer in their ground state due to the energy transfer by the illumination with the laser. Therefore, the theory has to be extended to the Casimir–Polder potential for excited particles in a mixed state.

The starting point for the derivation of the Casimir–Polder potential in general is again the Hamiltonian

$$\hat{\mathrm{H}} = \int \mathrm{d}^3 r \int_0^\infty \mathrm{d}\omega\, \hbar\omega \hat{\mathbf{f}}^\dagger(\mathbf{r},\omega)\hat{\mathbf{f}}(\mathbf{r},\omega) + \sum_n \hbar\omega_n \left|n\right\rangle \left\langle n\right| + \hat{\mathrm{H}}_{int}\,, \tag{3.56}$$

where the first part denotes the Hamiltonian of the electromagnetic field, the second part of the molecule and the third the interaction between both. Again, we restrict ourselves to the electric-dipole interaction $\hat{\mathrm{H}}_{int} = -\hat{\mathbf{d}}\cdot\hat{\mathbf{E}}$.

In contrast to the previous section, we assume a state as a product state consisting of the ground and first excited states at the points $\mathbf{r}_i$, $\left|\varphi_k\right\rangle = \prod_i^k \left|\mathbf{1}(\mathbf{r}_i,\omega_i)\right\rangle$.

A thermal state of the electromagnetic field of temperature T is described by the density matrix

$$\hat{\varrho}_F = \frac{1}{Z}\Bigg(\left|\{0\}\right\rangle\left\langle\{0\}\right| + \sum_i \int \mathrm{d}^3 r_1 \cdots \mathrm{d}^3 r_i \int_0^\infty \mathrm{d}\omega_1 \cdots \mathrm{d}\omega_i \mathrm{e}^{-\frac{\hbar}{k_B T}\sum_{j=1}^n \omega_i}$$
$$\left|\mathbf{1}(\mathbf{r}_1,\omega_1)\cdots\mathbf{1}(\mathbf{r}_j,\omega_j)\right\rangle\left\langle\mathbf{1}(\mathbf{r}_1,\omega_1)\cdots\mathbf{1}(\mathbf{r}_j,\omega_j)\right|\Bigg)\,, \tag{3.57}$$

where the partition function Z equals the trace over the term in the parenthesis.

In the experiment, whose results are discussed in Chapter 6, the molecules are located on a glass window and accelerated by a laser beam shining in from the back.

As a consequence, the molecules are not necessarily in their ground state. Instead, they have to be described by incoherent superpositions of internal-energy eigenstates [SYB12-II]

$$\hat{\varrho}_M = \sum_n p_n \left|n\right\rangle \left\langle n\right| , \quad (3.58)$$

with a probability distribution p_n, which we assume to be a Maxwell–Boltzmann distribution. The thermal field state can be expanded in a basis set of Fock states. With the electric field (3.28) and the fundamental commutator $\left[\hat{\mathbf{f}}(\mathbf{r},\omega), \hat{\mathbf{f}}^\dagger(\mathbf{r}',\omega')\right] = \delta(\omega-\omega')\delta(\mathbf{r}-\mathbf{r}')$ the integral can be evaluated and yields the result [SYB12-II]

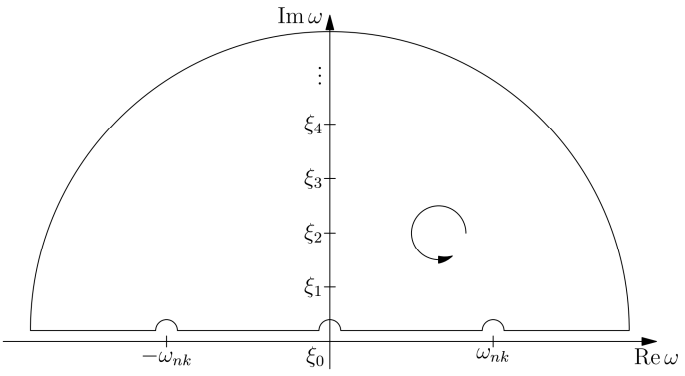

Figure 3.4: Sketch of the paths for the contour integration for the estimation of the thermal Casimir–Polder potential.

$$\langle \Delta E \rangle = \frac{\mu_0}{\pi} \sum_n p_n \sum_k \mathcal{P} \int_0^\infty \omega^2 \mathbf{d}_{nk} \cdot \mathrm{Im}\, \mathbf{G}(\mathbf{r}_A, \mathbf{r}_A, \omega) \cdot \mathbf{d}_{kn} \left(\frac{\sum_{j=0}^\infty j \mathrm{e}^{-\frac{j\hbar\omega}{k_B T}}}{\sum_{j=0}^\infty \mathrm{e}^{-\frac{j\hbar\omega}{k_B T}}} \frac{1}{\omega+\omega_{nk}} - \frac{\sum_{j=0}^\infty (j+1) \mathrm{e}^{-\frac{j\hbar\omega}{k_B T}}}{\sum_{j=0}^\infty \mathrm{e}^{-\frac{j\hbar\omega}{k_B T}}} \frac{1}{\omega-\omega_{nk}} \right) \mathrm{d}\omega \, . \quad (3.59)$$

The inner series (sums over j) can be evaluated and yields

$$\langle \Delta E \rangle = \frac{\mu_0}{\pi} \sum_n p_n \sum_k \mathcal{P} \int_0^\infty \mathrm{d}\omega\, \omega^2 \left(\frac{n(\omega)}{\omega+\omega_{nk}} - \frac{n(\omega)+1}{\omega-\omega_{nk}} \right) \mathbf{d}_{nk} \cdot \mathrm{Im}\mathbf{G}(\mathbf{r}_A, \mathbf{r}_A, \omega) \cdot \mathbf{d}_{kn} \, , \quad (3.60)$$

where $n(\omega)$ denotes the mean thermal photon number,

$$n(\omega) = \frac{1}{\mathrm{e}^{\frac{\hbar\omega}{k_B T}} - 1} \, . \quad (3.61)$$

By using the identity $n(-\omega) = -(n(\omega)+1)$, the Casimir–Polder potential can be obtained analogously

$$\langle \Delta E \rangle = \frac{\mu_0}{2\pi i} \sum_n p_n \sum_k \times \mathcal{P} \int_{-\infty}^\infty \mathrm{d}\omega\, \omega^2 \left(\frac{n(\omega)}{\omega-\omega_{nk}} - \frac{n(\omega)+1}{\omega-\omega_{nk}} \right) \mathbf{d}_{nk} \cdot \mathbf{G}(\mathbf{r}_A, \mathbf{r}_A, \omega) \cdot \mathbf{d}_{kn} \, . \quad (3.62)$$

This result can again be simplified by using contour-integral techniques. The paths are illustrated in Fig. 3.4. Here, the poles of the integrand in the upper complex

halfplane are needed. Two poles can be found on the real axis at $\omega = \pm\omega_{nk}$, which show a resonant behaviour of the integral. The thermal photon number $n(\omega)$ has poles for purely imaginary frequency arguments $\omega = i\xi_j$, with the Matsubara frequencies

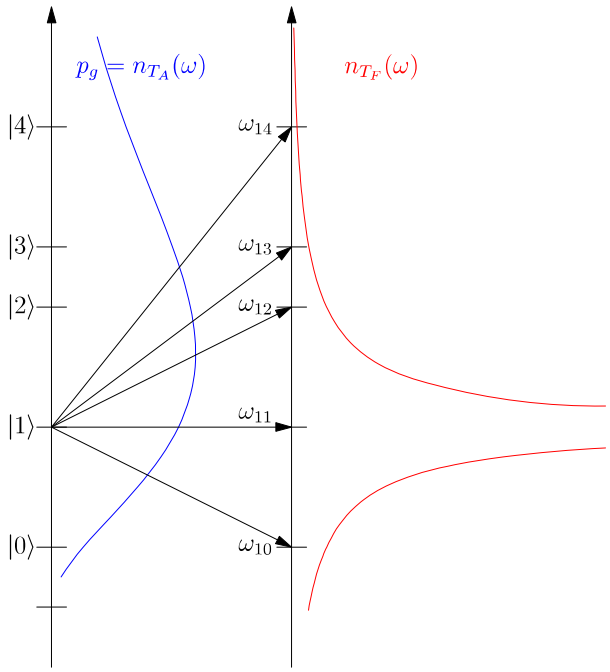

Figure 3.5: Sketch of the energy ordering, the resulting dipole transitions and the corresponding Bose–Einstein statistics for the environment at temperature T_F (red) and an example for the statistics of the population, which is Boltzmann distributed with the particle temperature T_A (blue).

$$\xi_j = \frac{2\pi k_B T}{\hbar} j\,, \qquad j = 0, 1, 2, \ldots\,. \tag{3.63}$$

The total Casimir–Polder potential, Eq. (3.62), separates into a sum over all potentials U_n for the initial state n of the molecule weighted by its probability p_n

$$U_{CP}(\mathbf{r}_A) = \sum_n p_n U_n(\mathbf{r}_A)\,. \tag{3.64}$$

Each potential U_n can be separated into a resonant and a nonresonant part due to the different poles

$$U_n(\mathbf{r}_A) = U_n^{\text{nres}}(\mathbf{r}_A) + U_n^{\text{res}}(\mathbf{r}_A)\,, \tag{3.65}$$

which are

$$U_n^{\text{nres}}(\mathbf{r}_A) = \mu_0 k_B T {\sum_j}' \xi_j^2 \,\text{Tr}\{\boldsymbol{\alpha}_n(i\xi_j)\mathbf{G}(\mathbf{r}_A, \mathbf{r}_A, i\xi_j)\}\,, \tag{3.66}$$

$$\begin{aligned} U_n^{\text{res}}(\mathbf{r}_A) = &-\mu_0 \sum_{k<n} (n(\omega_{nk}) + 1)\,\omega_{nk}^2\,\text{Tr}\{\mathbf{d}_{kn} \otimes \mathbf{d}_{nk}\text{Re}\,\mathbf{G}(\mathbf{r}_A, \mathbf{r}_A, \omega_{nk})\} \\ &+\mu_0 \sum_{k>n} n(\omega_{nk})\omega_{nk}^2\,\text{Tr}\{\mathbf{d}_{kn} \otimes \mathbf{d}_{nk}\text{Re}\,\mathbf{G}(\mathbf{r}_A, \mathbf{r}_A, \omega_{nk})\}\,, \end{aligned} \tag{3.67}$$

with the notation

$${\sum_j}' a_j = \frac{1}{2}a_0 + \sum_{j=1}^{\infty} a_j\,. \tag{3.68}$$

The nonresonant part is defined analogously to the Casimir–Polder potential at zero temperature. The difference between both is that the integral along the imaginary frequency axis is replaced by a discrete sum over the Matsubara frequencies. The resonant part appears in addition. It couples directly at the resonance frequencies of the involved particle. It separates into two parts, one for the intermediate state below the

initial and final state $k < n$, which yields a repulsive force, and one for the intermediate state above the initial state $k > n$. This part yields an attractive force.

It should be noted that the resonant part of the CASIMIR–POLDER potential has real photons as exchange particles. Figure 3.5 illustrates these two different contributions to the resonant CASIMIR–POLDER potential. It shows the energy ordering of a particle and the possible dipole transitions starting at the first excited state with their associated transition frequencies ω_{1j}. The probability distributions are given for the transition starting at the first excited state (red) and a possible distribution for the initial state (blue). Here, we choose a classical BOLTZMANN distribution with the atomic temperature[3] T_A. The contributions due to transition into higher states with the frequencies $\omega_{12}, \ldots, \omega_{1n}$ yield the attractive part of the CASIMIR–POLDER force and the transition into the lower state the repulsive ones. All these transitions contribute to the CASIMIR–POLDER potential. In order to obtain the full interaction, all these individual contributions have to be added up and weighted by their probabilities p_n as well as the number of contributing photons $n_T(\omega)$ at the frequency ω.

3.5 The scattering Green function

As can be seen from the last two sections, the scattering GREEN function plays an essential role in this theory. The solution of the fundamental vector HELMHOLTZ equation (3.24) is not easy to find and analytically only possible for a very small number of geometries. This section deals with the simplest geometry, the propagation in free space, and with a possible construction method to approximate the scattering GREEN function in arbitrary environments.

The advantage of the presented formulation of the CASIMIR–POLDER forces is the separation between the particle and the scatterer by introducing the atomic polarisability and the GREEN function, which includes the geometric and optical properties of the scatterer. The latter enter the vector HELMHOLTZ equation,

$$\mathbf{curl}\,[\mathbf{curl}\,\mathbf{G}(\mathbf{r},\mathbf{r}',\omega)] - \frac{\omega^2}{c^2}\varepsilon(\mathbf{r},\omega)\mathbf{G}(\mathbf{r},\mathbf{r}',\omega) = \boldsymbol{\delta}(\mathbf{r}-\mathbf{r}')\,, \tag{3.24}$$

via the permittivity $\varepsilon(\mathbf{r},\omega)$. The differential equation has to be supplemented by the boundary condition $\lim_{|\mathbf{r}-\mathbf{r}'|\to\infty}\mathbf{G}(\mathbf{r},\mathbf{r}',\omega) = 0$, which is known as SOMMERFELD's radiation condition. At the interface between dielectric objects, one has to impose MAXWELL's continuity conditions

$$\mathbf{n}\times\mathbf{E}^{(1)} = \mathbf{n}\times\mathbf{E}^{(2)}\,, \quad \mathbf{n}\times\mathbf{B}^{(1)} = \mathbf{n}\times\mathbf{B}^{(2)}\,, \tag{3.69}$$

[3] We consider the temperature of a particle as its averaged internal energy.

which yield the conditions for the Green tensor

$$\mathbf{n} \times \mathbf{G}^{(1)} = \mathbf{n} \times \mathbf{G}^{(2)}\,, \quad \mathbf{n} \times \mathbf{curl}\,\mathbf{G}^{(1)} = \mathbf{n} \times \mathbf{curl}\,\mathbf{G}^{(2)}\,. \tag{3.70}$$

In the following, we discuss some properties of the Green function. We first discuss the simplest solution of the vector Helmholtz equation, the free-space solution. In the next step we introduce an approximation method, the Born series expansion of the dyadic Green function.

3.5.1 The free-space propagator

Let us assume that the entire space is filled with a homogeneous and isotropic dielectric medium. In this case, the dielectric permittivity $\varepsilon(\omega)$ is spatially independent and the vector Helmholtz equation simplifies to

$$\mathbf{curl}\,[\mathbf{curl}\,\mathbf{G}(\mathbf{r},\mathbf{r}',\omega)] - \frac{\omega^2}{c^2}\varepsilon(\omega)\mathbf{G}(\mathbf{r},\mathbf{r}',\omega) = \boldsymbol{\delta}(\mathbf{r}-\mathbf{r}')\,. \tag{3.71}$$

In addition, the dyadic Green function becomes translationally invariant, meaning that it depends only on the difference between both spatial coordinates $\boldsymbol{\varrho} = \mathbf{r} - \mathbf{r}'$, $\mathbf{G}(\mathbf{r},\mathbf{r}',\omega) \equiv \mathbf{G}(\boldsymbol{\varrho},\omega)$. Therefore, the differential equation can be solved by the use of the Fourier transform technique. With

$$\mathbf{G}(\mathbf{k},\omega) = \frac{1}{(2\pi)^{3/2}} \int \mathbf{G}(\boldsymbol{\varrho},\omega) \mathrm{e}^{-i\mathbf{k}\cdot\boldsymbol{\varrho}}\, \mathrm{d}^3k\,, \tag{3.72}$$

the Fourier transform of the vector Helmholtz equation reads

$$-\mathbf{k}\times\mathbf{k}\times\mathbf{G}(\mathbf{k},\omega) - \frac{\omega^2}{c^2}\varepsilon(\omega)\mathbf{G}(\mathbf{k},\omega) = \mathbf{I}\,, \tag{3.73}$$

where $\mathbf{I}$ denotes the three dimensional unit matrix. This algebraic equation can be easily solved by the decomposition of the unit tensor $\mathbf{I}$ into its transversal and longitudinal parts with respect to the wave vector $\mathbf{k}$, which yields

$$\mathbf{I} = \left(\mathbf{I} - \frac{\mathbf{k}\otimes\mathbf{k}}{k^2}\right) + \frac{\mathbf{k}\otimes\mathbf{k}}{k^2}\,. \tag{3.74}$$

By using the identity for the double vector product

$$-\mathbf{k}\times\mathbf{k}\times \equiv k^2\left(\mathbf{I} - \frac{\mathbf{k}\otimes\mathbf{k}}{k^2}\right)\,, \tag{3.75}$$

shows that the first term of the vector Helmholtz equation (3.71) is transverse. The dyadic Green function is found to be

$$\mathbf{G}(\boldsymbol{\varrho},\omega) = \frac{c^2}{(2\pi)^{3/2}} \int \left[\frac{1}{k^2c^2 - \omega^2\varepsilon(\omega)}\left(\mathbf{I} - \frac{\mathbf{k}\otimes\mathbf{k}}{k^2}\right) - \frac{1}{\omega^2\varepsilon(\omega)}\frac{\mathbf{k}\otimes\mathbf{k}}{k^2}\right] \mathrm{e}^{i\mathbf{k}\cdot\boldsymbol{\varrho}}\, \mathrm{d}^3k\,. \tag{3.76}$$

With the relation $q^2(\omega) = \omega^2\varepsilon(\omega)/c^2$, the result is

$$\mathbf{G}(\boldsymbol{\varrho},\omega) = \frac{1}{4\pi q^2(\omega)}\left[\mathbf{grad}\,\mathbf{grad} + q^2(\omega)\mathbf{I}\right]\frac{\mathrm{e}^{iq(\omega)\varrho}}{\varrho}\,. \tag{3.77}$$

After the evaluation of the derivatives, the dyadic GREEN function again can be decomposed into transverse and longitudinal parts (for details, see [SB08, SYB12-I]). More important in this context is the free-space solution, where $\varepsilon(\omega) = 1$, for which one finds

$$\mathbf{G}^{(0)}(\boldsymbol{\varrho},\omega) = -\frac{c^2}{3\omega^2}\boldsymbol{\delta}(\boldsymbol{\varrho}) + \frac{\omega}{4\pi c}\left[f\left(\frac{c}{\omega\varrho}\right)\mathbf{I} - g\left(\frac{c}{\omega\varrho}\right)\frac{\boldsymbol{\varrho}\otimes\boldsymbol{\varrho}}{\varrho^2}\right]\mathrm{e}^{i\frac{\varrho\omega}{c}}\,, \tag{3.78}$$

with $f(x) = x + ix^2 - x^3$ and $g(x) = x + 3ix^2 - 3x^3$.

3.5.2 The Born series expansion

The analytically known solutions of the vector HELMHOLTZ equation is limited to the cases of a planarily, cylindrically or spherically layered system. In order to describe the scattering in arbitrary geometries, an approximation method is needed to construct the dyadic GREEN function. Here, we present the BORN series expansion, which is a method to express an unknown GREEN function by references. We start from the vector HELMHOLTZ equations for the unknown scattering GREEN function $\mathbf{G}$ and for the reference GREEN function $\mathbf{G}^{(0)}$ [SB08, SYB12-II]

$$\mathbf{curl}\,\mathbf{curl}\,\mathbf{G}(\mathbf{r},\mathbf{r}',\omega) - \frac{\omega^2}{c^2}\varepsilon(\mathbf{r},\omega)\mathbf{G}(\mathbf{r},\mathbf{r}',\omega) = \boldsymbol{\delta}(\mathbf{r}-\mathbf{r}')\,, \tag{3.79}$$

$$\mathbf{curl}\,\mathbf{curl}\,\mathbf{G}^{(0)}(\mathbf{r},\mathbf{r}',\omega) - \frac{\omega^2}{c^2}\varepsilon^{(0)}(\mathbf{r},\omega)\mathbf{G}^{(0)}(\mathbf{r},\mathbf{r}',\omega) = \boldsymbol{\delta}(\mathbf{r}-\mathbf{r}')\,, \tag{3.80}$$

with the reference permittivity $\varepsilon^{(0)}(\mathbf{r},\omega)$. The difference between both equations yields an inhomogeneous HELMHOLTZ equation for the sought scattering GREEN function $\mathbf{G}^{(S)}$

$$\begin{aligned}&\mathbf{curl}\,\mathbf{curl}\,\mathbf{G}^{(S)}(\mathbf{r},\mathbf{r}',\omega) - \frac{\omega^2}{c^2}\varepsilon^{(0)}(\mathbf{r},\omega)\mathbf{G}^{(S)}(\mathbf{r},\mathbf{r}',\omega)\\ &\quad= \frac{\omega^2}{c^2}\delta\varepsilon(\mathbf{r},\omega)\left[\mathbf{G}^{(0)}(\mathbf{r},\mathbf{r}',\omega) + \mathbf{G}^{(S)}(\mathbf{r},\mathbf{r}',\omega)\right]\,,\end{aligned} \tag{3.81}$$

with the difference of the permittivities $\delta\varepsilon(\mathbf{r},\omega) = \varepsilon(\mathbf{r},\omega) - \varepsilon^{(0)}(\mathbf{r},\omega)$. The fundamental solution of this equation is the reference GREEN function $\mathbf{G}^{(0)}$, which follows by comparison with Eq. (3.80). Hence, the scattering GREEN function can formally be found by the convolution of the right hand side of Eq. (3.81) with the reference GREEN function

$$\mathbf{G}^{(S)}(\mathbf{r},\mathbf{r}',\omega) = \int \mathrm{d}^3s\mathbf{G}^{(0)}(\mathbf{r},\mathbf{s},\omega)\cdot\frac{\omega^2}{c^2}\delta\varepsilon(\mathbf{s},\omega)\left[\mathbf{G}^{(0)}(\mathbf{s},\mathbf{r}',\omega) + \mathbf{G}^{(S)}(\mathbf{s},\mathbf{r}',\omega)\right]\,. \tag{3.82}$$

Due to the appearance of the scattering Green function on both sides of this equation, this is a Fredholm equation of the second kind, which can be solved iteratively

$$\begin{aligned}\mathbf{G}^{(S)}(\mathbf{r},\mathbf{r}',\omega) &= \frac{\omega^2}{c^2}\int \mathrm{d}^3 s' \mathbf{G}^{(0)}(\mathbf{r},\mathbf{s}',\omega)\delta\varepsilon(\mathbf{s}',\omega)\mathbf{G}^{(0)}(\mathbf{s}',\mathbf{r}',\omega) \\ &+ \left(\frac{\omega^2}{c^2}\right)^2 \int \mathrm{d}^3 s' \mathrm{d}^3 s'' \mathbf{G}^{(0)}(\mathbf{r},\mathbf{s}',\omega)\delta\varepsilon(\mathbf{s}',\omega)\mathbf{G}^{(0)}(\mathbf{s}',\mathbf{s}'',\omega)\delta\varepsilon(\mathbf{s}'',\omega)\mathbf{G}^{(0)}(\mathbf{s}'',\mathbf{r}',\omega) \\ &+ \cdots . \end{aligned} \tag{3.83}$$

In first order, the propagation from $\mathbf{r}'$ to $\mathbf{r}$ can be separated via the sum (respectively integral) over all individual points of the macroscopic body $\mathbf{s}'$

$$\mathbf{G}_1^{(S)}(\mathbf{r},\mathbf{r}',\omega) = \frac{\omega^2}{c^2}\int \mathrm{d}^3 s' \, \mathbf{G}^{(0)}(\mathbf{r},\mathbf{s}',\omega)\chi(\mathbf{s}',\omega)\mathbf{G}^{(0)}(\mathbf{s}',\mathbf{r}',\omega)\,, \tag{3.84}$$

which is also known as Hamaker approximation. For the next order of this expansion, a second interaction point $\mathbf{s}''$ has to be added and one finds

$$\begin{aligned}\mathbf{G}_2^{(S)}(\mathbf{r},\mathbf{r}',\omega) &= \frac{\omega^4}{c^4} \\ &\times \int \mathrm{d}^3 s'' \mathrm{d}^3 s' \, \mathbf{G}^{(0)}(\mathbf{r},\mathbf{s}'',\omega)\chi(\mathbf{s}'',\omega)\mathbf{G}^{(0)}(\mathbf{s}'',\mathbf{s}',\omega)\chi(\mathbf{s}',\omega)\mathbf{G}^{(0)}(\mathbf{s}',\mathbf{r}',\omega)\,, \end{aligned} \tag{3.85}$$

which defines for three separated objects in the free-space the so-called Axilrod-Teller potentials. This series continues and converges to the scattering Green function

$$\mathbf{G}^{(S)}(\mathbf{r},\mathbf{r}',\omega) = \sum_{n=1}^{\infty} \mathbf{G}_n^{(S)}(\mathbf{r},\mathbf{r}',\omega)\,. \tag{3.86}$$

Figure 3.6 illustrates this expansion as it is used for the Casimir–Polder potential up to the second order.

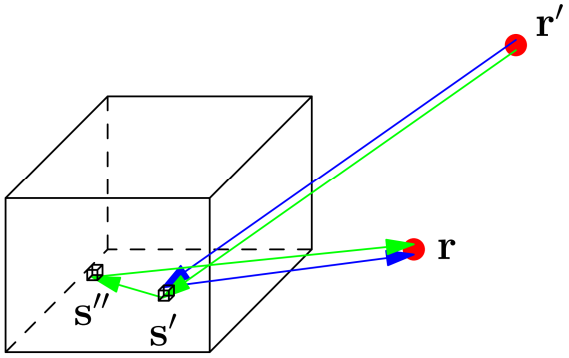

Figure 3.6: Sketch of the Born series expansion: In first order a photon propagates from $\mathbf{r}'$ to $\mathbf{r}$ via $\mathbf{s}'$ (blue), in second order again from $\mathbf{r}'$ to $\mathbf{r}$ via $\mathbf{s}'$ and $\mathbf{s}''$ (green).

We choose the free-space propagator (see Sec. 3.5.1) as reference Green function. In this case, the reference permittivity is $\varepsilon^{(0)} = 1$, and the difference permittivity is equivalent to the susceptibility of the macroscopic body $\delta\varepsilon(\mathbf{r},\omega) \equiv \chi(\mathbf{r},\omega)$, which means that the Born series is a series expansion with respect to the susceptibility of the considered medium.

For materials with spatially independent permittivity the Born series expansion can be interpreted as a polynomial expansion with respect to the difference permittivity (in our case, the susceptibility). For an insulating material, the terms corresponding to multiple scattering effects are negligibly small and the solid body can be treated as a dilute gas, which provides a rapid convergence of the Born series. Typically, in these situations the Born series expansion can be truncated after the first term.

chapter 4

The BORN series expansion for periodic gratings

The convergence of the approximation of the scattering GREEN tensor by the BORN series expansion is limited to two cases; either the source and final points are far away from the scattering object, or its electric response is weak. In other situations, higher orders of the BORN series expansions are needed. A possible remedy to this restriction is the local-field corrected version of the BORN series.

4.1 Local-field corrected Born series

A consequence of the BORN series expansion of the form derived in the previous chapter is a slow convergence for conducting materials, such as gold, with a large susceptibility. Hence, higher orders of interaction are needed to obtain a sufficiently good approximation. However, the number of integrals which have to be solved increases exponentially with the number of interaction orders. A second disadvantage is that the integrals are solvable analytically only for highly symmetric geometries. Even their numerical treatment raises issues due to the singularity of the integrand and the self interaction of the volume elements.[1] In order to improve this convergence problem, we will introduce a local-field corrected BORN series expansion.

[1] The numerical treatment would require the definition of an exclusion volume. The result does not converge with respect to such exclusion volumes, which is caused by the singularity of the scattering GREEN function in the spatial coincidence limit. Its behaviour in an environment of the coincidence limit $\mathbf{r}' = \mathbf{r} + \delta\mathbf{r}$ is not well defined. Hence, its treatment for a continuous body has errors. A solution of this problem can be given by the microscopic consideration of the crystal structure [KS15].

Its starting point is the general separation of every Green function into a regular part $\mathbf{R}$ and a singular part $\mathbf{D}$

$$\mathbf{G}(\mathbf{r},\mathbf{r}',\omega) = \mathbf{D}(\mathbf{r},\mathbf{r}',\omega) + \mathbf{R}(\mathbf{r},\mathbf{r}',\omega)\,, \tag{4.1}$$

with $\mathbf{D} = -\frac{c^2}{3\omega^2}\boldsymbol{\delta}(\mathbf{r}-\mathbf{r}')$ for the free-space propagator, see Sec. 3.5.1. The spatial singularity for an isotropic and homogeneous medium in Cartesian coordinates can be written as $\mathbf{D} = \lambda\boldsymbol{\delta}(\mathbf{r}-\mathbf{r}')$ with a constant λ, which does not depend on the spatial coordinate. Note that, in general, the singularity depends on a pilot vector $\mathbf{p}$, which denotes the direction of the singularity extraction. Hence, the singular part is proportional to its projector $\mathbf{D} \propto \mathbf{p}\otimes\mathbf{p}$. The same method introduced in the following can be applied to this general description as well, but we restrict ourselves to the case of an isotropic and homogeneous medium.

Inserting this separation, Eq. (4.1), into the Born series expansion yields

$$\begin{aligned}
&\mathbf{G}^{(S)}(\mathbf{r},\mathbf{r}',\omega) = \\
&\quad\frac{\omega^2}{c^2}\int \mathrm{d}^3s'\,[\lambda\boldsymbol{\delta}(\mathbf{r}-\mathbf{s}') + \mathbf{R}(\mathbf{r},\mathbf{s}',\omega)]\cdot\delta\varepsilon(\mathbf{s}',\omega)\cdot[\lambda\boldsymbol{\delta}(\mathbf{s}'-\mathbf{r}') + \mathbf{R}(\mathbf{s}',\mathbf{r}',\omega)] \\
&\quad+\left(\frac{\omega^2}{c^2}\right)^2\int \mathrm{d}^3s'\mathrm{d}^3s''\,[\lambda\boldsymbol{\delta}(\mathbf{r}-\mathbf{s}') + \mathbf{R}(\mathbf{r},\mathbf{s}',\omega)]\cdot\delta\varepsilon(\mathbf{s}',\omega) \\
&\quad\cdot[\lambda\boldsymbol{\delta}(\mathbf{s}'-\mathbf{s}'') + \mathbf{R}(\mathbf{s}',\mathbf{s}'',\omega)]\cdot\delta\varepsilon(\mathbf{s}'',\omega)\cdot[\lambda\boldsymbol{\delta}(\mathbf{s}''-\mathbf{r}') + \mathbf{R}(\mathbf{s}'',\mathbf{r}',\omega)] + \cdots\,.
\end{aligned} \tag{4.2}$$

The integral over the δ-distributions can now be performed. We remember the physical meaning of the spatial arguments. The considered propagation starts at the source point $\mathbf{r}'$ to the final point $\mathbf{r}$ via the intermediate point $\mathbf{s}$, where their numbering denotes their chronology with respect to their temporal scattering. Due to the spatial separation of the scattering object, which defines the integration range, and the source and final points the first and the last δ-functions do not contribute to the integral, whereas the integrals over the δ-functions depending on two intermediate points can be performed. This gives

$$\begin{aligned}
\mathbf{G}^{(S)}(\mathbf{r},\mathbf{r}',\omega) &= \frac{\omega^2}{c^2}\int \mathrm{d}^3s'\mathbf{R}(\mathbf{r},\mathbf{s}',\omega)\cdot\delta\varepsilon(\mathbf{s}',\omega)\cdot\mathbf{R}(\mathbf{s}',\mathbf{r}',\omega) \\
&+\left(\frac{\omega^2}{c^2}\right)^2\Bigg[\lambda\int \mathrm{d}^3s'\mathrm{d}^3s''\,\mathbf{R}(\mathbf{r},\mathbf{s}',\omega)\cdot\delta\varepsilon^2(\mathbf{s}',\omega)\cdot\mathbf{R}(\mathbf{s}',\mathbf{r}',\omega) + \lambda^2\int \mathrm{d}^3s'\mathrm{d}^3s'' \\
&\times\mathbf{R}(\mathbf{r},\mathbf{s}',\omega)\cdot\delta\varepsilon(\mathbf{s}',\omega)\cdot\mathbf{R}(\mathbf{s}',\mathbf{s}'',\omega)\cdot\delta\varepsilon(\mathbf{s}'',\omega)\cdot\mathbf{R}(\mathbf{s}'',\mathbf{r}',\omega)\Bigg] + \cdots\,.
\end{aligned} \tag{4.3}$$

One observes that the i-th order of the Born series expansion contains a term that is similar to the first-order contribution, in which only two regular parts appear and which differ by a factor $(\lambda\delta\varepsilon(\mathbf{s}',\omega))^{i-1}$. By assuming a spatially homogeneous susceptibility

of the scattering object, this factor can be taken out of the integral and yields the first order of the local-field corrected BORN series expansion

$$\mathbf{G}_1^{(S)}(\mathbf{r},\mathbf{r}',\omega) = \frac{\omega^2}{c^2}\delta\varepsilon(\omega)\sum_{i=0}^{\infty}\left[\frac{\omega^2}{c^2}\lambda\delta\varepsilon(\omega)\right]^i \int \mathrm{d}^3 s' \mathbf{R}(\mathbf{r},\mathbf{s}',\omega)\mathbf{R}(\mathbf{s}',\mathbf{r}',\omega)\,. \tag{4.4}$$

This expression can be further simplified by making use of the geometric series

$$\sum_{i=0}^{\infty}\left[\frac{\omega^2}{c^2}\lambda\delta\varepsilon(\omega)\right]^i = \left(1-\left[\frac{\omega^2}{c^2}\lambda\delta\varepsilon(\omega)\right]\right)^{-1}\,, \tag{4.5}$$

which converges, if the condition

$$\left|\frac{\omega^2}{c^2}\lambda\delta\varepsilon(\omega)\right| < 1 \tag{4.6}$$

is satisfied.

Applying this method to the free-space propagator yields the local-field-corrected first-order scattering GREEN function [HB14]

$$\mathbf{G}_1^{(S)}(\mathbf{r},\mathbf{r},\omega) = \frac{\omega^2}{c^2}\chi(\omega)\sum_{n=0}^{\infty}\left(-\frac{1}{3}\chi(\omega)\right)^n \int \mathrm{d}^3 s\, \mathbf{R}(\mathbf{r},\mathbf{s},\omega)\cdot\mathbf{R}(\mathbf{s},\mathbf{r},\omega)\,, \tag{4.7}$$

and the geometric series over the susceptibility can be performed, which yields

$$\mathbf{G}_1^{(S)}(\mathbf{r},\mathbf{r},\omega) = \frac{\omega^2}{c^2}\frac{\chi(\omega)}{1+\chi(\omega)/3}\int \mathrm{d}^3 s\, \mathbf{R}(\mathbf{r},\mathbf{s},\omega)\cdot\mathbf{R}(\mathbf{s},\mathbf{r},\omega)\,. \tag{4.8}$$

For the nonresonant CASIMIR–POLDER potential the scattering GREEN function has to be evaluated at imaginary frequencies. The convergence criterion for the geometric series is a pointwise convergence in the frequency domain. By using the monotonical decrease of the susceptibility χ for imaginary frequencies, one can either define a cut-off frequency ξ_0 by $\chi(i\xi_0) = 3$, which defines the upper boundary for the convergence of the geometric series. Or, if one claims the convergence for all frequencies, the criterion has to be evaluated in the static limit of the susceptibility, which can be found at $\xi = 0$. Therefore, the condition for the convergence of the geometric series simplifies to $\max_{\xi\in\mathbb{R}^+}\left|\frac{\chi(i\xi)}{3}\right| = \frac{\chi(0)}{3} = 0.96$, which is valid for silicon nitride, for which we use that the dielectric susceptibility is strictly monotonically decreasing for imaginary frequencies and the static permittivity of silicon nitride is $\varepsilon(0) = 3.87$ [BS12]. One observes that even for an insulating material the convergence of the geometric series is weak.

Hence, the convergence directly depends on the susceptibility of the medium. Consequently, by choosing a conductive material, such as gold, this condition will not be satisfied any more. However, we concentrate on the CASIMIR–POLDER interaction, where the scattering GREEN function is combined with other frequency dependent functions. In the following, we analyse that this condition is not as important for the

Casimir–Polder potential, where the contributions of the scattering Green function are weighted by the square of the frequencies, which can be understood as a convergence generating factor. In the next section, we apply this method to the experimental situation, in which a rubidium cloud is reflected at a gold grating. We will show that the local-field corrected Born-series expansion matches the experimental data very well.

4.2 The Casimir–Polder potential near a gold grating

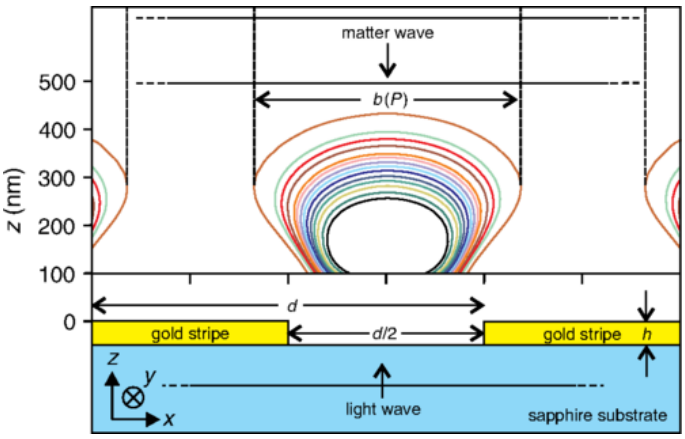

Figure 4.1: Geometry of the grating structure with the periodicity $d = 1\,\mu\text{m}$ and $h = 50\,\text{nm}$ height. The coloured lines show the equipotential lines for different laser powers $P = 120, \ldots, 247\,\text{mW}$ (black to brown) for rubidium atoms with an incident velocity $v = 3.4\,\text{cms}^{-1}$. Taken from [HB14].

In this section, we illustrate the Born series approach by computing the Casimir–Polder interaction of rubidium atoms with the scalar polarisability $\alpha(\omega)$, taken from Ref. [DAS09], in front of a gold grating. We consider a sapphire substrate periodically covered with gold stripes of 50nm height, 500nm thickness and a periodicity of $1\,\mu\text{m}$. We also assume the grating to be infinitely extended in the vertical direction. Figure 4.1 illustrates the cross section of this setup. The density in the atom cloud is relatively low, which justifies the assumption that the interaction between the atoms is negligible and, consequently, only the Casimir–Polder interaction between a single atom and the grating structure has to be considered.

We calculate the potential of a single grating bar, which will be continued periodically. Using the same reasoning, the Casimir–Polder force arising from the sapphire substrate is negligible by comparison with the force induced by the gold stripes. We used the Drude model for the susceptibility of the gold stripes [EP85, VBS08]

$$\varepsilon(\omega) = 1 - \frac{\omega_p^2}{\omega(\omega + i\gamma)}\,, \tag{4.9}$$

with the plasma frequency $\omega_p = 9.0\,\text{eV} = 1.37 \cdot 10^{16}\,\text{rad}\,\text{s}^{-1}$ and the relaxation rate $\gamma = 27.1\,\text{meV} = 4.12 \cdot 10^{13}\,\text{rad}\,\text{s}^{-1}$. With this model, we calculated the Casimir–Polder potential of a rubidium atom in front of a single gold stripe by numerically

evaluating the local-field-corrected first-order BORN approximation, Eq. (4.8)

$$U_{CP}(\mathbf{r}_A) = -\frac{\hbar}{2\pi\varepsilon_0}\int_0^\infty \mathrm{d}\xi\,\alpha(i\xi)\frac{\chi(i\xi)}{1+\chi(i\xi)/3}\int_V \mathrm{d}^3r'\,\mathrm{Tr}\left\{\mathbf{R}(\mathbf{r}_A,\mathbf{r}',i\xi)\cdot\mathbf{R}(\mathbf{r}',\mathbf{r}_A,i\xi)\right\}\,, \tag{4.10}$$

with the regular part of the free-space propagator, Eq. (3.78),

$$\mathbf{R}(\mathbf{r},\mathbf{r}',\omega) = \frac{\omega}{4\pi c}\left[f\left(\frac{c}{\omega\varrho}\right)\mathbf{I} - g\left(\frac{c}{\omega\varrho}\right)\frac{\boldsymbol{\varrho}\otimes\boldsymbol{\varrho}}{\varrho^2}\right]\mathrm{e}^{i\frac{\varrho\omega}{c}}\,, \tag{4.11}$$

and the difference vector $\boldsymbol{\varrho} = \mathbf{r} - \mathbf{r}'$. The total CASIMIR–POLDER potential can be obtained by the periodic extension to higher numbers of grating bars.

4.3 Comparison of the local-field-corrected Born approach with experimental data

With this section we close the discussion about the local-field-corrected BORN series expansion. Finally, we apply this method to an experimental situation and discuss its results. In order to complete this discussion we also compare the results with a CASIMIR–POLDER potential calculated with a different method, the so-called RAYLEIGH expansion. This method is a FOURIER expansion of the electric field.

A sapphire crystal is periodically covered with gold stripes, which have the extensions mentioned in Sec. 4.2. The crystal is illuminated by a laser under an angle of $\theta = 0.6196\,\mathrm{rad}$, which yields a transmission of 88% into the crystal [HB14]. The laser is blue detuned relative to the frequency of the strongest dipole transition of the rubidium atoms, which have a transition frequency at $\lambda = 780\,\mathrm{nm}$. The evanescent laser field induces a repulsive potential. Between the atoms and the gold stripes, the CASIMIR–POLDER force acts attractively. The total interaction is obtained by the superposition of both potentials. Figure 4.2 illustrates the potential landscape in the experimentally relevant regime.

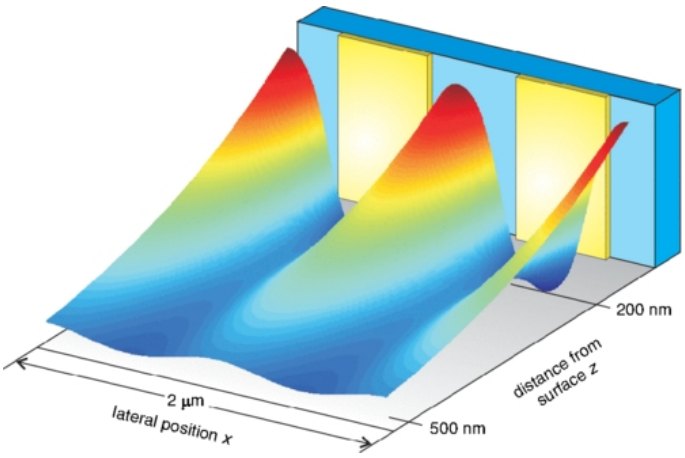

Figure 4.2: Simulation of the combined potential landscape for a laser power of $P = 211\,\mathrm{mW}$ and the experimentally used detuning $\Delta\lambda = 15\,\mathrm{nm}$. Taken from [HB14].

By changing the laser power P, the ratio between the attractive Casimir–Polder potential and the repulsive evanescent field can be altered. In the experiment, an atom cloud propagates with a slow velocity of $v = 3.4\,\mathrm{cm\,s^{-1}}$ towards this structured surface. By considering the wave front of such a plane matter wave (black straight lines in Fig. 4.1), which propagates towards such potential, one finds that the parts of the waves, which are in front of a gold stripe, were attracted by this surface and other parts, that are located in front of a grating opening, were dominated by the repulsive force due to the evanescent field. By solving the classical motion of a particle inside such potential landscape, one finds attractive and repulsive trajectories. Assuming that the atoms propagate like a plane wave towards this potential, a range can be defined where the particles were reflected at the surface. Based on the simulations, the repulsive regime can be obtained as a function of the laser power $b(P)$, see Fig. 4.1. This length is the projection of the equipotential lines of the potential energy evaluated at the kinetic energy of the atoms onto the planar wave front. The ratio between this length $b(P)$ and the periodicity d of the structure can be interpreted as a classical reflection coefficient $b(P)/d$, as it quantifies the fraction of reflected atoms. It has to be remarked that this ratio is not a reflection coefficient in the original optical sense. It does not describe the appearance of higher reflection orders. However, it is experimentally quantifiable by counting the reflected particles compared to the total number of particles. The experiment was performed at the University of Tübingen in the group of S. Slama, and we compared the measurements with the calculated potentials by the local-field corrected Hamaker approximation, see Sec. 4.1, and the exact calculation using the Rayleigh expansion for periodic structures [HB14].

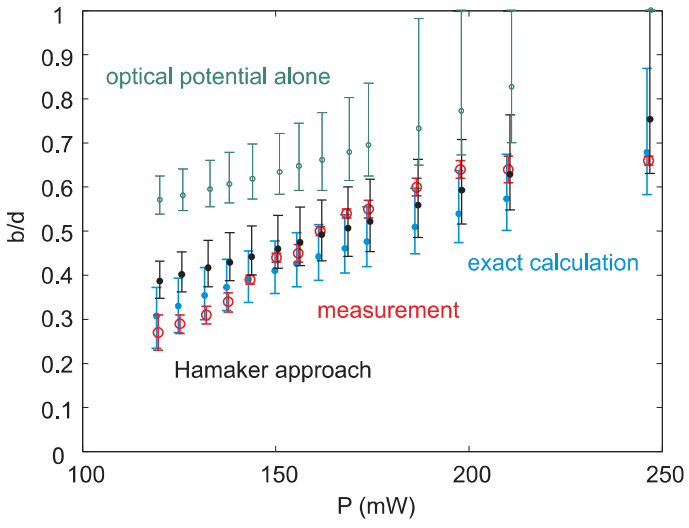

Figure 4.3: Comparison between the Hamaker approach (black), "exact" calculation by using Rayleigh expansion (blue), measurements (red) and the optical potential alone (green). Taken from [HB14].

Figure 4.3 shows the comparison between the measurements and the different theoretical approaches. One observes that for high laser powers the measurements and the theories match one another within the error bars due to the measurement inaccuracies with respect to the laser power P and the velocity of the particle v. For lower laser powers, the Hamaker theory does not fit the measurements very well. In this regime, the Casimir–Polder po-

tential becomes dominant compared to the evanescent field and the atom cloud is able to penetrate the evanescent potential deeper. Consequently, the interaction of the atoms with the gold stripes increases and the HAMAKER approach fails. Due to the large conductivity of the gold stripes, multiple reflections of the virtual photon inside the grating bar are becoming important, meaning that higher orders of the BORN series expansion are needed. To show the importance of the CASIMIR–POLDER potential for this experiment, we also plotted the evanescent optical potential alone (green line in Fig. 4.3).

Summarising, there are two situations in which the HAMAKER approximation is a good description of the CASIMIR–POLDER potential. For large distances between the particle and the scatterer the HAMAKER approach approximates the CASIMIR–POLDER potential very well, because in this regime multiple scattering processes inside the scatterer are negligible. If the dielectric response of the involved scatterer is small, the HAMAKER approach fits the experimental situation very precisely as well. This condition is satisfied for insulating materials. Here, coming from a microscopic point of view, multiple scattering processes between the atoms of the solid body are negligibly small. On the other hand, the RAYLEIGH expansion is only manageable for potentials outside of periodic structures. If e.g. the potential between two gold stripes is needed, the numerical effort of this expansion increases enormously. The second disadvantage of this expansion is that its application is limited to periodic structures, because it is based on the FOURIER expansion of the field. For large distances the number of required FOURIER modes is very small, and increases rapidly with decreasing atom-surface separation.

chapter 5

Correction of the Casimir–Polder potential for spatially extended particles

The Casimir–Polder force, in the way it has been introduced in Secs. 3.3 and 3.4, has been derived for point-like particles with anisotropic polarisability. In general, the different spatial orientations of this polarisability and the scattering object have to be taken into account. Often, an isotropic average of the polarisability is used to reduce the polarisability to a scalar quantity [SB08]

$$\boldsymbol{\alpha}(i\xi) \xrightarrow{\text{iso. average}} \alpha(i\xi)\mathbf{I}\,, \tag{5.1}$$

with the three-dimensional identity matrix $\mathbf{I}$. However, for large and rotating molecules, this assumption yields a large deviation of the Casimir–Polder potential. We will start this chapter with some considerations about some physical attributes of such molecules using the example of Phthalocyanine in Sec. 5.1 and we will discuss an experiment in Chapter 6, where the model describing the extension and rotation of the particle is needed. In the following, we will determine the influence of the spatial extension and the rotation of the particle to the Casimir–Polder potential. First, we will discuss the rotational effects in general, therefore we neglect the finite size and assume a point particle. Second, we will consider the complete dependency of the Casimir–Polder force on the rotation and extension of the molecule.

5.1 Example molecule: Phthalocyanine

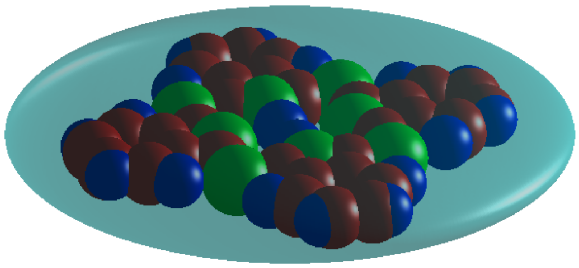

Figure 5.1: Sketch of a Phthalocyanine molecule including the equipotential surface of one per mille of the electronic density. Taken from [FS15].

Phthalocyanine is an organic dye molecule (Fig. 5.1). It consists of four benzene rings which are connected by nitrogen bonds. Altogether, the molecule is comprised of 32 carbon, 18 hydrogen and eight nitrogen atoms. This molecule is favoured in experiments due to its good detectability. It is a dye molecule, which can be excited by laser light and its fluorescence can be detected. As was shown in the previous chapters, the complete optical information of the particle is needed for the description of the Casimir–Polder force. Some absorption or extinction spectra exist in the literature, which are restricted to the visible range. A small number of spectra even include the ultraviolet range. However, the important infrared spectra are not immediately available. Therefore, we initially restricted ourselves to the extinction spectrum[1], shown in Fig. 5.2. This extinction spectrum $\tilde{\varepsilon}(\omega)$ is related to the imaginary part of the polarisability $\alpha(\omega)$ by the Clausius-Mosotti relation [JDJ02]

$$\operatorname{Im}\alpha(\omega) = \frac{\ln 10}{2}\frac{c}{\omega}\varepsilon_0\tilde{\varepsilon}(\omega)\,. \tag{5.2}$$

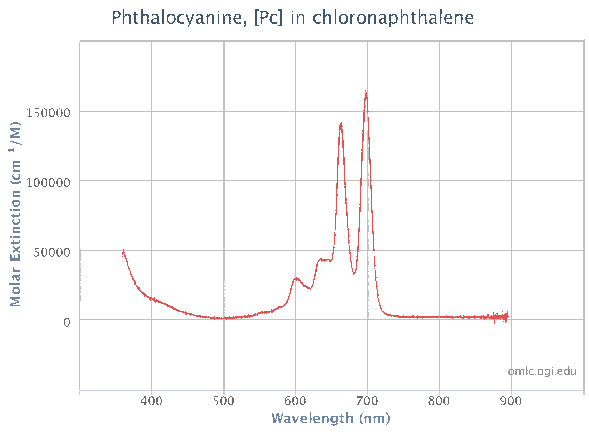

Figure 5.2: Absorption spectrum $\tilde{\varepsilon}(\omega)$ of Phthalocyanine. Taken from http://omlc.ogi.edu/spectra/PhotochemCAD/html/074.html.

In order to compute the Casimir–Polder interaction of Phthalocyanine, its polarisability at imaginary frequencies is needed, which can be obtained by applying the Kramers-Kronig relation [JDJ02]

$$\alpha(i\xi) = \frac{2}{\pi}\int_0^\infty \frac{\omega\operatorname{Im}\alpha(\omega)}{\omega^2+\xi^2}\mathrm{d}\omega\,. \tag{5.3}$$

Using this spectrum and both relations - the Clausius-Mosotti relation, Eq. (5.2), and the Kramers-Kronig relation, Eq. (5.3) - to calculate the polarisability of Phthalocyanine for imaginary frequencies will not be correct due to its restricted extinction spectrum. This

[1] http://omlc.ogi.edu/spectra/PhotochemCAD/html/074.html

deviation can be traced back to two causes: First, the absorption spectrum is only known in the visible range, but for the application of the Kramers-Kronig relation it is needed at all frequencies. Hence, the missing infrared spectrum due to vibrational transitions may yield a sizeable deviation. Second, Phthalocyanine is a pancake-shaped flat molecule with a strongly anisotropic polarisability, whereas we have assumed a point particle.

A second spectrum can be found in the literature, which allows us to include the ultraviolet range (See Fig. 4 in Ref. [BS70]). Combining these two spectra we obtain a high resolution view of the visible part of the spectrum of Fig. 5.2 and the ultraviolet spectrum from the second one. Including this second spectrum the effective Casimir–Polder potential increases by a factor of around 1.5.

As mentioned before, the knowledge about the infrared spectrum is important for the Casimir–Polder force. Such spectra are very rare in the literature. Therefore, we applied the following approximation. From the literature [RS09] the static polarisability is known to be $\alpha(0) = 98.6\text{Å}^3$. We can compare this static polarisability with that which arises as a result of the Kramers-Kronig relation with $\xi = 0$

$$\alpha(0) = \alpha(i0) = \frac{2}{\pi} \int_0^\infty \frac{\operatorname{Im} \alpha(\omega)}{\omega} \mathrm{d}\omega \,. \tag{5.4}$$

The difference between these should be caused by the missing contribution of the infrared spectrum. We assume that the dipole transition frequencies are densely spaced in the low frequency domain due to the large number of expected vibrations and rotations of the molecule. Then, the steps in the polarisability with imaginary frequencies are continuous and we assume a linear relation for the polarisability on the imaginary frequency axis between the static polarisability $\alpha(0)$ and the first frequency peak $\alpha(i\omega)$ in the visible range with $\omega \approx 2.1 \times 10^{15}\,\mathrm{rad\,s^{-1}}$. Thus, the Casimir–Polder potential rescales by an additional factor of around 4.3 which appears by taking the vibrations and rotations into account.

The next step is to include the anisotropy of the molecule. Here, we use the static anisotropic polarisability tensor, which is known from the literature [RS09] to be

$$\boldsymbol{\alpha}(0) = \operatorname{diag}(134.2, 134.2, 27.5)\,\text{Å}^3 \,. \tag{5.5}$$

We assume that the frequency dependence is approximately the same in all directions for the polarisability at imaginary frequencies. The anisotropic spectrum of a molecule illustrates that the anisotropy is dominated at low frequencies, where the vibrational and rotational modes are located. In the higher frequencies range describing the electronic transition, every particle becomes isotropic. Because of the dominance of the low

frequencies range of the polarisability for the estimation of the CASIMIR–POLDER potential, the restriction to the anisotropic part is valid. The visualisation of the relative polarisabilities implies that the anisotropy is approximately constant in the low frequency range. Normalising the static polarisability tensor and multiplying it with our calculated dynamic polarisability yields a good approximation of the total polarisability of Phthalocyanine

$$\boldsymbol{\alpha}(i\xi) = 1/98.6\,\mathrm{diag}(134.2, 134.2, 27.5)\alpha(i\xi)\,. \tag{5.6}$$

With all these assumptions we have a good first model to describe the molecule, but there still remain some inaccuracies. The molecule travels freely through the apparatus, so it can rotate and vibrate.

Let us first discuss the vibrations of the molecule. One can imagine that this flat molecule vibrates during its transition through the grating. The ground-state polarisability $\boldsymbol{\alpha}$ is constructed from the dipole transitions between the ground state $|0\rangle$ and excited states $|k\rangle$ [SB08]

$$\boldsymbol{\alpha}(\omega) = \lim_{\varepsilon\to 0}\frac{2}{\hbar}\sum_k \frac{\omega_{k0}\mathbf{d}_{0k}\otimes\mathbf{d}_{k0}}{\omega_{k0}^2-\omega^2-i\omega\varepsilon}\,. \tag{5.7}$$

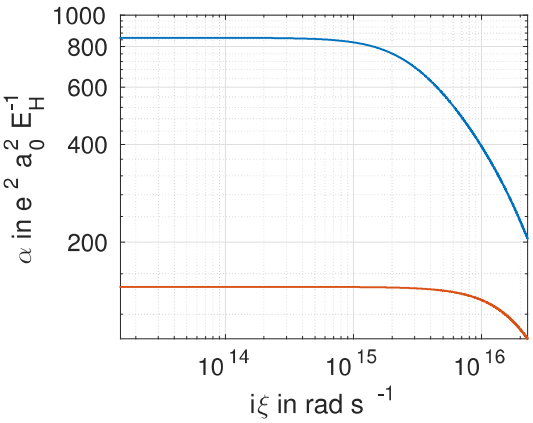

(a) Polarisability of Phthalocyanine for imaginary frequencies $i\xi$ along the semi-major axis (blue) and along the semi-minor axis (red).

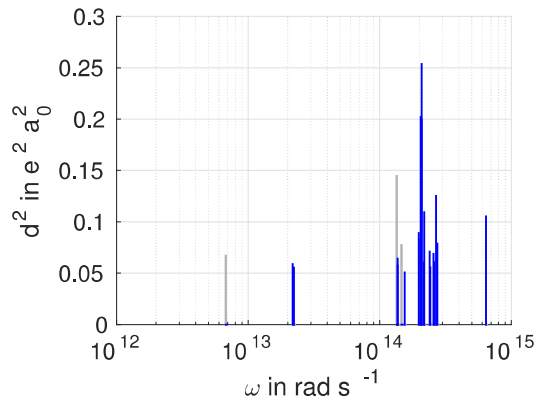

(b) Dipole transitions of Phthalocyanine from ground into the first excited state in-plane (blue) and out-off-plane (grey).

Figure 5.3: Polarisability and dipole transitions of Phthalocyanine based on molecular dynamical simulation.

The vibrations are often described in a harmonic approximation, where the potential of the intermolecular bond is expanded in a TAYLOR series around its equilibrium position up to the second order. In order to take these resulting dipole moments into account, we calculate the polarisability and the dipole transitions by a molecular dy-

namics simulation[2] [BF15]. Such methods can directly estimate the polarisability for imaginary arguments. In order to verify the simulated polarisability, we performed a number of checks. First, we computed the real and imaginary parts of the polarisability for real arguments, which we compared with the known spectra. Second, the static polarisability should also be reproduced on the imaginary frequency axis. The resulting polarisability is plotted in Fig. 5.3 (a). In order to estimate the resonant part of the Casimir–Polder potential, the dipole transitions from the ground state into an excited state are needed. Therefore, we calculate the dipole transitions into the first excited states by using the harmonic approximation. The result is shown in Fig. 5.3 (b).

In order to follow the description for the thermal Casimir–Polder force, see Sec. 3.4, the polarisability α_n and the dipole transitions $\mathbf{d}_{nk}$ depend on the initial state $|n\rangle$. The calculation of these state-dependent quantities is very difficult. In the experiment, which we will discuss in the next chapter, it was shown that the velocity of the molecules is Boltzmann distributed with a temperature $T \approx 1200\,\mathrm{K}$ [BF15], which refers to the external degrees of freedom. In order to identify the internal degrees of freedom, we have to make some assumptions. The molecule is in a thermal state $|\psi\rangle$, which we assume to be Boltzmann distributed

$$|\psi\rangle = \sum_n p_n |n\rangle \,, \tag{5.8}$$

with

$$p_n = \frac{1}{\mathcal{N}} \mathrm{e}^{-E_n/(k_B T)} \,, \qquad \mathcal{N} = \sum_n \mathrm{e}^{-E_n/(k_B T)} \,, \tag{5.9}$$

with the Boltzmann constant k_B and the eigenstates and their corresponding energies $|n\rangle$ and E_n, respectively.

This temperature corresponds to the internal degrees of freedom and we assume that it is less than the external temperature, $T \ll 1200\,\mathrm{K}$ in the absence of better spectroscopic measurements. This leads us to assume that the states, which can be occupied, belong to the rotational and vibrational excitations. The energy corresponding to this temperature is too low to reach electronic excitations. Hence, we assume that the change of the polarisability with respect to the different initial states $|n\rangle$ is negligible. Therefore, we identify the polarisability for all initial states, which can be occupied to be equal to the ground-state polarisability;

$$\alpha_n \equiv \alpha \,. \tag{5.10}$$

[2] At this point, we gratefully acknowledge contributions by Dr. Olga Bokareva for computing molecular polarisability and dipole moments.

5.2 Rotational average

As mentioned previously, even for point-like particles the orientation between the scatterer (laboratory fixed frame) and the particle has to be taken into account. Such orientational dependency can be added to the Casimir–Polder potential by introducing a rotational matrix $\mathbf{R}(\mathbf{\Omega})$, which should not be confused with the regular part of the Green function, Eq. (4.1), which describes the orientation of the molecular and the laboratory fixed frame. The Casimir–Polder potential then reads as

$$U_{CP}(\mathbf{r}_A, \mathbf{\Omega}) = \frac{\hbar\mu_0}{2\pi} \int_0^\infty \mathrm{d}\xi\, \xi^2\, \mathrm{Tr}\left\{\mathbf{R}^{-1}(\mathbf{\Omega}) \cdot \boldsymbol{\alpha}(i\xi) \cdot \mathbf{R}(\mathbf{\Omega}) \cdot \mathbf{G}(\mathbf{r}_A, \mathbf{r}_A, i\xi)\right\} , \tag{5.11}$$

where we consider the Casimir–Polder potential for ground-state particles, Eq. (3.55). The components of the argument of the rotational matrix are the angles for the elementary rotations, $\mathbf{\Omega} = (\Phi, \Theta, \Psi)$, which will be described in detail in the following. As shown before, a repulsive Casimir–Polder force can be achieved with a thermally excited particle. Later, we will present that the Casimir–Polder potential becomes repulsive for specific orientations $\mathbf{\Omega}$ and for anisotropic particles as well.

The rotational average then follows from the integration over all possible orientations

$$U_{CP}(\mathbf{r}_A) = \int \mathrm{d}\mathbf{\Omega}\, U_{CP}(\mathbf{r}_A, \mathbf{\Omega}) . \tag{5.12}$$

Before we start with the analysis of such a rotational averaging method, we want to determine, in which experimental situations that method is useful, and how the rotation can be described with respect to the symmetry of the particle and of the scatterer.

Here, we introduce two time scales: The time τ_{rot} that the molecule needs for a complete rotation and the effective interaction time with the scatterer, τ_{int}. The ratio between these two timescales tell us whether the rotational averaging method can be applied or not. Let us consider first the diffraction at thin membranes, for which $\tau_{int} < \tau_{rot}$. Here, a particle passes the grating with an arbitrary, but fixed orientation. The emerging interference patterns are independent of this orientation and, consequently, they have to be averaged incoherently [SH15]. Therefore, an averaging of the Casimir–Polder potential in this case does not make any sense.

In the opposite regime, which is more important for us, the rotational time is shorter than or roughly equal to the interaction time $\tau_{rot} \lesssim \tau_{int}$. This can be achieved by performing an interference experiment with thicker gratings. In such situations, the molecule performs more than one rotation during the interaction with the scatterer. Thus, we can assume that the phase impressed upon the matter wave is averaged over all orientations. Consequently, the interaction potential has to be rotationally averaged.

In order to compute the interaction with a rotating molecule, one has to think about the choice of the coordinate system for the rotation $\mathbf{\Omega}$. Here, we use the EULER angles with the convention of the so-called TAIL-BRYAN angles. This is a very intuitive description of the EULER angles, because they give the rotations only in the molecular fixed frame. They are applied in the navigation of aircraft. One angle describes a rotation around the pitch axis, which moves the aircraft's nose up and down. The second angle is for a rotation around the yaw axis, which shows movements of the nose from side to side. The last angle is for a rotation around the roll axis, where the nose will stand still and the particle rolls around the longitudinal axis. For the following consideration, we assume an ellipsoidally shaped molecule in front of a dielectric plate. By choosing this description for the rotations, the invariances of the medium (rotation around the surface normal) and the particle (rotations around the symmetry axes) will average out immediately. These rotations are described by the operation with an elementary rotation matrix. The complete rotational matrix is the product of the elementary rotations [MER95]

$$\mathbf{R}(\Phi,\Theta,\Psi) = \begin{pmatrix} 1 & 0 & 0 \\ 0 & \cos\Phi & \sin\Phi \\ 0 & -\sin\Phi & \cos\Phi \end{pmatrix} \begin{pmatrix} \cos\Theta & 0 & -\sin\Theta \\ 0 & 1 & 0 \\ \sin\Theta & 0 & \cos\Theta \end{pmatrix} \begin{pmatrix} \cos\Psi & \sin\Psi & 0 \\ -\sin\Psi & \cos\Psi & 0 \\ 0 & 0 & 1 \end{pmatrix}, \tag{5.13}$$

with the pitch Θ, yaw Ψ and roll angles Φ.

Using this rotational averaging method the different orientations and the rotational motion of the molecules can be taken into account. In addition, the finite spatial extent of the particle are important due to the comparable length scales of the molecule and its distance to the scattering object. For example, the molecule has a width of about 1.3 nm. The shortest distance to the grating a molecule reaches is in the order of several nanometers. Hence, the treatment as point-like particles is not valid any more.

5.3 Spatially extended molecules

The CASIMIR–POLDER force is caused by the polarisability of the particle, which is connected in a microscopic description to its transition dipole moments $\mathbf{d}_{mn}$. These moments are the expectation values of the dipole operator for the transitions between the electronic states $|m\rangle$ and $|n\rangle$ of an atom

$$\mathbf{d}_{mn} = \langle m|\,\hat{\mathbf{d}}\,|n\rangle = e\,\langle m|\,\hat{\mathbf{r}}\,|n\rangle\ . \tag{5.14}$$

For a molecule, the initial and final states are spatially delocalised over the particle. Now, we construct a model to approximate a spatially extended polarisability. In order to describe the CASIMIR–POLDER interaction of a molecule in terms of a rigid body, a spatially-dependent polarisability is needed. To construct this polarisability, we need to note that a particle occupies a volume V, with respect to which a normalised polarisability density distribution $\varrho(\mathbf{r})$ can be defined, which has to satisfy the normalisation condition

$$\int_V \varrho(\mathbf{r})\,\mathrm{d}^3 r = 1\,. \tag{5.15}$$

In principle, such a density distribution can have any arbitrary shape. In order to describe a physically relevant system, it is useful to base its construction on the mass and electronic distribution. The assumption of a GAUSSian distribution

$$\varrho(\mathbf{r}) = \frac{1}{\mathcal{N}} \mathrm{e}^{-\left(\frac{x^2}{a^2}+\frac{y^2}{b^2}+\frac{z^2}{c^2}\right)}\,, \tag{5.16}$$

has been successfully applied in the theory of ionic liquids [PN09] with the main axes a, b and c and the normalisation factor $\mathcal{N} = \pi^{3/2}abc$. The occupied volume V of the molecule can be determined by using a quantum molecular dynamics package, such as TURBOMOLE [Turb]. The volume's surface matches the equipotential surface of the electron density set to a low threshold value. Its typical value is on the order of 10^{-3} elementary charges per cubic BOHR radius. We assume that the shape of this volume is proportional to the corresponding main axes of the polarisability $a = g\alpha_{xx}$, $b = g\alpha_{yy}$ and $c = g\alpha_{zz}$, where g is a normalisation factor and can be determined by the volume $V = 4/3\pi abc = 4/3\pi g^3 \alpha_{xx}\alpha_{yy}\alpha_{zz}$ [FS15]. For Phthalocyanine one finds the parameter $V = 4.2 \cdot 10^3\,\mathrm{a_B^3}$ (with the BOHR radius $\mathrm{a_B}$) and, together with the static polarisability tensor $\boldsymbol{\alpha}_0 = \mathrm{diag}(852, 852, 146)\, e^2\mathrm{a_B^2 E_H^{-1}}$ [RS09] ($\mathrm{E_H}$ denotes the HARTREE energy and e the elementary charge), the main axis $a = b = 17\,\mathrm{a_B}$ and $c = 3.5\,\mathrm{a_B}$ [FS15].

By introducing such a polarisability density, its spatial dependence can be constructed as a product of space- and frequency-dependent polarisabilities

$$\boldsymbol{\alpha}(\mathbf{r}, \omega) = \boldsymbol{\alpha}(\omega)\varrho(\mathbf{r})\,. \tag{5.17}$$

Hence, for each point of the particle $\mathbf{r}'$ the CASIMIR–POLDER potential can be obtained

$$U_{CP}(\mathbf{r}_A + \mathbf{r}', \boldsymbol{\Omega}) = \frac{\hbar\mu_0}{2\pi} \int_0^\infty \mathrm{d}\xi\, \xi^2\, \mathrm{Tr}\left\{\mathbf{R}^{-1}(\boldsymbol{\Omega}) \cdot \boldsymbol{\alpha}(\mathbf{r}', i\xi) \cdot \mathbf{R}(\boldsymbol{\Omega}) \right.$$
$$\left. \cdot \mathbf{G}(\mathbf{r}_A + \mathbf{R}^{-1}(\boldsymbol{\Omega})\mathbf{r}', \mathbf{r}_A + \mathbf{R}^{-1}(\boldsymbol{\Omega})\mathbf{r}', i\xi)\right\}\,, \tag{5.18}$$

where $\mathbf{r}_A$ denotes the centre of mass of the particle. The complete CASIMIR–POLDER potential then follows from an integration over the molecular volume and averaging

over all orientations

$$U_{CP}(\mathbf{r}_A) = \int\limits_V \mathrm{d}^3 r' \int \mathrm{d}\boldsymbol{\Omega}\, U_{CP}(\mathbf{r}_A + \mathbf{r}', \boldsymbol{\Omega})\,. \tag{5.19}$$

Formally, this expression resembles the first order of the Born series expansion and describes the pairwise integration of constituents of the molecule weight with the Gaussian distribution.

In the following, we analyse the impact of this averaging method for some special shapes of the molecular volume (spherical and ellipsoidal) in front of an infinite plate. After that, we take a closer look at the dynamical effects of such rotations. This is motivated by the initialisation of the molecular beam, where the heat transfer from the incoming laser field to the molecule takes place. In this section we assume a Boltzmann distributed angular momentum spectrum and take the thermal average over this distribution. At the last step of this theoretical introduction, we generalise the presented formalism for the extended molecules to the Born series expansion.

For the following scenarios we choose a separation of the polarisability into the product of a constant anisotropy, the frequency dependence and the spatial dependence

$$\boldsymbol{\alpha}(\mathbf{r}, \omega) = \boldsymbol{\alpha}^\star \cdot \alpha(\omega)\varrho(\mathbf{r})\,. \tag{5.20}$$

The Green tensor in the nonretarded limit for a half-space can be written as [FS15, SB08]

$$\mathbf{G}(\mathbf{r}_A, \mathbf{r}_A, \omega) = \frac{c^2}{32\pi\omega^2 z_A^3} \frac{\varepsilon(\omega) - 1}{\varepsilon(\omega) + 1} \operatorname{diag}(1, 1, 2)\,. \tag{5.21}$$

5.3.1 The Casimir–Polder interaction on a spherical molecule

For spherical molecules, such as fullerenes C_{60}, with a radius R the polarisability density has the simple form $\varrho(\mathbf{r}) = 1/(\pi^{3/2}a^3)\exp(-r^2/a^2)$ which only depends on the distance r from the centre of mass, and where a denotes the Gaussian radius of the electronic density. The molecular radius R is approximately related to the Gaussian radius a by $R \approx 2.5a$, because the cut-off of the electronic wavefunction is at approximately 3σ. The polarisability tensor for this case is diagonal and proportional to the identity matrix, $\boldsymbol{\alpha}(i\xi) = \alpha(i\xi)\boldsymbol{I}$.

In this situation, the rotational averaging is trivial. Only the computation of the spatial integral over the volume V remains. In spherical coordinates (r, θ, φ) and in the nonretarded limit, the Casimir–Polder potential in front of a half-space reads as [FS15]

$$U_{CP}(z_A) = \frac{\lambda}{\mathcal{N}} \int\limits_0^R \int\limits_0^\pi \int\limits_0^{2\pi} e^{-\frac{\varrho^2}{a^2}} \left(z_A + \varrho\cos\vartheta\right)^{-3} \varrho^2 \mathrm{d}\varrho\, \sin\vartheta \mathrm{d}\vartheta\, \mathrm{d}\varphi\,, \tag{5.22}$$

with the normalisation $\mathcal{N} = \pi^{3/2}a^3$ and the constant

$$\lambda = -\frac{\hbar\mu_0 c^2}{16\pi^2}\int_0^\infty d\xi\,\alpha(i\xi)\frac{\varepsilon(i\xi)-1}{\varepsilon(i\xi)+1} = U_{CP}^{\mathrm{dip}}(z_A)z_A^3 \tag{5.23}$$

which includes the electromagnetic response properties of the molecule and the surface. The function $U_{CP}^{\mathrm{dip}}(z_A)$ denotes the Casimir–Polder potential for a point-like molecule with the same polarisability. The electromagnetic and geometric properties factorise due to the process of taking a specific distance limit, the nonretarded limit, which yields a strict power law z_A^{-3}.

If one assumes that the molecular radius R is much smaller than the distance between its centre of mass and the plate, $R \ll z_A$, a Taylor expansion yields

$$\begin{aligned} U_{CP}(z_A) &= \frac{U_{CP}^{\mathrm{dip}}(z_A)}{\mathcal{N}}\sum_{n=0}^{\infty}\frac{(-1)^n(n+2)!}{2n!} \\ &\quad\times\int_0^R\int_0^{2\pi}\int_0^{\pi}\varrho^2\sin\vartheta\mathrm{e}^{-\frac{\varrho^2}{a^2}}\left(\frac{\varrho}{z_A}\right)^n\cos^n\vartheta\mathrm{d}\vartheta\mathrm{d}\varphi\mathrm{d}\varrho\,. \end{aligned} \tag{5.24}$$

Performing the integrals yields

$$\begin{aligned} U_{CP}(z_A) &= U_{CP}^{\mathrm{dip}}(z_A)\sum_{n=0}^{\infty}c_n\left(\frac{a}{z_A}\right)^n \\ &= U_{CP}^{\mathrm{dip}}(z_A)\left[1+\frac{1}{2}\left(\frac{a}{z_A}\right)^2+\frac{3}{4}\left(\frac{a}{z_A}\right)^4+\cdots\right], \end{aligned} \tag{5.25}$$

where we assumed that the error due to the upper limit of the radial integration is negligible by taking the limit $R \to \infty$.

The first term in Eq. (5.25) is the well-known Casimir–Polder potential for point dipoles. The remaining terms in the Taylor expansion are the first corrections to the Casimir–Polder potential for spherical molecules with finite size. Figure 5.4 shows the relative contributions of the first three terms in the expansion (5.25) as a function of the scaled variable z_A/R.

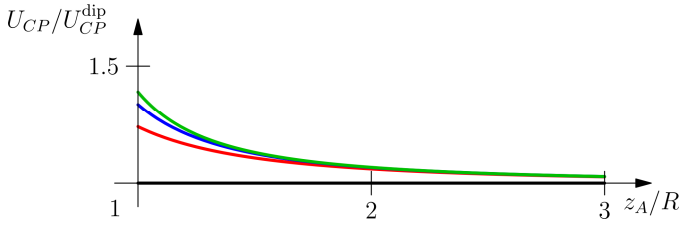

Figure 5.4: Relative contributions of the first three terms in the expansion (5.25) of the Casimir–Polder potential for a spherical molecule. The thick black line shows the Casimir–Polder potential for point dipoles. The red, green and blue lines includes the first-, second- and up to third-order corrections, respectively. Taken from [FS15].

This series converges rather quickly, even the third-order correction suffices to give good results at the closest possible approach. Their deviations from the point-dipole particles results can be as large as forty percent, but tail off rapidly for larger distances.

One observes that this correction is needed, if the typical distances between the particle and the scattering object are on the order of several molecular radii. Otherwise, the impact of the extension of the molecule is negligible and the description as point particles is valid.

5.3.2 The Casimir–Polder interaction on an ellipsoidal molecule

In the second example, we assume an ellipsoidally shaped molecule whose polarisability distribution will have the same symmetry as the molecule itself. We denote the principal axes again as a, b and c, which yields the dipole density as in Eq. (5.16). Analogously, the static polarisability is proportional to these principal axes, $\boldsymbol{\alpha}_0 = \tilde{\alpha}\,\mathrm{diag(a,b,c)}$, and its normalisation reads $\boldsymbol{\alpha}^\star = 3(a+b+c)^{-1}\tilde{\alpha}^{-1}\boldsymbol{\alpha}_0$.

In the following, we restrict ourselves to the specific case of spheroidal molecules, where two principal axes are identical, say $b = c$. Commonly, the eccentricity $e = b/a$ can be defined with $e > 1$ for oblate and $e < 1$ for prolate spheroidal molecules. Because of the rotational symmetry of the scattering Green tensor and of the polarisability tensor we use the Tail–Bryan angles as convention for the definition of the Euler angles, see Sec. 5.2. A rotation of the molecule around the roll axis leaves the interaction potential invariant due to its symmetry. The symmetry of the half-space results in an independence of a rotation around the yaw axis. This means that under the trace of the Casimir–Polder potential (5.18) and outside the Green tensor the rotation matrix (5.13) can be reduced to

$$\mathbf{R} = \begin{pmatrix} \cos\vartheta & 0 & \sin\vartheta \\ 0 & 1 & 0 \\ -\sin\vartheta & 0 & \cos\vartheta \end{pmatrix} . \tag{5.26}$$

Analogously, the rotation matrix inside the scattering Green function can be represented by the matrix product

$$\mathbf{R}^T = \begin{pmatrix} \cos\vartheta & 0 & \sin\vartheta \\ 0 & 1 & 0 \\ -\sin\vartheta & 0 & \cos\vartheta \end{pmatrix} \cdot \begin{pmatrix} \cos\varphi & \sin\varphi & 0 \\ -\sin\varphi & \cos\varphi & 0 \\ 0 & 0 & 1 \end{pmatrix} , \tag{5.27}$$

which is caused by the invariance with respect to rotations around the yaw axis. Inserting these relations into Eq. (5.18) yields the Casimir–Polder potential

$$\begin{aligned} \frac{U_{CP}(z_A)}{U_{CP}^{\mathrm{dip.}}(z_A)} &= \frac{1}{4}\int \mathrm{d}\Omega \int \mathrm{d}V \\ &\quad \times \frac{3\varrho(\mathbf{r})}{1+2e}\left[1 + \frac{(\mathbf{R}^T\cdot\mathbf{r})_z}{z_A}\right]^{-3} \mathrm{Tr}\left[\mathbf{R}^{-1}\cdot\mathrm{diag}(1,e,e)\cdot\mathbf{R}\cdot\mathrm{diag}(1,1,2)\right] . \end{aligned} \tag{5.28}$$

Performing the rotations yields for the trace term

$$\mathrm{Tr}\,[\dots] = \cos^2\vartheta(e-1) + 2(e+1)\,, \tag{5.29}$$

and the rotated relative coordinate becomes

$$\frac{(\mathbf{R}^T\cdot\mathbf{r})_z}{z_A} = \frac{a}{z_A}(e\cos\vartheta\cos\eta - \sin\vartheta\cos\eta\sin\nu)\,, \tag{5.30}$$

where we used ellipsoidal coordinates $\mathbf{r} = (a\sin\nu\cos\eta, ae\sin\nu\sin\eta, ae\cos\nu)$ with the associated volume element $\mathrm{d}V = a^2e^2\sin\eta\,\mathrm{d}a\,\mathrm{d}\eta\,\mathrm{d}\nu$. A consequence of Eq. (5.29) is that for rotation angles that satisfy $\vartheta \geq \arccos\frac{\sqrt{2(1-e^2)}}{1-e}$ the Casimir–Polder force becomes repulsive. This is valid for an eccentricity $e<1$, which means prolate spherical particles. In this notation and by using the Taylor expansion

$$\frac{1}{(1+x)^3} = \sum_{n=0}^{\infty}\frac{(-1)^n}{n!}\frac{(n+2)!}{2}x^n\,, \tag{5.31}$$

the integrand decomposes into products of trigonometric functions, which can be evaluated analytically. The correction of the Casimir–Polder potential then can be written as [FS15]

$$\begin{aligned}\frac{U_{CP}(z_A)}{U_{CP}^{\mathrm{dip.}}(z_A)} &= \frac{1}{A^3\pi^{3/2}}\frac{1}{4}\frac{3}{1+2e}\sum_{n=0}^{\infty}\frac{(-1)^n}{n!}\frac{(n+2)!}{2}\sum_{m=0}^{n}\binom{n}{m}e^m(-1)^{n-m}\\ &\quad\times\int\mathrm{d}\vartheta\,\mathrm{d}\varphi\,\left[\cos^2\vartheta\,(e-1)+2\,(e+1)\right]\sin^{n-m}\vartheta\cos^m\vartheta\\ &\quad\times\int\mathrm{d}a\,\mathrm{d}\nu\,\mathrm{d}\eta\,a^2\sin\eta\left(\frac{a}{z_A}\right)^n\mathrm{e}^{-\frac{a^2}{A^2}}\sin^{n-m}\nu\cos^n\eta = \sum_{n=0}^{\infty}c_n(e)\left(\frac{a}{z_A}\right)^n \qquad (5.32)\\ &= \frac{7e+5}{4(1+2e)} + \frac{3(39e^3+21e^2+22e+18)}{200(1+2e)}\left(\frac{a}{z_A}\right)^2+\cdots\,. \qquad (5.33)\end{aligned}$$

One observes that there is already a correction of the Casimir–Polder potential for point dipoles in analogy to the result for spherical molecules. Certainly, it stands out that the correction coefficients depend on the eccentricity e. In the limit of a sphere, it turns out that the result equals the expression in Eq. (5.25), as it should.

5.3.3 Ellipsoidal molecules with Boltzmann-distributed torques

The assumption of isotropically distributed angles is, despite its appeal owing to its simplicity, not necessarily realistic. The molecules that pass through a Casimir–Polder interaction zone are typically produced at some rotational temperature in excess of room temperature. Consequently, it is more realistic to assume thermally distributed torques rather than an isotropic angular average. As the molecular beam velocity is

typically slow enough that the rotational timescale is much shorter than the traversal time through the grating, we can replace the rotational average by the temporal average

$$\int d\Omega \mapsto \frac{1}{\tau} \int_0^\tau dt \tag{5.34}$$

where τ is the time needed for a full rotation of the molecule.

The rotational dynamics will for simplicity be computed classically. This is justified as long as the rotational temperature of the molecule is large enough such that the rotational energy levels are sufficiently close to be treated as a continuum. Hence, we solve HAMILTON's equations of motion with the classical Hamiltonian function

$$H = T_{\text{trans}} + T_{\text{rot}} + U_{CP} \,. \tag{5.35}$$

Compared with the rotational energy of a large molecule, the CASIMIR–POLDER potential can be safely neglected so that the centre-of-mass motion and the rotational dynamics completely separate, and the molecules can be treated as freely rotating particles whose dynamics are well-known [LL69].

The rotational energy T_{rot} for a symmetric top, such as a spheroidally shaped molecule, reads

$$T_{\text{rot}} = \frac{p_\vartheta^2}{2I_0} + \frac{\left(p_\varphi - \cos\vartheta p_\psi\right)^2}{2I_0 \sin^2\vartheta} + \frac{p_\psi^2}{2I_0 e_\vartheta} \,, \tag{5.36}$$

with the canonical momenta p_ϑ, p_φ and p_ψ corresponding to the Euler angles ϑ, φ and ψ, the moment of inertia I_0 and the eccentricity $e_\vartheta = I_b/I_a$ of the ellipsoid of inertia. Note that the eccentricity e associated with the dipole polarisability is not the same as the eccentricity e_ϑ associated with the mechanical rotation but they are related by $e_\vartheta = (e^2+1)/(2e^2)$.

Owing to the weakness of the CASIMIR–POLDER potential, the equation of motion can be solved for freely rotating particles which yields, after substituting $u = \cos\vartheta$, the well-known differential equation [LL69]

$$\dot{u}^2 = \left(\frac{2E}{I_0} - \frac{p_\psi^2}{e_\vartheta I_0^2}\right)\left(1-u^2\right) - \left(\frac{p_\varphi - u p_\psi}{I_0}\right)^2 \,, \tag{5.37}$$

where the total energy E and the momenta p_φ and p_ψ are conserved. The axial symmetry of the molecule implies that the rotations only depend on the pitch angle ϑ. Using this symmetry and the relation (5.37), the time average $\mathrm{d}t$ can be replaced by an average over the cosine of the pitch angle $\mathrm{d}u$,

$$\mathrm{d}t = \frac{\mathrm{d}u}{\sqrt{\left(\frac{2H}{I_0} - \frac{p_\psi^2}{e_\vartheta I_0^2}\right)\left(1-u^2\right) - \left(\frac{p_\varphi - u p_\psi}{I_0}\right)^2}} \,. \tag{5.38}$$

Inserting again the GREEN tensor for a half-space, Eq. (5.21), yields the corrected CASIMIR–POLDER potential

$$\frac{U_{CP}(z_A)}{U_{CP}^{\mathrm{dip}}(z_A)} = \left(\frac{I_0}{2\pi\beta}\right)^{3/2} \frac{1}{\sqrt{e_\vartheta}} \int \mathrm{d}^3p\, \mathrm{e}^{-\beta H} \int_0^\tau \frac{dt}{\tau} \int \mathrm{d}^3\varrho\, \frac{3\eta(\varrho)}{4(1+2e)} \left[1 + \frac{(\mathbf{R}(t)\cdot\boldsymbol{\varrho})_z}{z_A}\right]^{-3} \times \mathrm{Tr}\left[\mathbf{R}^{-1}(t)\cdot\mathrm{diag}(1,e,e)\cdot\mathbf{R}(t)\cdot\mathrm{diag}(1,1,2)\right] . \tag{5.39}$$

Because of the conservation of total energy, the Hamiltonian can be evaluated at $\vartheta = \pi$ as $H = (p_\vartheta^2 + p_\varphi^2 + p_\psi^2/e_\vartheta)/(2I_0)$, which means that the angular momenta enter the average function only parametrically. Consequently, by performing the transformation of the three-dimensional momenta into ellipsoidal coordinates $\{p, \nu, \eta\}$ ($p_1 = p_\vartheta\sqrt{\beta/(2I_0)} \equiv p\sin\nu\cos\eta$, $p_2 = p_\varphi\sqrt{\beta/2I_0} \equiv p\sin\nu\sin\eta$ and $p_3 = p_\psi\sqrt{\beta/(2I_0 e_\vartheta)} \equiv p\cos\nu$), the dependence of the moment of inertia I_0 and β factorise in the differential $\mathrm{d}u$ in Eq. (5.38). Hence, the average time τ can be computed by evaluating the integral

$$\tau = \int_{u_1}^{u_2} \frac{\mathrm{d}u}{\sqrt{\left(\frac{2H}{I_0} - \frac{p_\psi^2}{e_\vartheta I_0^2}\right)(1-u^2) - \left(\frac{p_\varphi - u p_\psi}{I_0}\right)^2}} , \tag{5.40}$$

where u_1 and u_2 are the classical turning points, i.e. the roots of the denominator in Eq. (5.40) for a complete rotation. This means that the time average can be carried out using

$$\frac{1}{\tau}\int_0^\tau f\left[\cos\vartheta(t)\right]\mathrm{d}t \mapsto \frac{\int_{-1}^{1} f(u)\,(1-u^2)^{-1/2}\,\mathrm{d}u}{\int_{-1}^{1}(1-u^2)^{-1/2}\,\mathrm{d}u} , \tag{5.41}$$

with the result that the average over the momenta $\mathbf{p}$ separates from the dynamical, rotational average and, subsequently, the correction to the CASIMIR–POLDER potential is independent of temperature as well as the moment of inertia.

This cancellation is a direct consequence of assuming a weak CASIMIR–POLDER potential and the subsequent treatment of freely rotating molecules. By relaxing this assumption one has to change the total energy of the system to $H \mapsto H + U_{CP}$ in Eq. (5.38), with U_{CP} from Eq. (5.11), upon which the integrals no longer separate. In this case, Eq. (5.39) has to be solved numerically.

Another consequence of this calculation is that in the case of short interaction times the temperature-dependence will cancel as well. If the molecule does not accomplish a full rotation, the averaged time τ' will be shorter than the rotation time τ, which means that the integration ranges in Eqs. (5.40) and (5.41) have to be changed to $u \in [u_1, \tilde{u}]$ with $\tilde{u} \leq u_2$ and $t \in [-1, a]$ with $a \leq 1$, respectively.

5.4 The Born series expansion for extended and rotating molecules

In the previous sections the correction of the Casimir–Polder potential due to rotational and temporal averaging of extended molecules has been discussed for the specific situation of its interaction with a half-space, which is not a good approximation in most experimental situations. Therefore, it is helpful to investigate the perturbative expansion of the Green tensor in terms of the Born series (see Sec. 3.5.2).

The spatial extent of a distributed dipole polarisability can be translated into 'blurred' spatial arguments of the scattering Green function which can be expressed by the integral kernel [FS15]

$$\begin{aligned}\mathbf{\Lambda}(\mathbf{r}_A,\mathbf{s},\mathbf{s}',\omega) = \frac{\omega^2}{c^2}\int \mathrm{d}\Omega \int \mathrm{d}V\, \varrho(\mathbf{r})\mathbf{R}(\Omega) \\ \cdot\mathbf{G}_0\left[\mathbf{r}_A + \mathbf{R}^{-1}(\Omega)\cdot\mathbf{r},\mathbf{s},\omega\right]\otimes\mathbf{G}_0\left[\mathbf{s}',\mathbf{r}_A + \mathbf{R}^{-1}(\Omega)\cdot\mathbf{r},\omega\right]\cdot\mathbf{R}^{-1}(\Omega)\,. \end{aligned} \tag{5.42}$$

With the help of this fourth-rank tensor function $\mathbf{\Lambda}(\mathbf{r}_A,\mathbf{s},\mathbf{s}',\omega)$, the Born series for the Green function of extended and rotating molecules reads as [FS15]

$$\begin{aligned}&\mathbf{G}^{(S)}(\mathbf{r}_A,\mathbf{r}_A,\omega) = \\ &\int d^3s\, d^3s'\, \mathbf{\Lambda}(\mathbf{r}_A,\mathbf{s},\mathbf{s}',\omega) : \Bigg[\delta\varepsilon(\mathbf{s},\omega)\boldsymbol{\delta}(\mathbf{s}-\mathbf{s}') + \frac{\omega^2}{c^2}\delta\varepsilon(\mathbf{s})\mathbf{G}_0(\mathbf{s},\mathbf{s}',\omega)\delta\varepsilon(\mathbf{s}',\omega) \\ &+\left(\frac{\omega^2}{c^2}\right)^2\int d^3s''\delta\varepsilon(\mathbf{s},\omega)\mathbf{G}_0(\mathbf{s},\mathbf{s}'',\omega)\delta\varepsilon(\mathbf{s}'',\omega)\cdot\mathbf{G}_0(\mathbf{s}'',\mathbf{s}',\omega)\delta\varepsilon(\mathbf{s}',\omega)+\cdots\Bigg]\,,\end{aligned} \tag{5.43}$$

where the notation ':' denotes the contraction $(A:x)_{ij} = A_{imnj}x_{mn}$ with the inner two indices of the fourth-rank tensor.

If the reference Green function $\mathbf{G}_0$ refers to a spatially homogeneous medium, e.g. a bulk material or free space, see Sec. 3.5.1, it is itself translationally invariant, i.e. $\mathbf{G}_0(\mathbf{r},\mathbf{s}) = \mathbf{G}_0(\mathbf{r}-\mathbf{s})$. In such situations it can be assumed that the extention of the blurred source point $\mathbf{r}_A + \mathbf{R}^{-1}(\mathbf{\Omega})\cdot\mathbf{r}$ is small compared with the propagation length $|\mathbf{s}-\mathbf{r}_A|$ which means that the Green function can be expanded in a Taylor series

$$\mathbf{G}_0(\mathbf{r}_A + \mathbf{R}^{-1}(\Omega)\cdot\mathbf{r}-\mathbf{s}) \approxeq \mathbf{G}_0(\mathbf{r}_A-\mathbf{s}) + \frac{\partial\mathbf{G}_0(\mathbf{r}_A-\mathbf{s})}{\partial x_k}\left(\mathbf{R}^{-1}(\Omega)\cdot\mathbf{r}\right)_k\,. \tag{5.44}$$

After the expansion of the rotated argument of the Green function, the integral kernel (5.42) consists of elementary integrals, which can be evaluated analytically. Inserting

the series expansion into Eq. (5.42) yields [FS15]

$$\begin{aligned}\Lambda_{ijkl}(\mathbf{r}_A,\mathbf{s},\mathbf{s}',\omega) = \frac{\omega^2}{c^2}\int \mathrm{d}\Omega \int \mathrm{d}^3 r\, \varrho(\mathbf{r}) R_{i\mu}(\Omega) \\ \times \left[G^{(0)}_{\mu j}(\mathbf{r}_A-\mathbf{s},\omega) + \left(\partial_\kappa G^{(0)}_{\mu j}(\mathbf{r}_A-\mathbf{s},\omega)\right) R_{\kappa\sigma}(\Omega) r_\sigma\right] \\ \times \left[G^{(0)}_{k\nu}(\mathbf{r}_A-\mathbf{s},\omega) + \left(\partial_\kappa G^{(0)}_{k\nu}(\mathbf{r}_A-\mathbf{s},\omega)\right) R_{\kappa\sigma}(\Omega) r_\sigma\right] R_{l\nu}(\Omega)\,, \end{aligned} \tag{5.45}$$

where we made use of Einstein's summation convention. This integral can be computed analytically, because the Green tensors are not affected by it. Hence, this integral consists, for a given reference Green function, only of elementary integrals. The numerical effort for computing the complete modified Born series is thus equivalent to that for non-rotating particles.

5.5 Application: Diffraction at a square wire

In order to illustrate the influence of the presented effect, a typical experimental setup for the interference with molecules [TJ12] will be shown. Here, the simplest setup, in which a molecular beam is diffracted off a single wire with square cross-section, will be assumed. For the calculation of the resulting interference pattern $P(x)$ on the screen, the Kirchhoff diffraction integral (see Sec. 2.3) is used.

In this situation, the transmission function is taken to be $t(x) = 1$ for points outside the wire and $t(x) = 0$ for points within the wire. For simplicity, a one-dimensional scattering process was assumed. The Casimir–Polder potential entering the Kirchhoff diffraction integral is given by an additional phase shift, which is accumulated by the transition of the particles by the wire $t(x') \mapsto t(x')\mathrm{e}^{i\varphi(x')}$ with the phase $\varphi(x') = U_{CP}(x')d/(\hbar v)$ [JDP05, JDP06], where d denotes the thickness of the grating and v the velocity of the particles. Here, the approach and the departure of the molecule from the scattering object was neglected, which gives rise to the following approximations. First, the interference pattern is evaluated by the Kirchhoff integral in the far-field limit, in which the distances between source and grating and between grating and screen of 1 m ($L_1 = L_2 = 1\,\mathrm{m}$) was assumed. Second, we employ the eikonal approximation and correct the interference pattern by the presented rotational average method. Again, the dye molecule Phthalocyanine has been chosen with a mass of 514a.u., which, at a velocity of 200 m/s, yields a de Broglie wavelength $\lambda_{\mathrm{dB}} = 3.8$ pm. The diffraction wire is taken to be a square wire with an edge length of $d = 250$ nm made of a dielectric material. The Casimir–Polder potential is assumed to be in the nonretarded limit in front of an infinite plate. The correction of the Casimir–Polder potential for spatially extended particles plays a major role in short distances to the

dielectric object. Thus, we consider the nonretarded regime. In this case the spatial and frequency dependencies of CASIMIR–POLDER potential, Eq. (3.55), separate and one finds

$$U_{CP}(z_A) = -\frac{C_3}{z_A^3}\,, \tag{5.46}$$

with the C_3 coefficient, which involves the dielectric properties of the plate and the molecule

$$C_3 = \frac{\hbar}{16\pi^2\varepsilon_0}\int_0^\infty \alpha(\omega)\frac{\epsilon(\omega)-1}{\epsilon(\omega)+1}\,\mathrm{d}\omega\,. \tag{5.47}$$

Typical values of such C_3 coefficients are in the range $C_3 = 1\ldots 20\,\mathrm{meV(nm)}^3$ for atoms in front of a dielectric surface. We consider a large and extended molecule, taking a C_3-coefficient of $C_3 = 200\,\mathrm{meV(nm)}^3$, which is a typical value for a weakly conductive surface and a nonpolar molecule [BF15]. The transmission function then reads [FS15]

$$t(x') = \Theta(|x'|-d/2)\exp\left\{-i\frac{C_3 d}{\hbar v}\frac{1}{(|x'|-d/2)^3}\right\} \tag{5.48}$$

for point dipoles and [FS15]

$$t(x') = \Theta(|x'|-d/2)\exp\left\{-i\frac{C_3 d}{\hbar v}\frac{1}{(|x'|-d/2)^3}\left(0.9+4.9\left[\frac{a}{(|x|-d/2)}\right]^2\right)\right\}\,, \tag{5.49}$$

with $a = 17a_0 = 0.9\mathrm{nm}$ for the extended molecule [BF15].

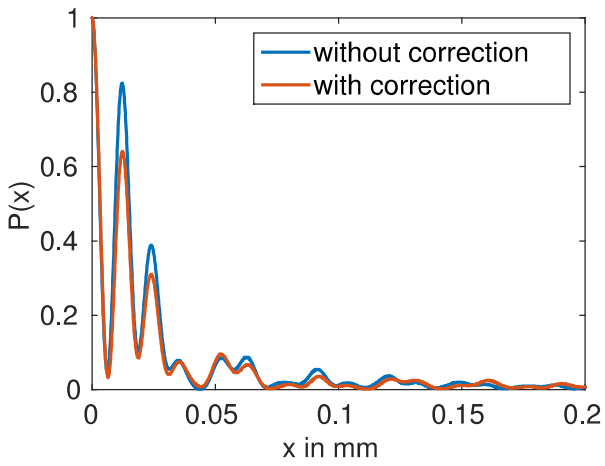

Figure 5.5: Expected interference pattern with (red) and without (blue) correction due to finite size of the molecule. Taken from [FS15]

Figure 5.5 shows the expected interference patterns for the diffraction at a wire with and without the finite-size correction. One observes the POISSON spot arising at the origin of the interference pattern. Two results can be obtained from this picture. On the one hand, one can see a decrease of the intensity of the lower diffraction orders by up to twenty percent if the finite extent of the molecule is taken into account. On the other hand, for higher diffraction orders a spatial shift of the minima and maxima of the interference pattern is observable. These effects scale with the strength of the potential. They increase with increasing C_3-coefficients. This means that these corrections become even more important for semiconducting or metallic wires.

chapter 6

Analysis of the interference patterns

We will apply the theory developed in the previous chapters to a specific set of experimental data. The emergence of the interference patterns will be described with KIRCHHOFF's diffraction integral. First, the transmission function of the grating is needed. Its absolute value can be represented by a periodic step function, the periodicity p and the opening fraction f of the gratings

$$|t(z)| = \sum_n \Theta\left[z - (n + 1 - f)p\right] \Theta\left[np - z\right] , \tag{6.1}$$

where $\Theta[x]$ denotes the HEAVISIDE function. The used parameters are given in table 6.1. The grating bars are assumed to be infinitely long. We denote it by x. The particles pass the apparatus along the y-direction which is parallel to the surface of the earth. Thus, the transmission function only depends on one coordinate, which we denote by z. Hence, the interference pattern is automatically velocity-selected by the gravitational force. Slower molecules will remain longer in the apparatus, which means that, due to the gravitational force, their path will deviate from the horizontal in analogy to the ballistic trajectory of a projectile. In the formulation with the KIRCHHOFF integral, the longitudinal transmission through the grating is projected onto an infinitely small transversal plane. The phase of the transmission function can be obtained by this projection of the CASIMIR–POLDER potential which yields, together with the eikonal approximation, Eq. (2.6),

$$\arg\left[t(z)\right] = -\frac{1}{\hbar v_\parallel} \int_{-\infty}^{\infty} U_{CP}(y, z)\, \mathrm{d}y = \varphi(z) . \tag{6.2}$$

In the following, the results of our theory and their comparison with the experimental data will be presented.

6.1 Experimental data

In the experiment, which was performed in the group of Markus Arndt at the University of Vienna [TJ12, BF15], five different gratings have been used, for details see table 6.1. All gratings have the same periodicity of $p = 100\,\text{nm}$. Figure 6.1 illustrates the geometry of the grating, where d is the grating thickness, T_1 is the largest width of the grating bar and T_2 is the grating opening. The ratio

$$f = \frac{T_2}{p} = \frac{T_2}{T_1 + T_2}\,, \tag{6.3}$$

relates the vertical grating constants to the opening fraction f.

Grating	material	thickness d[nm]	opening fraction f	Wedge angle α[°]
G1	SiN_x	10	0.46	50
G2	SiN_x	46	0.46	17
G3	SiN_x	10	0.79	33
G4	SiN_x	87	0.57	10
G5	C	20	0.68	19

Table 6.1: Geometry and material of the used gratings, the first column enumerates the gratings, the second the material and the last three contain the geometric dimensions, the thickness d, the opening fraction f and the wedge angle α

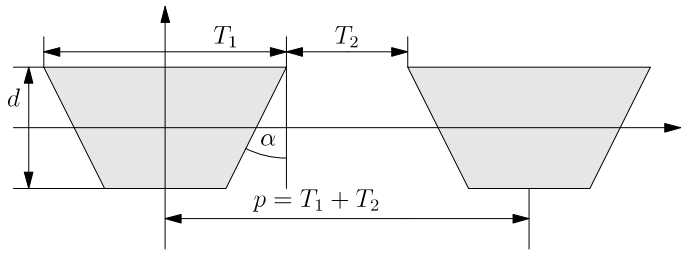

Figure 6.1: Sketch of the cross section area of two grating bars with thickness d, a shortest grating opening T_1, the longest width of a grating bar is denoted by T_2 and a wedge angle α. The sum of T_1 and T_2 defines the periodicity p of the grating.

Figure 6.1 illustrates the cross section of the grating bars. One observes that they are trapezoidal, which is caused by their production process. Their analysis with an electron microscope yields the wedge angles, which are given in Table 6.1. These angles causes on the one hand difficulties in the numerical treatment of the Casimir–Polder potential, whereas, on the other hand, they provide the convergence of the Born series, because they suppress resonances of electromagnetic waves between the grating bars. Hence, for the calculation of the Casimir–Polder potential it is sufficient to take into account the first order of the Born series.

Two different materials have been used for the gratings. One is amorphous silicon nitride SiN_x with an unknown stoichiometry, which is caused by the production process of the wafer. Such wavers are mechanically unstable and they have to be stabilised by the inflow of nitrogen, which can dramatically influence the optical properties. To describe its dielectric susceptibility we used the simplified model [BF15]

$$\operatorname{Im}\varepsilon(\omega) = \Theta(\omega - \Omega_T)\frac{f\Omega\gamma(\omega-\Omega_T)^2}{[(\omega^2-\Omega^2)^2+\gamma^2\omega^2]\omega}\,, \tag{6.4}$$

with the parameters $\Omega_T = 3.48\cdot10^{15}$ rad/s, $\Omega = 1.09\cdot10^{16}$ rad/s, $f = 1.13\cdot10^{17}$ rad/s, and $\gamma = 1.16\cdot10^{16}$ rad/s. In order to convert the imaginary part of the permittivity at real frequencies to the permittivity at imaginary frequencies, we use the Kramers-Kronig relation [BS12], see Sec. 3.2,

$$\chi(i\xi) = \varepsilon(i\xi) - 1 = \frac{2}{\pi}\int_0^\infty d\omega \frac{\omega \operatorname{Im}\varepsilon(\omega)}{\omega^2+\xi^2}\,. \tag{6.5}$$

For the dielectric susceptibility of the amorphous carbon grating (graphite grating) we used the model from Ref. [RH97]. This model is separated into two parts: one representing the electric transitions and one describing the vibrational transitions by a Lorentz model [RH97]

$$\varepsilon(\omega) = \varepsilon_\infty + \frac{S\omega_T^2}{\omega_T^2-\omega^2-i\Gamma\omega}\,, \tag{6.6}$$

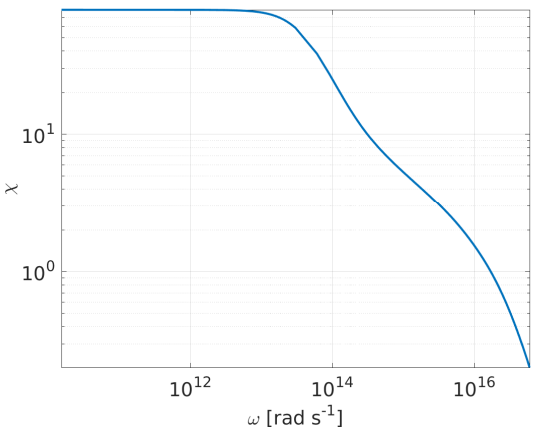

Figure 6.2: Plot of the susceptibility $\chi(\omega)$ for the graphite grating.

where the oscillator strength S, the phonon frequency ω_T, the phenomenological damping constant Γ and the dielectric function ε_∞. The values found for the dielectric function depend on the orientation of the electromagnetic field, parallel ($\parallel$) and perpendicular ($\perp$) [RH97]. The corresponding parameters are tabulated in Table 6.2. The dielectric function ε_∞ determines the electric transitions and is based on experimental measurements, see App. A.

By applying the Kramers–Kronig relation, Eq. (6.5), the dielectric function for graphite can be turned to the imaginary frequency axis separately for the different orientations and result in $\chi_\parallel(i\xi)$ and $\chi_\perp(i\xi)$. An amorphous material is described by an isotropic dielectric function. In order to apply these data we average both quantities via the geometric mean

$$\chi_C(i\xi) = \sqrt{\chi_\parallel(i\xi)\chi_\perp(i\xi)}\,, \tag{6.7}$$

orientation	S	ω_T [rad/s]	Γ [rad/s]	ε_∞
$\parallel$	0.004	$1.634 \cdot 10^{14}$	$1.89 \cdot 10^{8}$	5.78
$\perp$	0.031	$2.99 \cdot 10^{14}$	$5.65 \cdot 10^{8}$	$\varepsilon_\infty(\omega)$

Table 6.2: Parameters for the dielectric function for amorphous carbon, depending on the orientation: S denotes the oscillator strength, ω_T the phonon frequency, Γ the damping constant. The dielectric constant ε_∞ is a real constant for parallel, for perpendicular it depends on the frequency. See App. A.

which is plotted in Fig. 6.2. The data in Ref. [RH97] are limited to the frequency range $[0.02, 40]\,\mathrm{eV}$.

The molecular beam is created either by a thermalisation in an oven or by laser evaporation of the molecules. Hence, their velocities, respectively their de-Broglie wave length, are thermally (Boltzmann) distributed. However, this property of the matter wave can be used to get multiple measurements by a horizontal arrangement of the experimental setup, as it will be explained in Sec. 6.3.

6.2 Calculation of Casimir–Polder potentials for the experiments

In this chapter we will apply the presented theory for the estimation of the Casimir–Polder potential to an experimental realisation. Therefore we use the established theory (Chapter 3), together with the local-field-corrected Born series expansion (Chapter 4) and the rotational averaging method (Chapter 5).

6.2.1 Evaluation method

For the evaluation of the interference patterns, we use Kirchhoff's diffraction formula. Any potential mismatch between the theory and the experiment will be covered by a fitting factor η.

$$P(z') = \frac{a_0^2 k^2}{4\pi^2} \left| \int |t(\tilde{z})| \, \mathrm{e}^{i\eta\varphi(\tilde{z})} \frac{\mathrm{e}^{ik\left(\sqrt{L_1^2+(\tilde{z}-z)^2}+\sqrt{L_2^2+(z'-\tilde{z})^2}\right)}}{\sqrt{L_1^2+(\tilde{z}-z)^2}\sqrt{L_2^2+(z'-\tilde{z})^2}} \mathrm{d}\tilde{z} \right|^2 . \tag{6.8}$$

A least-squares fit of the measured interference pattern and the Kirchhoff's diffraction formula yields a measure for the quality of the calculated Casimir–Polder potential compared to the experiment.

6.2.2 Preliminary considerations

First, we take a closer look at the material properties. To do so, we calculate the Casimir–Polder potential for Phthalocyanine in front of an infinite halfspace. The result is shown in Fig. 6.3 and follows from the integral [SYB12-I]

$$U_{CP}(z_A) = \frac{\hbar\mu_0}{8\pi^2}\int_0^\infty \mathrm{d}\xi\, \xi^2\alpha(i\xi) \times \int_{\xi/c}^\infty \mathrm{d}\kappa_\perp\, \mathrm{e}^{-2\kappa_\perp z_A}\left[\frac{\kappa_\perp-\kappa'_\perp}{\kappa_\perp+\kappa'_\perp} + \left(1-2\frac{\kappa_\perp^2 c^2}{\xi^2}\right)\frac{(\chi(i\xi)+1)\kappa_\perp-\kappa'_\perp}{(\chi(i\xi)+1)\kappa_\perp+\kappa'_\perp}\right], \tag{6.9}$$

with the length of the perpendicular wave vector $\kappa_\perp$, which is related to the wave vector inside the material $\kappa'_\perp = \sqrt{\chi(i\xi)\xi^2/c^2+\kappa_\perp^2}$. For small distances, where the condition $n(\omega_{\max})z_A \ll c/\omega_{\max}$ is satisfied, where $n(\omega) = \sqrt{\varepsilon(\omega)\mu(\omega)}$ denotes the refractive index and $\omega_{\max}$ the maximum of all relevant particle and medium resonance frequencies, one finds the nonretarded asymptotic behaviour of the Casimir–Polder potential [SB08, SYB12-I]

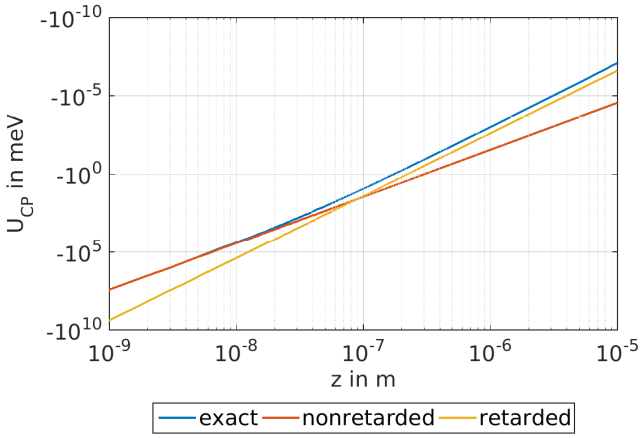

Figure 6.3: Casimir–Polder potential in front of an infinite plate, exact potential (blue), C_3 potential (red) and C_4 potential (yellow).

$$U_{CP}(z_A) = -\frac{C_3}{z_A^3}, \qquad C_3 = \frac{\hbar}{16\pi^2\varepsilon_0}\int_0^\infty \alpha(i\xi)\frac{\varepsilon(i\xi)-1}{\varepsilon(i\xi)+1}\,\mathrm{d}\xi\,. \tag{6.10}$$

On the other hand, for large distances $n(\omega_{\max})z_A \gg c/\omega_{\max}$, where the propagation time of the virtual photon has to be taken into account, one finds the asymptotic law [SB08, SYB12-I]

$$U_{CP}(z_A) = -\frac{C_4}{z_A^4}, \qquad C_4 = \frac{23\hbar c}{640\pi^2\varepsilon_0}\alpha(0)\chi(0)\,, \tag{6.11}$$

which is known as the retarded Casimir–Polder potential. Figure 6.3 illustrates the Casimir–Polder potential for Phthalocyanine in front of a silicon nitride wall. It can be seen that the near field regime, i.e. the nonretarded C_3-potential, is limited to regions very close to the wall, up to at most 10 nm. The validity of the far-field approximation starts relatively late, so that the intermediate range occupies a large region. Consequently, a purely retarded or nonretarded limit does not match the relevant

regime of the experiment, hence the full description of the scattering GREEN function is needed.

Rotation of the molecule

In the next step, we consider the rotation of the molecule. The moment of inertia of Phthalocyanine along the main rotation axes are [MS13]

$$\boldsymbol{\Theta} = \mathrm{diag}\,(1,1,2) \times 8.3 \cdot 10^{-44}\,\mathrm{kg\,m^2}\,, \tag{6.12}$$

which can be obtained from a quantum dynamics simulation, as implemented in the software package TURBOMOLE [Turb]. By comparison of the rotational energy with the thermal energy, assuming an average temperature $T = 600\,\mathrm{K}$ [MS13, BF15], the rotation time yields approximately

$$\tau_{xx} = \tau_{yy} \approx 20\,\mathrm{ps}\,, \qquad \tau_{zz} \approx 28\,\mathrm{ps}\,. \tag{6.13}$$

As mentioned above (see Sec. 5.2), a comparison with the interaction time determines the averaging method. The shortest interaction time can be evaluated as the translational time for the fastest molecule travelling at $v = 250\,\mathrm{ms^{-1}}$ [BF15] inside the thinnest grating 10 nm, see Table 6.1 and Refs. [TJ12, BF15]. In this case, an interaction time of $\tau_{int} = 40\,\mathrm{ps}$ is estimated. Hence, the interaction time scale is larger than the rotational time, and the molecule performs more than one rotation inside the grating which means that the rotationally averaged CASIMIR–POLDER potential describes this situation adequately.

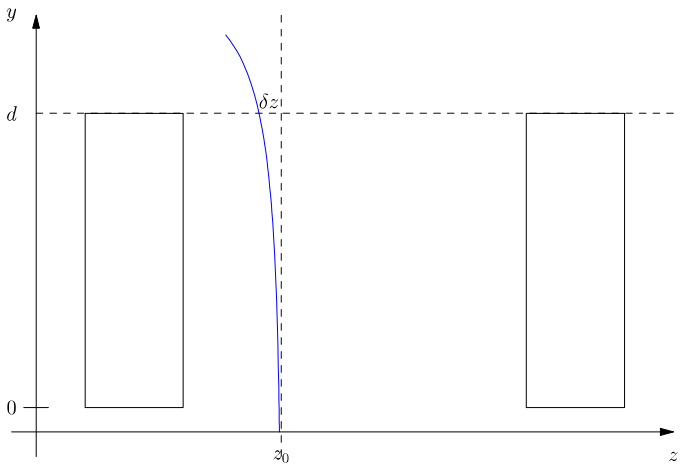

Figure 6.4: Trajectory of the particle of passing the grating.

Shortest distances to the grating walls

In addition, an important aspect is the shortest distance at which a molecule passes the grating. For that, we consider a point particle of mass m flying parallel to a finite plate in the y-direction with the velocity v_y. The arrival at and departure from the plate is neglected. The CASIMIR–POLDER force perpendicular to the plate acts on the particle and accelerates it in the z-direction towards the plate, see Fig. 6.4. We assume a nonretarded potential, as we are interested only in the shortest distance.

The trajectory of the particle can be evaluated by NEWTON's equation of motion

$$m\ddot{z} = -\frac{3C_3}{z^4} \tag{6.14}$$

with the initial conditions $z(0) = z_0$ and $\dot{z}(0) = 0$. The force is homogeneous across the plate and the interaction time is given by the longitudinal extension of the plate d and the initial velocity v_y, $\tau = d/v_y$. A subtle point concerns the deviation at the end of the plate $\tan\alpha = \dot{z}(\tau)/v_y$. The largest deviation angle is given by the scattering geometry as the ratio between the spatial extension of the detector and the distance the molecule propagates, which is approximately 0.3 mrad. For its estimation, we numerically evaluated the shortest distance z_0 to the grating bar depending on the parameter mass m, potential strength C_3, longitudinal velocity v_y, grating thickness d and the cut-off angle α.

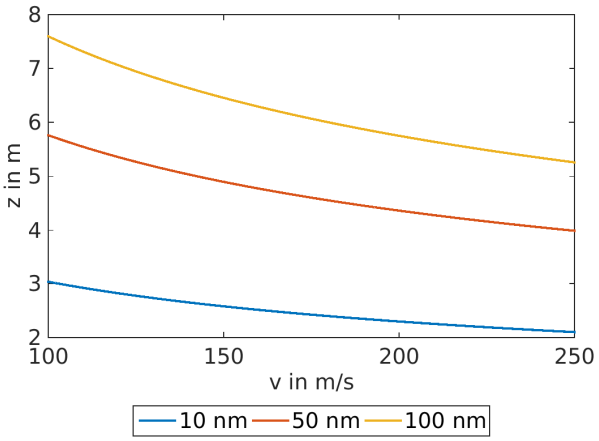

Figure 6.5: Cutoff distances depending on the velocity for three grating thicknesses: 10 nm (blue), 50 nm (red), 100 nm (yellow).

We denote this method as a cutoff, because it defines the shortest distances to the grating, which particles can reach and can be measured on the screen. Phase shifts that are accumulated in regions closer to the grating, are not measured in these experiments, due to their strong deviation from the optical axis, and so their considerations in the analysis of the interference patterns would be nonphysical. With respect to the analysis method, which is a fitting routine and compares the expected interference patterns with the measurements, we add a factor η, which scales the potential strength. Figure 6.5 illustrates the cutoff, the shortest distances, which can be reached from the molecules, as function of the velocity.

First-order of the Born series

In a first step, we apply the first order of the BORN series expansion, see Sec. 3.5.2, to a rectangular grating. We assumed the non-retarded free-space GREEN function to estimate the influence of the shape of the scattering object. Figure 6.6 (left) illustrates the landscape of such potential. One observes a curvature of the edges of the grating bar in analogy to the classical superposition of wave. Far away from the grating, it can be seen that the potential is similar to one appearing from a plane and the periodic structure vanishes. By using this method two more effects can by considered - the

influence of a wedge angle and the the influence of surface roughness, which will be treated in the following.

Influence of wedge angles

An important aspect is the wedge angle of the grating bar. Figure 6.6 (right) illustrates the dependency of the phase due to such an angle for a thick grating. It can be seen that its influence is more than an expected shift, it also influences the shape of the marginal potential. It can be observed that depending on the wedge angle the strength of the phase decreases and the result also changes the power law. The strong shift compared with the non rotated surface is due to the integral along the trajectories of the particles. In case of a non sloped surface the trajectories follow the equipotential lines and results in a $1/r^3$ depend. In all other cases this slope yields a decrease of the potential and results in different power laws. Hence, the calculations strongly depends on the correct wedge angle.

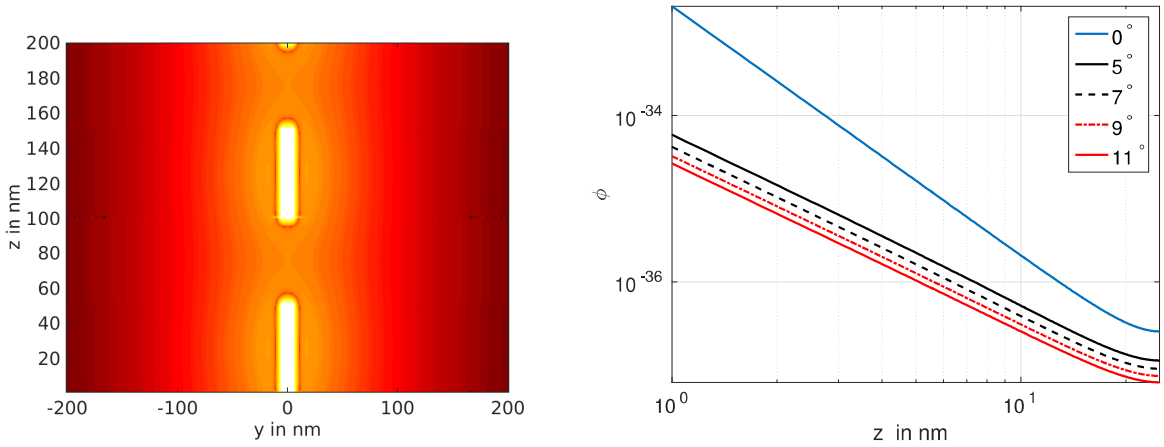

Figure 6.6: Contour plot of the Casimir–Polder potential for a rectangular grating of thickness 10 nm and opening fraction 0.5 (left). Phase depending on the wedge angle for a grating bar of 200 nm thickness (right).

Surface roughness

A rough surface appears as the boundary of the integration volume. Hence, we take a close look at surface roughness. Here, we again use the first order Born approximation and model a periodic surface structure, as shown in Fig. 6.7. We consider a surface of a refractive grating, where the surface is periodically covered with rectangular stripes, similar to the experiments in Sec. 4.3. We modeled the surface with a periodic step function, changed the periodicity and analysed the distance of the influence of such structured surfaces. We assumed a roughness with an rms of 1 nm. It can be seen

in Fig. 6.7 (left) that for large spatial frequencies the effect of the surface roughness vanishes for relatively small distances (around 4 nm). However, in case of low spatial frequencies (right picture in Fig. 6.7), the influence of this surface roughness is still measurable at distances larger than 4 nm.

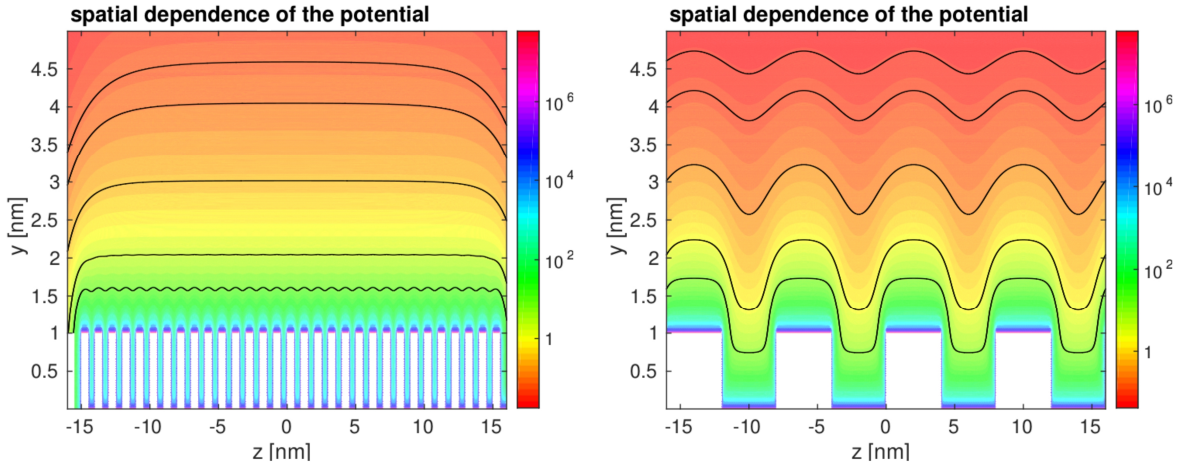

Figure 6.7: Potential landscape in front of a periodic surface with large spatial frequency (left) and low spatial frequency (right).

Summarising these effects it can be concluded that the effect of the surface roughness can be neglected. For the potential integrated along the trajectories of the particles, it can be seen that for large wedge angles this potential is relevant only in a very small (point-like) region. The wedge angle dominates the impact of the surface roughness.

6.2.3 Combination of all effects contributing to the Casimir–Polder potential

We calculated the Casimir–Polder potential for Phthalocyanine, using the product ansatz for the polarisability $\boldsymbol{\alpha}(\mathbf{r}, i\xi) = \tilde{\boldsymbol{\alpha}}(i\xi) \cdot \varrho(\mathbf{r})$, with the polarisability tensor for imaginary frequencies, $\tilde{\boldsymbol{\alpha}}(i\xi)$, from the quantum dynamics simulation.[1] To model the extension of the molecule we used the Gaussian spatial density $\varrho(\mathbf{r})$, introduced in Sec. 5.3, with the parameters noted in Sec. 5.1. To include thermal effects, we assumed an internal temperature $T = 600\,\mathrm{K}$ of the molecules and an environmental temperature of $T_{env} = 300\,\mathrm{K}$. Here, we used Eqs. (3.64)-(3.66) to compute the Casimir–Polder potentials. The dye molecule is dominated by electronic transitions in the visible range of the electromagnetic spectrum. Hence, the lowest electronic excitation will be located in the infrared range which has an upper boundary at a wavelength of around 800 mn. By treating this wavelength as a thermal wavelength, it corresponds to a temperature

[1] The quantum dynamics simulation was done by Olga Bokareva.

of around 2500 K. Thus, a thermal population of any excited state can only be accomplished for temperatures larger than this threshold value. This leads us to treat the polarisabilities for the excited state to be the ground-state polarisability.

In a similar way we treat the resonant part of the Casimir–Polder potential, which involves the dipole transitions based on the quantum chemical simulation, Fig. 5.3 (b). The scattering Green tensor was again computed by the Born series expansion up to the first order and we applied the local-field correction introduced in Sec. 4.1. We evaluated the resonant with the dipole transitions and found that its contribution to the Casimir–Polder potential is negligibly small. Figure 5.3 (b) illustrates these transitions from ground to the first excited state which are dominated by vibrational transitions.

For the rest of this chapter, only the marginal distribution of the potential $\tilde{U} = \int U \mathrm{d}y$ is needed, Eq. (6.2), which is given by the integration of the potential U along the longitudinal y-direction. Note that $\tilde{U}_{CP}(z)$ does no longer have the physical unit of a potential, though we keep calling it that for simplicity.

After discussing the retardation effects, the motion of the molecule, surface roughness and the measurability of the particles, we consider the impact of the higher orders of the Born series expansion and point out the deviation of the approach compared with the exact solution. For this, let us consider a Phthalocyanine molecule located in front of an infinite half-space made of silicon nitride. We chose this arrangement due to its analytically known solution for the scattering Green tensor. We restrict ourselves to the nonretarded regime due to the fact that the influence of the higher orders of the Born series expansion is stronger there than in the retarded region. Both methods, the exact solution and the approach, yield a C_3-potential in that region with different C_3-coefficients. The ratio between both leads to the correction factor [BF15]

$$\gamma = \frac{3\int\limits_0^\infty \mathrm{d}\xi \alpha(i\xi)\frac{\varepsilon(i\xi)-1}{\varepsilon(i\xi)+2}}{2\int\limits_0^\infty \mathrm{d}\xi \alpha(i\xi)\frac{\varepsilon(i\xi)-1}{\varepsilon(i\xi)+1}} \approx 1.1799 \tag{6.15}$$

as the ratio between the exact Casimir–Polder potential for an infinite plate [SYB12-I]

$$U_{CP}(z) = -\frac{\hbar}{16\pi^2\varepsilon_0 z^3}\int\limits_0^\infty \alpha(i\xi)\frac{\varepsilon(i\xi)-1}{\varepsilon(i\xi)+1}\,\mathrm{d}\xi\,, \tag{6.16}$$

and the potential in first order of the Born series

$$U_{CP}^{(1)}(z) = -\frac{3\hbar\mu_0 c^2}{32\pi^2 z^3}\int\limits_0^\infty \mathrm{d}\xi \alpha(i\xi)\frac{\varepsilon(i\xi)-1}{\varepsilon(i\xi)+2}\,. \tag{6.17}$$

We estimate the CASIMIR–POLDER potential via the calculation of the scattering GREEN tensor in the local-field corrected approach, see Sec. 4.1,

$$\mathbf{G}(\mathbf{r}_A, \mathbf{r}_A, i\xi_j) = \frac{\chi(i\xi)}{1+\chi(i\xi)/3} \int_V \mathrm{d}^3 r' \, \mathrm{Tr}\left\{\mathbf{R}(\mathbf{r}_A, \mathbf{r}', i\xi) \cdot \mathbf{R}(\mathbf{r}', \mathbf{r}_A, i\xi)\right\} , \tag{6.18}$$

with the regular part of the free space propagator, Eq. (3.78)

$$\mathbf{R}(\mathbf{r}, \mathbf{r}', \omega) = \frac{\omega}{4\pi c}\left[f\left(\frac{c}{\omega\varrho}\right)\mathbf{I} - g\left(\frac{c}{\omega\varrho}\right)\frac{\boldsymbol{\varrho}\otimes\boldsymbol{\varrho}}{\varrho^2}\right] \mathrm{e}^{i\frac{\varrho\omega}{c}} , \tag{6.19}$$

with the difference vector $\boldsymbol{\varrho} = \mathbf{r} - \mathbf{r}'$.

We consider the thermal effects by evaluation of the MATSUBARA sum for the nonresonant part of the thermal CASIMIR–POLDER potential, see Sec. 3.4, with an inner temperature $T_{mol} = 600\,\mathrm{K}$ and an environmental temperature $T_{env} = 300\,\mathrm{K}$. Here, the assumption of the equality of the polarisabilities $\alpha_n \equiv \alpha$ is used, which enters the calculation via the simulated spectra, see Fig. 5.3 (a). This yields the CASIMIR–POLDER potential for point-like polarisable particles

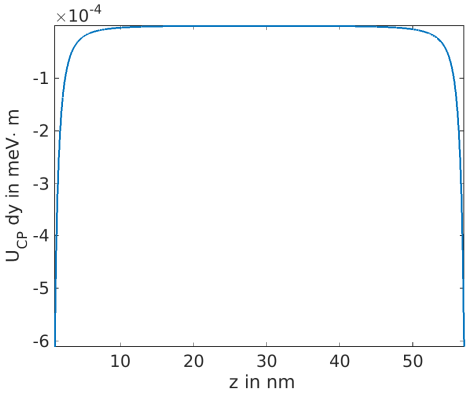

Figure 6.8: Calculated marginal potential for the carbon grating, G5.

$$U_{CP}(y,z) = \mu_0 k_B T {\sum_j}' \xi_j^2 \, \mathrm{Tr}\{\boldsymbol{\alpha}(i\xi_j)\mathbf{G}(\mathbf{r}_A, \mathbf{r}_A, i\xi_j)\} . \tag{6.20}$$

This potential has to be corrected with respect to the higher-orders of the BORN series expansion and with regard to the extension and rotation of the molecule, which yields the potential

$$\tilde{U}_{CP}(z) = \gamma\left[0.9 + 4.9\left(\frac{a}{z}\right)^2\right]\int U_{CP}(y,z)\,\mathrm{d}y . \tag{6.21}$$

The first factor, γ, denotes the higher order correction, Eq. (6.15), the second term is due to the extension and rotation of the molecule, Eq. (5.33), with $a = 17\,\mathrm{a_B} = 0.9\,\mathrm{nm}$ and an eccentricity $e = 4$, see Sec. 5.3.2.

Figures 6.8 and 6.9 illustrate the different marginal potentials inside the gratings for the carbon grating and the silicon nitride gratings, respectively. One observes that for the thicker gratings G2 and G4 the marginal potential is about an order of magnitude larger than for the thinner grating due to the different integration ranges. Multiplication with the inverse of the product of the PLANCK constant $\hbar$ and the velocities v, the phase shift becomes $\varphi(z) = -\tilde{U}_{CP}(z)/(\hbar v)$.

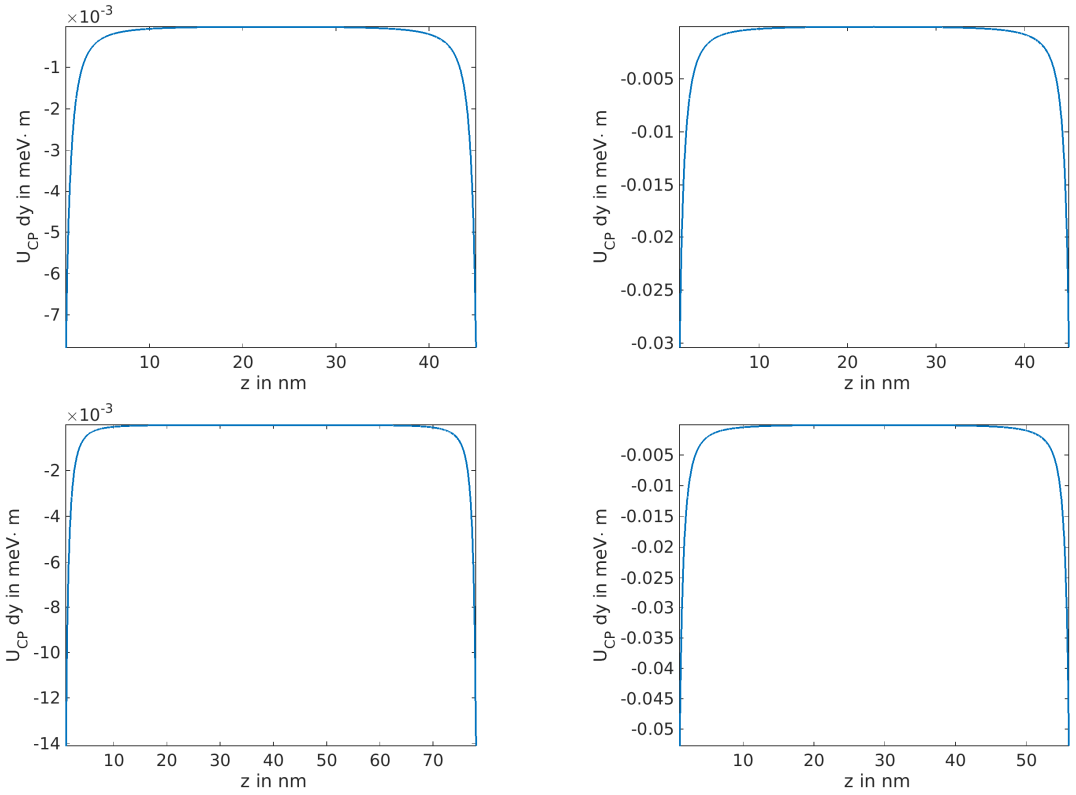

Figure 6.9: Calculated marginal potentials for the silcon nitride gratings: G1 (up, left), G2 (up, right), G3 (down, left), G4 (down,right).

6.3 Analysis of the interference patterns

Figure 6.10 shows a typical outcome of the interference experiment. The experiments were performed with a low flux of molecule, which means that only one molecule passes the apparatus at any one time. Hence, the interactions between the molecules do not have to be considered. Due to the automatic velocity-selection the interference fringes are shifted away from the zeroth interference order with decreasing velocity of the particles. Particles with a lower velocity are located in the lower region of the interference pattern.

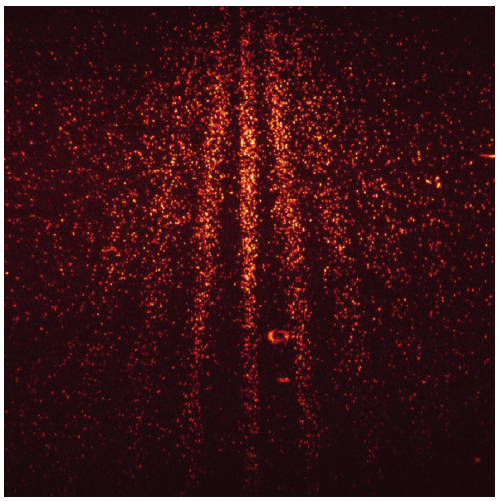

Figure 6.10: Typical interference pattern. Taken from Ref. [TJ12].

A horizontal cut through this interference pattern provides a velocity selection. Such selection defines a class of velocities $[v_i, v_{i+1}]$. Hence, a velocity distribution $\varrho(v)$, respectively depending on the k-vector $\varrho_v(k)$, has to be taken into account in the analysis.

The analysis of the interference patterns uses KIRCHHOFF's diffraction formula introduced in Sec. 2.3. The velocity distribution $\varrho_v(k)$ has to be included as well as the spatial extension of the source. These two effects appear in the method via an incoherent average over the velocity distribution $\varrho_v(k)$ and the single source point ($\mathbf{y}_0$). The interference pattern can be obtained from the intensity

$$I_v(z) = \int\limits_A \mathrm{d}\mathbf{y}_0 \int \mathrm{d}k\, \varrho_v(k) P(z; \mathbf{y}_0, k)\,, \tag{6.22}$$

where $P(z; \mathbf{y}_0, k)$ denotes the interference pattern calculated with the KIRCHHOFF's diffraction formula, Eq. (2.19), for a matter wave with the absolute value of the wave vector k and the source point $\mathbf{y}_0$. The analysis of the measurements was performed by a fit with respect to the strength of the CASIMIR–POLDER potential. A numerical routine adapted from S. NIMMRICHTER and T. JUFFMANN fits the measurements to the interference patterns depending on the calculated CASIMIR–POLDER potentials. The fitting parameter η scales the strength of the CASIMIR–POLDER potential. Figure 6.11 shows some examples of the result of the fitting routine. One observes that the theory in general matches the experimental data, but the fitting factor is still needed. The fitting parameter varies between 2 and 8, which describes a very large range and still has to be understood. This will be discussed in the next section.

6.4 Discussion of the experimental results

The calculated CASIMIR–POLDER potential with the fitting parameter η for the thicker grating matches the measurements very well. There, the value of η is relatively low ($\eta \approx 2$). In case of thinner gratings the deviation from the estimated CASIMIR–POLDER potential increases, which can be seen by the values of the fitting parameter, which go up to a factor of 8. This mismatch has to be considered in detail.

Let us repeat the steps for the calculation of the CASIMIR–POLDER potential. First, the complete electromagnetic properties of Phthalocyanine are needed. The quantum dynamics problem for the polarisability is solved in the limit of low internal temperature of the molecules. Its results are trustworthy. We have tested them against existing measurements in the optical range as well as the static polarisability.

We included the complete geometric shape of the grating by using the BORN series approach with trapezoidal grating bars. We corrected the approximation due to the self-interaction of the grating particles (local-field correction). We also considered higher orders of the BORN series expansion. In the next step, we considered the spatial extension and rotation effects of the molecule, which enter the electromagnetic scattering problem as smeared out source and final points.

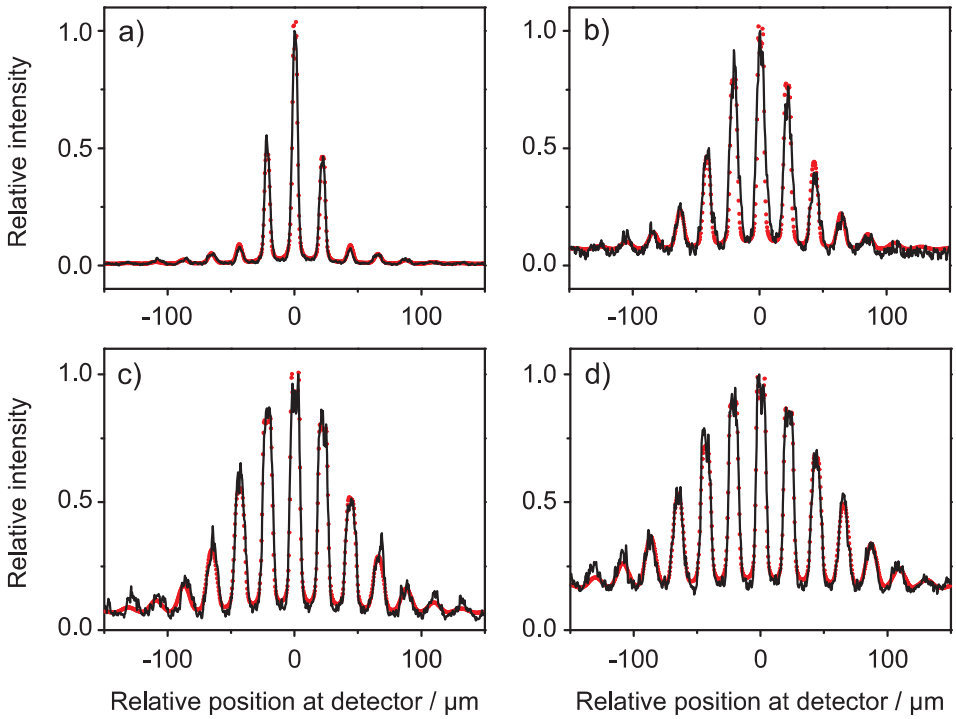

Figure 6.11: Fit of the Casimir–Polder potential and the experimental data for a velocity $v = 200$ m/s. Excellent agreement between theory and experiment can be obtained by the fit factor a) $\eta = 7.2$ for G1, b) $\eta = 2.0$ for G2, c) $\eta = 8.2$ for G3, and d) $\eta = 5.0$ for G4. Taken from [BF15].

The last point, which is still open, is the electromagnetic response of the grating bars. The material, silicon nitride, has an unknown stoichiometry (SiN_x). This leads to a wide range of possible optical responses, which can vary between isolating and weakly conducting. In this sense, the theory is incomplete due to a lack of information regarding the susceptibility of the material. Another aspect is the possibility of localised charges in the grating bar, which cause static electric fields.

The electric field, that is induced by a homogeneous surface charge, scales with the inverse third power of the distance, r^{-3} and acts on the static polarisability of the particle instantaneously. Hence, the interaction potential entering the phase shift, Eq. (6.2), scales with an $1/r^3$ over all distances. This means that the measurements have to be performed in the retarded regime to distinguish between the phases appearing from the Casimir–Polder potential and from the electrostatic interaction. In order to quantise this effect the charge distribution is needed. In the absence of such measurements, we will discuss the sources of the charges by analysing the production process of the gratings and determine qualitatively its influence.

We have to distinguish between two different production steps. In the first step, silicon nitride wafers have to be built. This is done by crystal growth. Such wafers made

of silicon nitride are mechanically unstable and consequently they have to be stabilised. In order to do so, an inert gas of nitrogen will be added to the environment during the growth process. Due to the accumulation of nitrogen to the crystal structure of the silicon nitride the unknown stoichiometry appears. Investigation of this production process has shown that, depending on the pressure of the inert gas, the conductivity of the wafer changes [YL08], meaning that the model for the susceptibility of silicon nitride does not represent its true properties. In addition, permanent charges can be placed inside the wafer [S95] during the growing process.

In the second step, one has to cut the grating openings into the wafer. We concentrate on two methods for cutting the grating structures. One is photolithography [S95, SG07], which is used for thick gratings. There, the grating structure is etched into the wafer. The other method is focused ion beam milling, where the grating openings were cut into the wafer by a fast ion beam. This method also produces permanent charges in the grating structure [YL08].

The thick grating, G4, was built by photolithography and the thinner gratings, G1-G3, by focused ion beams. One observes that the deviation of the calculated Casimir–Polder potential is less for the thick grating than for the thinner gratings. It is only a factor of two for the thick grating, which can be understood by the growth process of the wafer, which hence a deviation of the susceptibility. The higher deviations, which are observed for the thinner gratings, can be explained by the focused ion beam milling. This method localises charges inside grating bars, which causes a superposition of the Casimir–Polder force with an electric field induced by the charges. On finds an ion density of around $2.6 \cdot 10^{13}\,\mathrm{ions/cm^2}$ of Gallium ions (Ga^+) at a 100 nm thick silicon nitride grating [YL08], which decreases with time due to their neutralisation in air. Such measurements can be performed by a Kelvin probe force microscope. Measurements at the used gratings yields no results. One can expect that the number of ions decreases strongly, because the gratings were produced many years ago, and only the charges captured inside the grating bars still exist.

Consequently, the difference between theory and experiment could be explained on the basis of electric fields, which yield an additional force and hence an additional phase shift, which was not considered in the theory for the Casimir–Polder potential. In order to quantify the influence of the charges, additional investigations are needed. One possibility would be the measurement of the charge density, which is difficult for such small structures. Another option would be to use the interference experiments to estimate the additional phase shift. This method will be introduced in the following chapter.

chapter 7

Inverse scattering - spectroscopy of the matter wave

In the previous chapter we applied the formalism determining the Casimir–Polder interaction between a molecule and a dielectric grating to a real experiment. We included the Born series expansion to consider the geometric shape of the grating bars. Regarding the molecule we also used the correction according to its extension and rotation. The comparison with the corresponding experimental data showed a deviation between theory and experiment. The evaluated potentials are underestimated which might be caused by the applied assumptions - the first-oder Born series approach, the description as trapezoidal shaped cross sections area of the grating bars - or the data entering the Casimir–Polder potential for the polarisability of the molecule and the susceptibility of the dielectric grating. All aspects are potential sources of error. Consequently, one would have to gather additional information for example by infrared spectroscopy of Phthalocyanine or the measurement of the conductivity of the gratings. However, we know from scattering theory (chapter 2) that all information is impressed in the interference pattern. Hence, it is feasible to ask, if the interaction potential can be estimated from the interference patterns.

Let us recall Kirchhoff's diffraction formula, Eq. (2.19),

$$P\left(x',z'\right)=\frac{a_0^2k^2}{4\pi^2}\times\left|\int t\left(\tilde{x},\tilde{z}\right)\frac{\mathrm{e}^{ik\left(\sqrt{L_1^2+\left(\tilde{x}-x\right)^2+\left(\tilde{z}-z\right)^2}+\sqrt{L_2^2+\left(x'-\tilde{x}\right)^2+\left(z'-\tilde{z}\right)^2}\right)}}{\sqrt{L_1^2+\left(\tilde{x}-x\right)^2+\left(\tilde{z}-z\right)^2}\sqrt{L_2^2+\left(x'-\tilde{x}\right)^2+\left(z'-\tilde{z}\right)^2}}\mathrm{d}\tilde{x}\mathrm{d}\tilde{z}\right|^2,$$

for the estimation of the emerging interference pattern and the eikonal approximation,

Eq. (2.6),

$$\arg t(\mathbf{r}) = \varphi(\mathbf{r}) = -\frac{1}{\hbar}\int V\left(\mathbf{r}(t)\right)\mathrm{d}t \approx -\frac{1}{\hbar v_{\parallel}}\int V(\mathbf{r})\mathrm{d}\mathbf{r}_{\parallel}\,,$$

for calculating the spatial phase distribution of the complex transmission function. Here, we find two mathematical operations that result in a loss of information. One is to take the square of the absolute value of the wave in front of the screen that results the amplitude of the wave and yields the interference pattern. The other is the eikonal approximation, which is a line integral along the trajectories of the molecules. In order to estimate the interaction potential one has to invert both steps.

In the following, we analyse both steps and point out the corresponding inversion methods. First, we look at KIRCHHOFF's diffraction formula. By using the connection between matter-wave optics and ray optics one finds the HARTMANN–SHACK sensor which is an optical instrument and provides the phase distribution of a light wave. It results in a novel measuring method for matter waves to estimate the spatial distribution of its phase. Second, we consider the eikonal approximation which connects the interaction potential with the transmission function via the integration along straight lines. Thus, a rotation of the grating and the integration along the trajectories of the particles is a RADON transformation of the interaction potential.

Applying both methods, the full interaction potential can be determined by measuring the interference patterns. Finally, we consider the CASIMIR–POLDER potential and present a reconstruction method for the estimation of the polarisability of the particle based on the exact knowledge of the scattering object with respect to its dielectric function and geometrical shape.

7.1 Phase estimation of a neutral matter wave - the Hartmann–Shack sensor

The HARTMANN–SHACK sensor is an optical device for the phase estimation of the wave front of an electromagnetic wave. It is based on the geometric optics at a converging lens. In the following, we briefly discuss its principle and provide a possible implementation for matter waves.

Principle of a Hartmann–Shack sensor

A HARTMANN–SHACK sensor [JH1900, SP71] consists of a two-dimensional periodical arrangement of converging lenses with the spacing Δl. Figure 7.1 illustrates this arrangement in a one-dimensional cut through the sensor. The lenses are numbered by

the index i. Their positions are marked by x_i. The basic idea behind such sensor starts with a wave front with a phase profile $\varphi(x)$, which will be written as a TAYLOR series expansion of the wave front around the centre of a converging lens e.g. for the i-th lens

$$\varphi(x)|_{x=x_i} = \varphi(x_i) + \varphi'(x_i)(x - x_i) + \dots . \tag{7.1}$$

A wave front that is not strongly curved over the diameter of the lens can be approximated by a tilted plane wave. The screen of a HARTMANN–SHACK sensor is located in the focal plane of the lenses. By following the description of the geometric optics at a converging lens, a plane wave that is oriented parallel to the lens will create a point spot in the focal plane on the optical axis. If the plane wave is tilted by an angle θ, which is related to the gradient of the spatial phase distribution by $\sin\theta = \varphi'(x_i)$ [1], the resulting spot is shifted in the focal plane by Δx_i. One finds the relation

$$\varphi'(x_i) = \frac{k_0}{f}\Delta x_i\,, \tag{7.2}$$

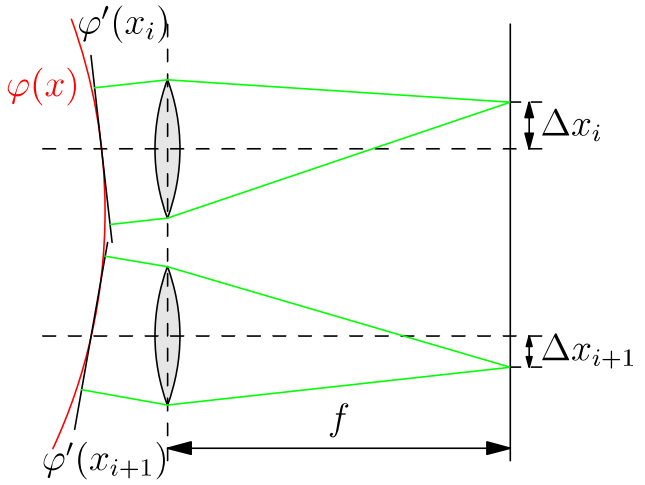

Figure 7.1: Sketch of the phase estimation method of a HARTMANN–SHACK sensor: The phase distribution of the wave $\varphi(x)$ (red) will be approximated by a TAYLOR series, resulting in oblique plane waves in front of the lenses (blue). They will be projected onto the screen (green) and result in spots in the focal plane. Their deviations from their optical axes are proportional to the slope of the plane wave. Taken from [FS17]

with the focal distance f and the absolute value of the wave vector k_0.

In general, the deviation from the optical axis occurs in both dimensions. Therefore, it will be described by a two-dimensional vector $\Delta\mathbf{X}(\mathbf{r})$. The phase of the wave front can be obtained from the line integral over all aberrations

$$\varphi(\mathbf{r}) = \frac{k_0}{f}\int \Delta\mathbf{X}(\mathbf{r}')\cdot \mathrm{d}\mathbf{r}'\,, \tag{7.3}$$

where k_0 denotes the wave number and $\Delta\mathbf{X}(\mathbf{r}')$ denotes the deviation of the spot from the optical axis (in the screen plane) at the position $\mathbf{r}'$. The first experimental realisation of this method was realised by R.V. SHACK and B.C. PLATT in the early 1970's [SP71].

In order to use this method for matter waves, one has to find a two-dimensional periodical arrangement of converging lenses for matter waves. The treatment of the wave optics of a matter wave is similar to that of electromagnetic waves using FOURIER

[1] The sine arises due the definition of the angle θ, which is the deviation from the optical axis.

optics. In FOURIER optics, the interaction of an incoming wave ψ_{in} with an optical instrument is related to the outgoing wave ψ_{out} by a convolution with an integral kernel K [JWG68]

$$\psi_{out} = K * \psi_{in} = \int \mathrm{d}^3 r' K(\mathbf{r} - \mathbf{r}')\psi_{in}(\mathbf{r}') \,. \tag{7.4}$$

For a converging lens, this kernel is given by [JWG68]

$$K_{lens} = \mathrm{e}^{-ik\frac{x^2+y^2}{f}} \,, \tag{7.5}$$

with the absolute value of the wave vector k and the focal distance f. Analogously, for matter waves it follows from Eq. (2.6) that the phase of the integral kernel is given as the integral along the trajectories of the particles through the interaction potential

$$\arg K = -\frac{1}{\hbar} \int H_{int}[\mathbf{r}(t)] \, \mathrm{d}t \,. \tag{7.6}$$

Therefore, a spatially quadratic interaction HAMILTONian is needed for the description of a converging lens.

The Hartmann–Shack sensor for matter waves

We are considering a neutral, nonpolar, but polarisable particle. Let there be a standing laser wave with the wavelength λ. In this case, the interaction HAMILTONian can be written as the dipole electric field interaction $H_{int} = -\mathbf{d} \cdot \mathbf{E}$ and the dipole moment is induced by the electric field itself, which yields $H_{int} = -\frac{1}{2}\alpha \left|\mathbf{E}\right|^2$, where α denotes the polarisability of the particle at the laser field frequency. The electric field of a linear polarised GAUSSian beam, propagating along the x-direction, can be described by

$$|\mathbf{E}(\mathbf{r})| = A \, \mathrm{e}^{-\frac{\varrho^2}{W_0^2}} \cos(kx) \,, \qquad \varrho^2 = y^2 + z^2 \tag{7.7}$$

with the amplitude A, the wave number $k = 2\pi/\lambda$, the beam radius $W_0^2 = \lambda x_0/\pi$ and the beam waist x_0.

One-dimensional beam array

Figure 7.2 shows the principal arrangement of a one-dimensional beam array. The retroreflected GAUSSian beams form a two-dimensional array of converging lenses. In general, however, the resulting curvatures of the created lenses will be different along the x-and y-directions. The curvature in x-direction is given by the wavelength of the laser light, whereas in the y-direction it is related to the beam waist which itself is given in terms of the wavelength by $x_0 = \lambda/(4\pi)$. This means that it is impossible to realise equal curvatures, i.e. rotationally symmetric lenses. In this case, one has to work with two distinct focal planes which in turn means that two separate measurements have to be performed.

The individual lenses imprint identical phase shifts $\varphi(x, y)$ on the matter wave. We define the periodicity of the lenses as $d = \lambda/(2\pi)$. In this case, the accumulated phase in each beam is [KH09]

$$\varphi(x, y) = \varphi_0 \cos^2\left(\frac{x}{d}\right) \mathrm{e}^{-\frac{y^2}{W_0^2}}, \quad (7.8)$$

with

$$\varphi_0 = 8\sqrt{2\pi}\frac{\alpha}{\hbar c}\frac{P}{W_0 v}, \quad (7.9)$$

where α denotes the polarisability of the particle at the frequency of laser field, P the power of the laser and v denotes the velocity of the particle. The TAYLOR series expansion of the cosine and the exponential function up to the second order yields the quadratic form of the phase

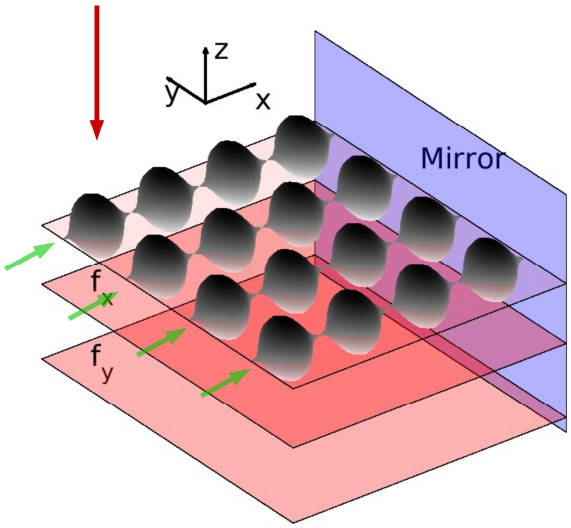

Figure 7.2: Sketch of the setup for the linear arrangement. Four lasers create standing waves by the reflection at the mirror. Due to the different periodicities curvatures in the x- and y-direction, one finds the two focal planes labelled with f_x and f_y. The particles pass the laser field along the negative z-direction (red arrow). Taken from [FS17]

$$\varphi(x, y) \approx \varphi_0 \left(1 - \left(\frac{x}{d}\right)^2 - \frac{y^2}{W_0^2}\right) = \varphi_0 - \varphi_0\frac{x^2}{d^2} - \varphi_0\frac{y^2}{W_0^2}, \quad (7.10)$$

where the first term yields a constant phase shift of the matter wave, the second term describes the converging lens in x-direction with the focal distance [FS17]

$$f_x = \frac{d^2 k_{\mathrm{dB}}}{\varphi_0} = \frac{d^2 W_0 k_{\mathrm{dB}} \hbar c v}{8\sqrt{2\pi}\alpha P}, \quad (7.11)$$

and the third term describes the converging lens in y-direction with a different focal distance [FS17]

$$f_y = \frac{W_0^2 k_{\mathrm{dB}}}{\varphi_0} = \frac{W_0^3 k_{\mathrm{dB}} \hbar c v}{8\sqrt{2\pi}\alpha P}. \quad (7.12)$$

For a purely one-dimensional arrangement, the incoming matter wave should align along the optical axis, which is experimentally hard to realise. Therefore, the deviation in the y-direction is needed as well. By the knowledge of the behaviour in two orthogonal directions, this system can be expanded into a two-dimensional sensor by a periodic arrangement of multiple lasers. In this context, one can define two-dimensional sensors with two focal planes, one for each direction.

Figure 7.2 shows the principal arrangement of the setup. Linearly arranged lasers create a two-dimensional array of converging lenses by the reflection at a mirror, which yields an array of standing laser fields parallel to each other. Therefore, the size of the

lens is defined by the periodicity of the lasers (in y-direction) and by the wavelengths of the laser in x-direction. The particles pass through the laser beams in z-direction. Due to the different extensions of a lens along x- and y-directions, two focal planes have to be defined.

Subsequent measurements with the screen at the focal distances f_x and f_y produces measurement patterns that are smeared out in the y- and x-directions, respectively. Each lens covers an area of $d \times W_0$. This means that the phase cannot be determined to a better resolution than this. In order to accomplish a higher resolution, lenses would have to be created with a size smaller than the beam waist which requires a modified concept which we describe next.

Two-dimensional beam arrays

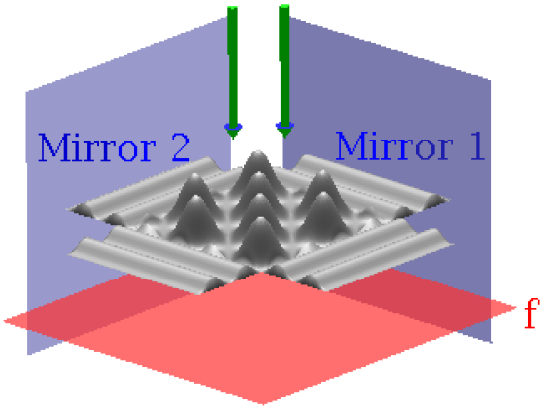

Figure 7.3: Sketch of the setup for a two-dimensional beam array. The superposition of two crossed standing waves creates the two-dimensional arrangement of converging lenses (grey) with a single focal plane f (red). The molecules move along the green arrow through such apparatus. Taken from [FS17]

As was shown in the previous section, in a one-dimensional beam array the beam waist limits the resolution. Instead, we propose to use a line source, i.e. an extended beam in one spatial direction, which can be created by a one-dimensional beam expander, which can experimentally be realised by cylindrical lenses. Theoretically, such an extended (linearly polarised) beam can be obtained by applying HUYGENS' principle [BW99] and by superposing the electric field, Eq. (7.7), along the rotation axis of the cylinder, which yields the electric field

$$|\mathbf{E}(\mathbf{r})| = A\,\mathrm{e}^{-\frac{x^2}{W_0^2}} \cos(kz)\,. \tag{7.13}$$

To produce a two-dimensional lens array, two line sources, propagating along orthogonal directions, have to be used (see Fig. 7.3). In other words, this creates a two-dimensional optical lattice. The phase that will be accumulated by passing through this device can be written as

$$\varphi(x,y) = \varphi_0 \cos^2\left(\frac{x}{d}\right) \cos^2\left(\frac{y}{d}\right)\,. \tag{7.14}$$

Its TAYLOR series expansion again yields a constant phase shift plus the converging lens with a single focal distance [FS17]

$$f = \frac{d^2 W_0 k_{\mathrm{dB}} \hbar c v}{8\sqrt{2\pi}\alpha P}\,. \tag{7.15}$$

Figure 7.3 illustrates the experimental setup. Two laser beams have to be extended along the x- and the y-direction. Each of them creates a standing wave by the reflection at a mirror (blue). Both fields will be arranged orthogonally, which creates the two-dimensional landscape and can be identified as a two-dimensional array of lenses for matter waves. In this setup, the periodicities of the lenses become equal in both directions, thus only one focal plane appears, which simplifies the measurement.

A typical laser has a wavelength of several hundred nanometers, e.g. 543 nm for the green helium-neon laser. This means for the HARTMANN–SCHACK sensor for matter waves, that a lens has an extension of roughly 250 nm. This has two consequences. One is, that the spot has to be measured on length scales smaller than this diameter, which is possible by using special filter techniques for the analysis [CB16]. The other consequence is, that the phase profile will be averaged over an area of 250 nm × 250 nm, which demands that the curvature of the phase profile should be negligibly small over this area. The resolution can be increased by spatial shifts of the sensor, so that the average will be made over different areas.

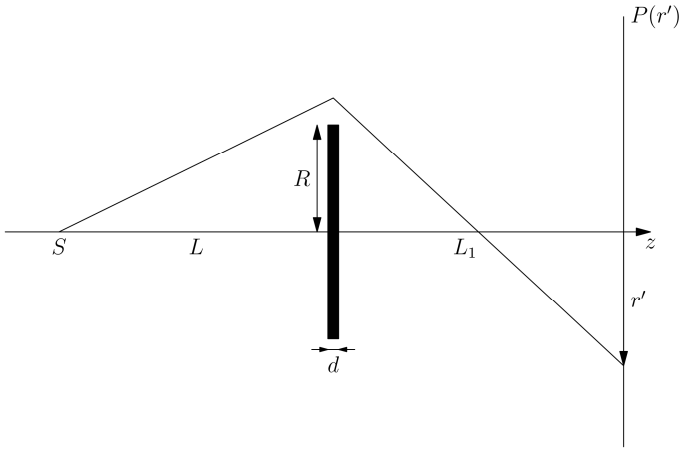

Figure 7.4: Sketch of the diffraction at a spherical disc. Point source S, intensity profile at the screen $P(r')$, distance between source and disc L and between disc and screen L_1 and the disc with radius R and thickness d. Taken from [FS17]

Example: Diffraction at a disc

Here, we illustrate the expected measurements of such HARTMANN–SHACK sensor for matter waves by considering a diffraction experiment at a disc. Figure 7.4 shows the typical experimental arrangement for such an experiment at a spherical disc with radius R and thickness d. We assume a near field diffraction (FRESNEL approximation) analogously to the POISSON spot experiments reported in Refs. [TR11, JH16]. Then, KIRCHHOFF's diffraction integral in cylindrical coordinates for the intensity profile reads [BW99]

$$P(r') = \left| a_0 k_0 \frac{\mathrm{e}^{ik_0\left(L+L_1+r'^2/(2L)\right)}}{LL_1} \int_R^\infty \mathrm{e}^{i\varphi(r)} \mathrm{e}^{ik_0 r^2 \frac{L+L_1}{2LL_1}} J_0\left(\frac{k_0 r r'}{L}\right) r\mathrm{d}r \right|^2 , \tag{7.16}$$

with the cylindrical BESSEL function $J_0(x)$, the wave's amplitude a_0, its wave vector k_0 and a phase $\varphi(r)$ that depends on the interaction between the particles and disc. For matter waves and a dielectric body this phase is proportional to the CASIMIR–POLDER potential integrated along the trajectories of the particles. Here, different functional dependencies can appear due to the involved materials and geometrical shape of the scatterer. For example, a disc of thickness d and a non-retarded CASIMIR–POLDER interaction would yield a phase

$$\varphi(r) \propto \frac{C_3 d}{r^3}\,, \tag{7.17}$$

whereas a sphere would give [JH16]

$$\varphi(r) \propto C_{52} r^{-5/2}\,, \tag{7.18}$$

where the coefficient C_{52} depends on the radius of the sphere. The distance between source and disc is L and between disc and screen is L_1.

For the simulation we assume the following parameters: disc radius $R + 25\,\mu$m, $L = 1.5\,$m, $L_1 = 1\,$m, and a DE BROGLIE wavelength $\lambda = 3\,$pm. These parameters are based on the experiment reported in Ref. [TR11], and satisfy the near field criterion $R^2/(L\lambda) \gg 1$. For the phase profile, we choose a simplified model

$$\varphi(r) = -\frac{C}{r - R}\,, \tag{7.19}$$

with $C = 1\mu$m, which is valid for charged particles.

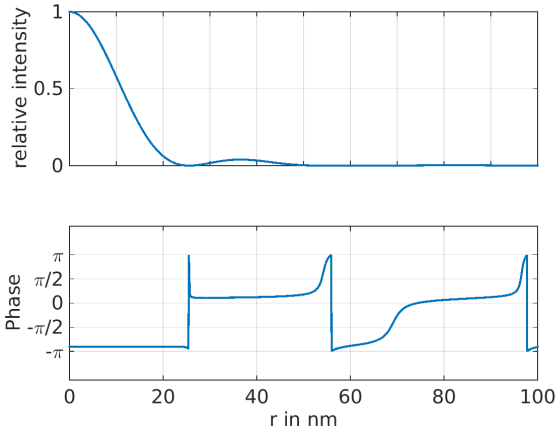

Figure 7.5: Expected measurements for the diffraction at a disc, amplitude (top) showing the POISSON spot and the corresponding phase distribution (bottom) resulting from the HARTMANN–SHACK sensor for matter waves. Taken from Ref. [FS17].

Figure 7.5 shows the amplitude and phase of the diffracted matter wave. The amplitude $\sqrt{P(r')}$ can be obtained from the intensity of the diffraction pattern, whereas the phase $\phi(r')$ of the matter wave can be retrieved by the application of the HARTMANN–SHACK measurement presented above.

The complex wave expression that appears under the absolute value in KIRCHHOFF's diffraction formula, Eq. (7.16), is in general given by

$$\sqrt{P(r')}\mathrm{e}^{i\varphi(r')} = a_0 k_0 \frac{\mathrm{e}^{ik_0\left(L+L_1+r'^2/(2L)\right)}}{LL_1} \int_0^\infty t(r)\mathrm{e}^{ik_0 r^2 \frac{L+L_1}{2LL_1}} J_0\left(\frac{k_0 r r'}{L}\right) r\mathrm{d}r\,, \tag{7.20}$$

where $t(r)$ denotes the complex transmission function of the scattering object (here the disc). In Fig. 7.5, we have assumed that $t(r) = \Theta(r - R)\mathrm{e}^{i\varphi(r)}$. Note that for the numerical example we have also chosen a particular phase profile $\varphi(r)$. However, it could be of interest to use the information supplied by the HARTMANN–SHACK measurement to reconstruct an unknown phase profile or, more generally, an unknown complex transmission function. By this, one obtains information about the interaction of the matter-wave constituents (i.e. atoms or molecules, now viewed as particles) with the scatterer and hence the interaction potential H_{int}.

In this specific example, the diffracted wave (7.20) is related by a HANKEL transform to the transmission function $t(r)$. This means that the transmission function can be obtained by suitable inversion algorithms for the HANKEL transform that are known from the literature [JF99, DWZ02, CC07]. Beyond this simple example, neither has the scatterer to be rotationally symmetric nor does the FRESNEL approximation have to be sufficient.

The interaction between the particles and a macroscopic scatterer is, at least for globally neutral and polarisable particles, the CASIMIR–POLDER potential [CP1948, SYB12-I, SB08] which results from ground-state fluctuations of the quantised electromagnetic field. An immediate application of a HARTMANN–SHACK measurement would therefore be to reconstruct the CASIMIR–POLDER interaction itself. Combined with additional knowledge about the geometric and optical properties of the macroscopic scatterer, it will be possible to also reconstruct the polarisability of the microscopic particles.

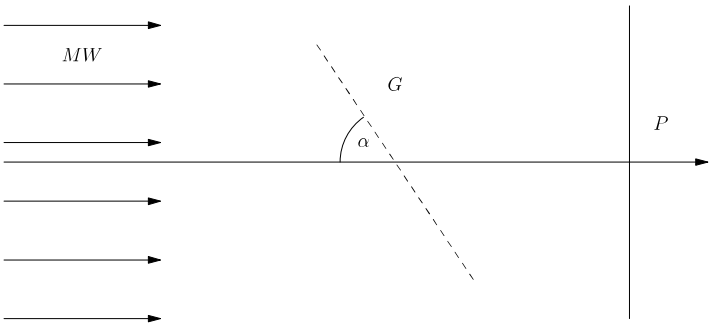

Figure 7.6: Sketch of the experimental setup for the tomographic reconstruction. The grating G will be rotated by an angle α with respect the the optical axis. The matter wave MW passes the grating on the straight lines parallel to the optical axis, interferes afterwards and is projected onto the screen P.

7.2 Reconstruction of a weak interaction potential

In a diffraction experiment, where a matter wave interacts with a scattering object via an interaction potential $U(\mathbf{r})$, this interaction can affect the matter wave in two different ways. Both describe a momentum transfer, which can act in a direction transverse to the propagation that results in a spatial shift of the particles. On the other

hand, it can affect a momentum transfer in the longitudinal direction, i.e. along the direction of propagation, which only leads to a phase shift of the matter wave. For a sufficiently weak interaction, such as the CASIMIR–POLDER force, the transverse momentum transfer can be neglected, and it is enough to consider the phase shift.

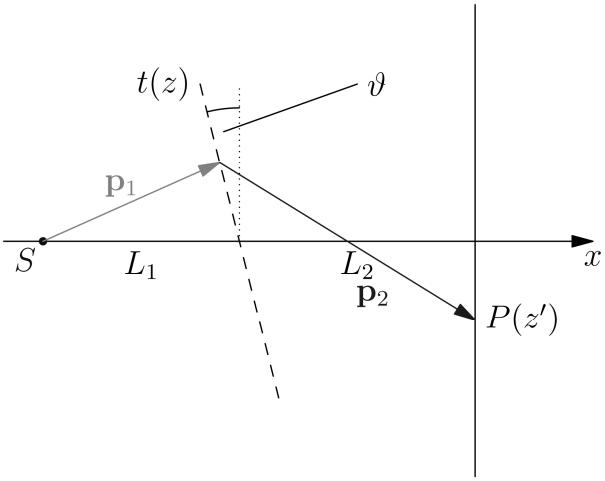

Figure 7.7: Sketch of the experimental setup. The matter wave is generated at the point S and propagates through the rotated scattering object (rotation angle ϑ with respect to the transversal plane of the wave). The emerging interference pattern at the screen is labelled with $P(z')$. The vectors $\mathbf{p}_1$ and $\mathbf{p}_2$ illustrate the wave propagation from the source to the scatterer and from the scatterer to the screen, respectively. Taken from Ref. [FS17].

through the scattering object, see Sec. 2.1.

Due to the symmetry of the potential along the longitudinal direction, the wave vector of the incoming wave is identical to that of the outgoing wave. Intermittently, however, the particles are accelerated during the approach of the scattering object and decelerated upon their departure [TJ10]. This implies that the integration over time along the particle's trajectories can be replaced by an integration along these paths

$$\begin{aligned}\varphi(x) &= -\frac{1}{\hbar}\int_{t_0}^{t_e} H_{int}[x(t), y(t)]\,\mathrm{d}t \\ &= -\frac{1}{\hbar v_\parallel}\int_{y_0}^{y_e} H_{int}(x, y)\,\mathrm{d}y\,,\end{aligned} \tag{7.21}$$

where we assumed that the particles move along straight lines $y = v_\parallel t$

7.2.1 Tomographic reconstruction of a weak interaction potential

A consequence of the eikonal approximation is that the scattering object enters the description of the scattering process via the projection of the interaction potential onto the transversal plane. Hence, a rotation of the scatterer is equivalent to different marginals of the interaction potential. This procedure is well established as the basis of the reconstruction algorithm using RADON transformation. The principle is sketched in Fig. 7.7 showing a wave generated at the source S propagating through the scattering object with transmission function $t(z)$ that is rotated by an angle ϑ with respect to transverse plane. The interference pattern is observed at $P(z')$.

7.2.2 The Radon transformation and its inversion

As mentioned before, a consequence of the eikonal approximation is that the longitudinal extension of the scatterer enters the KIRCHHOFF integral only in the projection onto the transverse plane. In the following, we introduce the RADON transform and a possible inversion method.

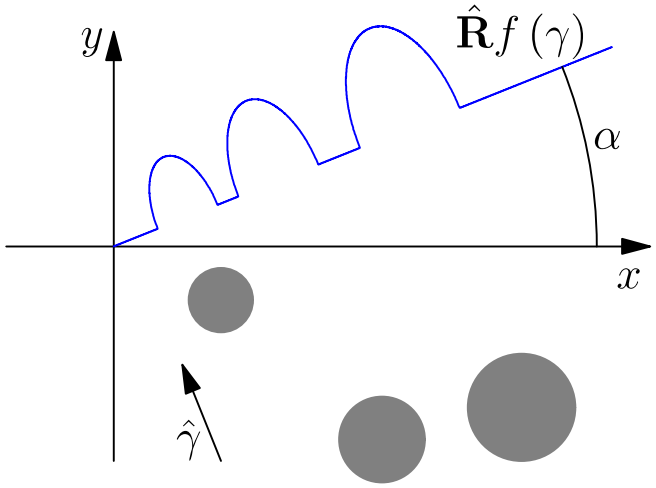

Figure 7.8: An example for the RADON transformation. The scalar field consisting of three cylinders of the height 1 (grey circles), $f(x,y) = \sum_{i=1}^{3} \Theta\left(r_i - \sqrt{(x-x_i)^2 + (y-y_i)^2}\right)$, is projected onto the line perpendicular to the direction $\hat{\gamma}$. The blue line shows its result for one angle α.

The Radon transformation

A RADON transform $\hat{R}$ is an integral transformation and maps a scalar field, $f(x,y)$, for Cartesian coordinates to polar coordinates via an integration along parallel straight lines, which creates an angle regarding the Cartesian coordinate system [JR17]. Figure 7.8 illustrates the different systems. The new coordinates are given by the rotation angle α and the straight line perpendicular to the integration direction. In the case of a two-dimensional scalar field $f(x,y)$, the RADON transform

$$\hat{R}f(\gamma) = \int_{\gamma} f(x,y)\,\mathrm{d}s \tag{7.22}$$

along the straight line $\gamma(t) = (x(t), y(t)) = (r\cos\alpha + t\sin\alpha, r\sin\alpha - t\cos\alpha)$ can be defined as

$$\hat{R}f(r,\alpha) = \int_{-\infty}^{\infty} f(r\cos\alpha + t\sin\alpha, r\sin\alpha - t\cos\alpha)\,\mathrm{d}t\,. \tag{7.23}$$

Figure 7.8 shows a simple example of the RADON transform. Here, three cylinders of a unit height define the scalar field $f(x,y)$. The blue curve denotes a RADON transform in the direction of $\hat{\gamma}$, the unit vector of the integral trajectories, which is rotated clockwise by the angle α.

The inverse Radon transformation

In the literature, a large number of algorithms exist for the estimation of the inverse RADON transformation. For details see the excellent textbooks [HHB84, RNB96, KS88].

Here, we briefly introduce the basic idea behind the back projection method [SB02], where all scattering profiles $\hat{\mathbf{R}}f\,(r,\alpha)$ depending on the angle α have to be known for the reconstruction of the integral kernel $f\,(x,y)$.
First, we have to define the RADON projection operator [SB02]

$$\lambda_\phi(p) = \hat{\mathbf{R}}_\phi\left[f(\mathbf{r})\right](p) = \int_A f(\mathbf{r})\delta(p-\mathbf{r}\cdot\mathbf{n}_\phi)\,\mathrm{d}^2r \tag{7.24}$$

of the two-dimensional function $f(\mathbf{r})$ $[\mathbf{r}=(x,y)]$ and the unit vector in ϕ-direction $\mathbf{n}_\phi = (\cos\phi, \sin\phi)$, which is a surface integral over the occupied area A. The projected straight line is given in HESSE normal form $p = \mathbf{r}\cdot\mathbf{n}_\phi$. In the next step, the marginal distribution for all angles ϕ will be rewritten as

$$f_\phi(\mathbf{r}) = \lambda_\phi(\mathbf{r}\cdot\mathbf{n}_\phi)\,, \tag{7.25}$$

which is called back projection of a single angle. The integration over all angles ϕ yields the complete back-projected distribution

$$f_b(\mathbf{r}) = \hat{\mathbf{B}}\left[\lambda_\phi(\mathbf{r}\cdot\mathbf{n}_\phi)\right] = \int_0^\pi \lambda_\phi(\mathbf{r}\cdot\mathbf{n}_\phi)\,\mathrm{d}\phi\,. \tag{7.26}$$

An analysis of the composition of the RADON transform and the back projection yields the relation

$$\hat{\mathbf{B}}\left\{\hat{\mathbf{R}}\left[f(\mathbf{r})\right]\right\} = \int_A f(\mathbf{r}')\frac{1}{|\mathbf{r}-\mathbf{r}'|}\,\mathrm{d}^2r'\,, \tag{7.27}$$

which is a convolution integral with the kernel $|\mathbf{r}|^{-1}$, and is equivalent to the electrodynamics picture of an electric potential evoked by the area charge density $f(\mathbf{r})$. The integral kernel corresponds to the point spread function of the composition $\hat{\mathbf{B}}\hat{\mathbf{R}}$. The deconvolution of this equation can be done by the use of the convolution theorem by multiplying with the integral kernel and applying the inverse FOURIER transform, which yields the inverse RADON transform

$$\hat{\mathbf{R}}^{-1} = \mathfrak{F}^{-1}\,|\boldsymbol{\varrho}|\,\mathfrak{F}\hat{\mathbf{B}}\,, \tag{7.28}$$

which has to be understood as a composition of these elementary operations. This algorithm for the inverse RADON transform is only a toy example and not convenient for a numerical implementation, because its numerical effort is enormously high. Other methods exist, which decrease the numerical cost, but this example is easy to understand. Nevertheless, with such a method the reconstruction of the interaction potential from the marginal phases is possible, so that we can continue with the analysis of the CASIMIR–POLDER potential to estimate the polarisability of the particle.

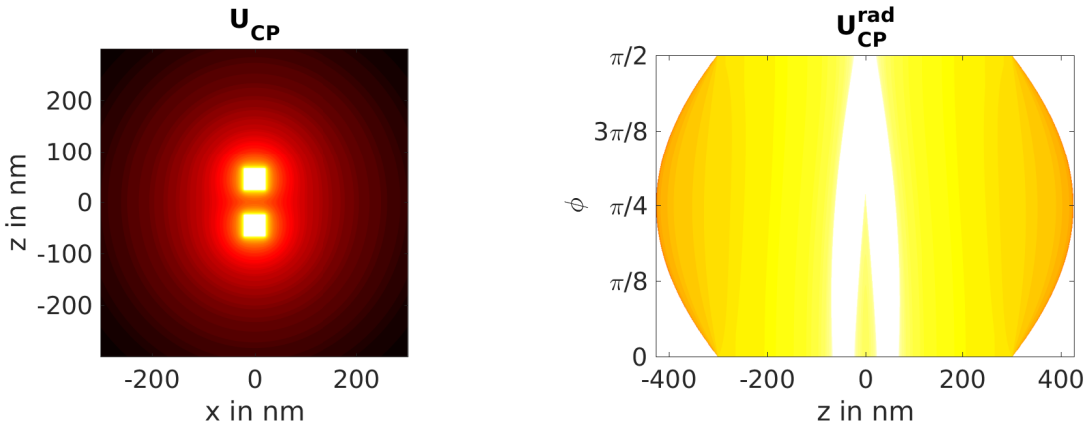

Figure 7.9: Potential landscape of the two grating bars (left) and its corresponding RADON transformation (right).

Example: Diffraction at two square bars

We will now illustrate the application of the inverse RADON transformation by considering a matter-wave interference experiment in which particles were diffracted at two grating bars with a square cross section. The bars have an edge length of 20 nm and are separated by a distance of 50 nm. We assume a weak susceptibility of the gratings, so that we can apply the BORN series approach to estimate the potential landscape. We choose an interaction strength with a C_3-coefficient of $C_3 = 150\,\mathrm{neV(nm)}^3$. Figure 7.9 illustrates the two-dimensional potential landscape of the CASIMIR–POLDER potential (left) and its corresponding RADON transformation (right). According to the geometry one observes that the two grating bars create effectively one bar for rotation angles around $\pi/4$.

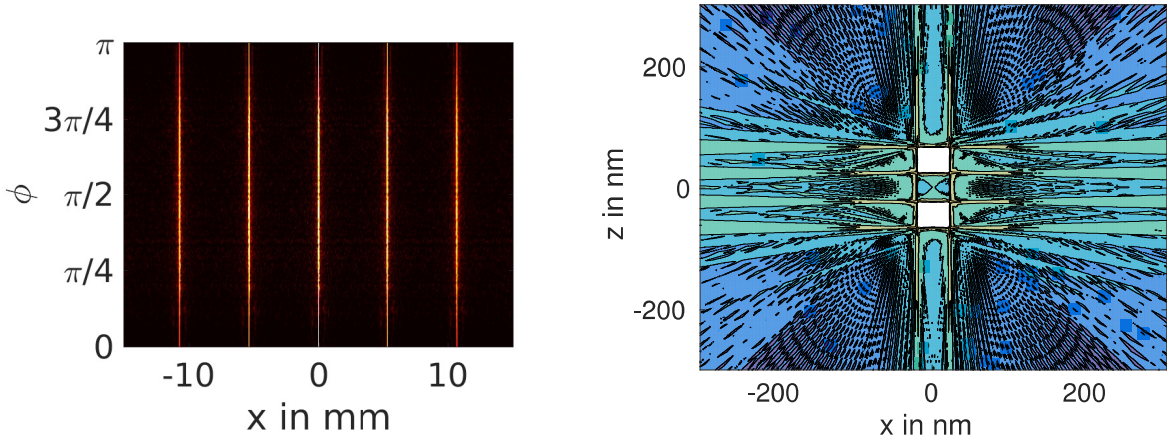

Figure 7.10: Sketch of the interference patterns depending on the rotation angle ϕ (left) and the inverse RADON transformation of the reconstructed interaction potential (right).

For the simulation we chose Rubidium atoms with a mass of $86u$ and a velocity of $900\,\mathrm{m\,s^{-1}}$, equivalent to a DE BROGLIE wavelength of $\lambda_{\mathrm{dB}} = 5.3\,\mathrm{pm}$. These values

coincide with those in the experiment in Ref. [WH10].

Figure 7.10 illustrates the emerging interference pattern by the diffraction at both bars depending on the rotation angle ϕ and the reconstructed potential landscape using an inversion method implemented in MATLAB. It can be seen that the singularities along the shadows of the grating bars present problems for the reconstruction towards the faces of the bars, whereas the cross section of the bars can be found very accurately. Using this method, the correct order of magnitude of the interaction potential can be reconstructed and the geometric shape of the scatterer. Further inverstigations are needed to improve the quality of the reconstruction.

7.3 Decomposition of the Casimir–Polder potential

As an application of the reconstruction procedure, let us consider the diffraction of neutral and polarisable particles at a dielectric body. In this case, we are considering the Casimir–Polder potential at low temperatures for an isotropic particle

$$U_{CP}(\mathbf{r}_A) = \frac{\hbar\mu_0}{2\pi}\int_0^\infty \mathrm{d}\xi\, \xi^2\alpha(i\xi)\,\mathrm{Tr}\left\{\mathbf{G}(\mathbf{r}_A,\mathbf{r}_A,i\xi)\right\}\,, \tag{7.29}$$

which, regarding the scalar polarisability α, is a Fredholm equation of the first kind. Inversion of this equation to obtain the polarisability is possible via a discretisation of the integral. For this purpose, we define an equidistant grid in the frequency domain, ξ_j , with a spacing $\Delta\xi$. Let us assume that the estimated Casimir–Polder potential is based on measurements using the Hartmann–Shack method, which means that it is known on a discrete set of spatial points $\mathbf{r}_i$,

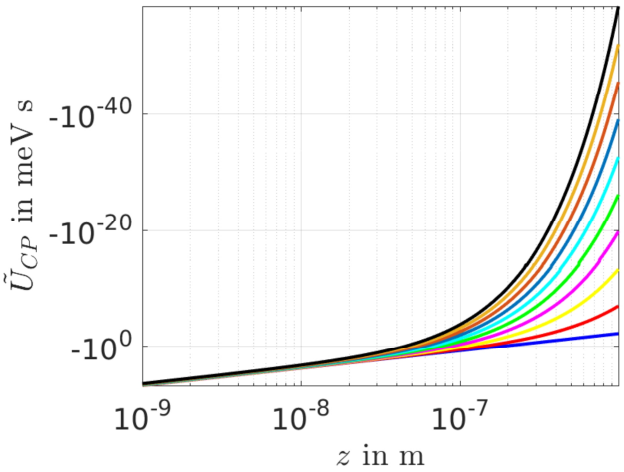

Figure 7.11: Plot of the frequency dependent Casimir–Polder potential $\tilde{U}_{CP}(z,\xi)$, Eq. (7.33), for Phthalocyanine in front of an infinite half-space for different equidistantly distributed imaginary frequencies $\xi = 1.52\times 10^{13}, 4.65\times 10^{15}, 6.93\times 10^{15}, \ldots, 2.06\times 10^{16}\,\mathrm{rad\,s^{-1}}$ (blue to yellow). Taken from [FS17].

$$U_{CP}(\mathbf{r}_i) \approx \frac{\hbar\mu_0\Delta\xi}{16\pi^2}\sum_{j=1}^{N}\alpha(i\xi_j)\xi_j^2\,\mathrm{Tr}\mathbf{G}(\mathbf{r}_i,\mathbf{r}_i,i\xi_j)\,. \tag{7.30}$$

For numerical reasons, we introduce a dimensionless function $\chi(\xi)$ by normalising the

frequency-dependent polarisability to its static value

$$\alpha(i\xi) = \alpha(0)\chi(\xi)\,, \tag{7.31}$$

so that the CASIMIR–POLDER potential becomes

$$U_{CP}(\mathbf{r}) = \int_0^\infty \mathrm{d}\xi \chi(\xi)\tilde{U}_{CP}(\mathbf{r},\xi)\,. \tag{7.32}$$

Here, we introduced a frequency-dependent potential function

$$\tilde{U}_{CP}(\mathbf{r},\xi) = \frac{\hbar\mu_0}{16\pi^2}\alpha_0\xi^2 \mathrm{Tr}\mathbf{G}(\mathbf{r},\mathbf{r},i\xi)\,, \tag{7.33}$$

which is illustrated in Fig. 7.11. It can be clearly seen that in the nonretarded limit, spatial and frequency dependencies decouple. As we have argued previously, the resulting system of equations cannot be inverted in the nonretarded limit. Hence, the sampling has to be extended well into the retarded regime.

Using the discretisation of the CASIMIR–POLDER potential, Eq. (7.30), together with Eq. (7.33), the system of linear equations for the estimation of the dimensionless function $\chi(\xi_j)$ can be written as [FS17]

$$U_{CP}(\mathbf{r}_i) = \sum_j \tilde{U}_{CP}(\mathbf{r}_i,\xi_j)\Delta\xi\chi(\xi_j)\,. \tag{7.34}$$

As the polarisability $\alpha(i\xi)$ is a monotonously decreasing function of ξ, one has at least to ensure the condition $\chi(\xi_i) \in [0,1]$ for solving the system of equations. The solution of the system of equations is then performed using a least-squares fit. The result is shown in Fig. 7.12. One observes that the general behaviour of the dimensionless function $\chi(\xi)$ is well reproduced. A better agreement can be obtained by choosing a larger number of sample points, or by a more appropriate (e.g. non-equidistant) discretisation of the frequency axis.

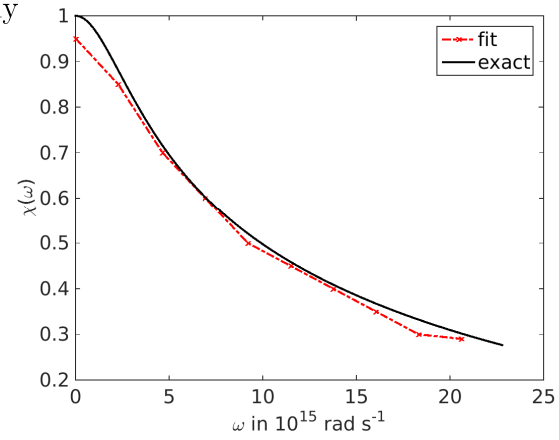

Figure 7.12: Result of the fit routine for the estimation of the characteristic function of Phthalocyanine in front of a silicon nitride wall for 10 fitting points. Taken from [FS17].

As a result, the polarisability of the particle can be estimated from a measurement of the CASIMIR–POLDER potential, given the knowledge of the geometric shape and the optical response of the scatterer. Although we have only shown the reconstruction for a

simple idealised experimental arrangement, it is clear that more complicated scattering geometries can be treated on the same footing. In each case, a detailed investigation of the numerical errors would be necessary which we have omitted here for simplicity.

7.4 Simplification by symmetry

At the begin of this chapter, we formulated the question whether the information content of the interference patterns is enough for an estimation of the properties of the involved participants. In general, this has to be affirmed. We performed the reconstruction of the polarisability of the particles, we repeated the essential steps for calculating an interference pattern with matter waves and presented methods for their back estimation. Following such method, the estimation of the properties of the scatterer - its optical response or its geometric shape - can be performed analogously.

First, we concentrated on a single interference pattern and showed the reconstruction via the Hartmann–Shack sensor for matter waves. Here, we proposed a new experimental arrangement for the estimation of the phase profile of the matter wave. It is built with a standing laser field which has to be located in a certain distance in front of the screen. Following this measuring principle one has to perform two measurements - one with and one without the laser field - to estimate the complete information about the wave. Due to the far-field assumption, the distance between the optical plane and the detector is negligible. In order to reconstruct the interaction potential, one has to rescale the amplitude and the phase due to the free propagation from the scattering object to the screen. Following the Huygens–Fresnel principle, the complex transmission function with the marginal Casimir–Polder potential in the argument can be obtained. The next step is the estimation of the Casimir–Polder potential from the marginal phase distributions. We showed that this marginal distribution is equivalent to a Radon transformation of the interaction potential. In order to use the established inversion methods for the Radon transform, a large number of rotation angles are needed, which means that the experiments have to be repeated very often with a rotated scattering object.

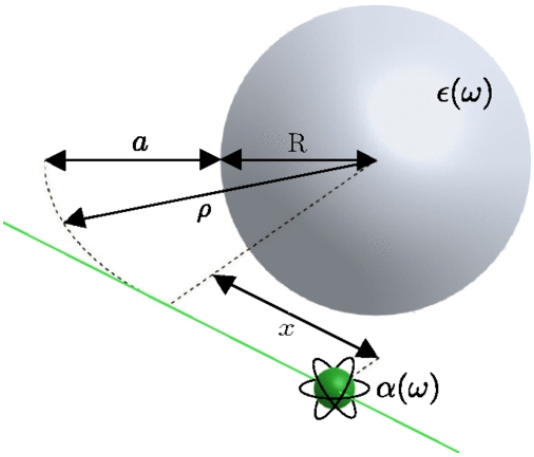

Figure 7.13: Scattering of a particle at a sphere of radius R. Trajectory of the particle (green) is distanced by a to the sphere. Taken from [JH16]

In order to reduce the large number of measurements one can use a rotationally symmetric scattering object, such as dielectric spheres [TR11, JH16], as illustrated in Fig. 7.13, or wires [SR15]. By the diffraction on such structure only two measurements (with and without the laser field) remain to be performed. Following this arrangement, a possible method of investigation of the optical properties of unknown particles has been proposed. However, one has to take into account that the reconstructed polarisability is on the imaginary frequency axis. Two resonance peaks on the real frequency axis that are closely together are transformed via Kramers–Kronig relations into one smoothed step at imaginary frequencies. This means that they can not be resolved via this method.

In chapter 6, we presented the results of one matter-wave interference experiment and showed the deviation of the calculated interaction potential from the measured one. We mentioned that the possibility of localised charges results in electric fields, which may explain these deviations. By applying our reconstruction method to this experiment, it should be possible to identify additional potentials by subtracting the calculated Casimir–Polder interaction.

chapter 8

Conclusion and Outlook

We began this work with the difference between the particle and the wave picture which are combined in quantum mechanics via the wave-particle duality. This concept brakes down by observing coherent superpositions of truly macroscopic objects. Thus, matter waves serve as objective evidence for this concept. Matter-wave interference experiments constitute a good starting point for such investigations, because they use the quantum nature of small massive objects in conditions when they behave like waves. In order to find the boundary between both kinds of description the experiments cover different parameters for the matter wave, which are the mass, the volume of the particle, and the velocity. Due to the DE BROGLIE relation, the mass and the velocity enter directly into the wave vector of the matter wave. One assumes that the extension of the particle plays an important role with respect to the quantum nature of the particle. In a quantum mechanical description the particle is coherently spread out over a finite volume. In analogy to wave optics, it can be defined in terms of such quantities as coherence width and length of a molecular beam. Diffraction can only be produced if the scattering object is smaller than the coherence width. Matter-wave experiments are based on this description. In order to enlarge the diffracting particles, the number of internal degrees of freedom increase, which results in problems with the preparation of the initial state of the particles, and can couple with the environment leading to decoherence effects. Due to such couplings, a detection of the particle can be performed that results in a localisation of the particle and a decrease of its coherence length. Consequently, the interference pattern will vanish due to the coupling strength.

For this thesis, we restricted ourselves to the diffraction of neutral matter waves at

dielectric objects. This means that the interaction to be considered was the Casimir–Polder force. This is an example of a dispersion force and appears when a neutral, but polarisable particle gets close to a dielectric surface. It originates from the ground-state fluctuations of the electromagnetic field and therefore it can be evaluated using macroscopic quantum electrodynamics.

We started this thesis with an introduction to the scattering process. There, we firstly presented justification of the commonly used eikonal approximation, which means that the particles pass the grating on straight paths and determines how the interaction potential due to the scattering process arises. After that, we illustrated a quantum mechanical method for the estimation of the interference pattern via transverse Wigner functions, which was followed by Kirchhoff's diffraction formula. This describes interference experiments via the superposition of propagation waves, which was used for the evaluation of the interference pattern from the experiment performed with Phthalocyanine.

We presented the quantisation of the electromagnetic field in the presence of dielectric bodies. By assuming that the interaction can be described with electric field-dipole interaction, a spatially dependent energy shift can be obtained, which is the Casimir–Polder potential at zero temperature. At finite temperature, we made the assumption that the particles and the electromagnetic field are in a thermal state. Both potentials are state-of-the-art and are presented in the third chapter.

One aim of this thesis was the estimation of interactions in the concrete experimental situation of interference of the dye molecule Phthalocyanine on nanomechanical gratings built from silicon nitride and amorphous carbon. With respect to the description of the Casimir–Polder force via scattering Green functions, its material dependence can be separated into two parts, the polarisability of the particle and the scattering properties of bodies, which includes their geometric shape and their optical response. The latter contains most of the difficulties, because one needs the frequency dependent solution of the vector Helmholtz equation together with the boundary conditions given by the experimental situation. In order to estimate this, we used the Born series expansion of the scattering dyadic Green function, which we introduced at the end of the third chapter. This expansion is a series with respect to the susceptibility of the dielectric object. Its convergence cannot be determined in general. We derived the local-field corrected Born series expansion, which includes the self-interaction of the considered particles. Here, we concentrated on the first order of this expansion. These calculations we introduced in the fourth chapter and compared the results with data from a matter-wave reflection experiment and with the results of an exact calculation via the Rayleigh expansion. The conclusion was that the method of the local-field

corrected Born series expansion is useful even for materials with a large susceptibility, such as gold. With this method, we found a good description for the geometric shape of the scattering object to derive the scattering Green function.

Because of the short interaction times of the molecules with the grating bars, the particles can reach very small distances. This leads us to consider finite-size effects of the Casimir–Polder force. The extension of the particle is around 1.3 nm, which is in the same order of magnitude as the shortest distance to the grating. Hence, the assumption that the particle can be considered as a point is not valid any more. It led us to consider the particle as a rigid rotor in analogy to classical mechanics which means that the anisotropy of the particle also has to be taken into account. We firstly analysed the behaviour of point particle with an anisotropic polarisability for different orientations and constructed a method to describe such rotational effects. In classical electrodynamics, such extension would be present in higher orders of the multipole momenta. In order to find a model describing these effects, a spatially extended dipole polarisability had to be defined. Therefore, we constructed a normalised spatial density distribution which we multiplied with the dipole polarisability of the molecule. Here, we assumed that each molecule can be embedded into a volume whose shape depends on the molecule. In order to describe a dipole polarisability, we based the volume on the electronic density of the molecule and defined its surface to an accuracy of one permille electrons per cubic Bohr radius. Here, we found an ellipsoidally shaped volume for Phthalocyanine. Due to its compact structure we assumed a Gaussian-distributed density. Estimation of the used parameters was given in chapter five. With respect to this density, we performed a rotational and spatial average over the particle and estimated the influence of the extension of the particles on the Casimir–Polder potential. We applied this method to the special cases of a spherical and ellipsoidal molecule in front of a half-space. We found that the potential can increase by up to forty percent for close distances. Its dependence shows similarities to the consideration of higher momenta. The first correction term scales with an r^{-5}-law, which is equivalent to the behaviour of an induced quadrupole in front of a dielectric half-space [JAC2010]. This relation between the potential for a quadrupole moment and the first order of the correction still has to be shown. With respect to the discussion from chapter four, the Born series expansion has also to be modified to describe extended and rotating particles. Following the first-order Born approach (which we have performed to include the spatial extension of the particle), one finds that this approach is equivalent to a smearing of the source and observation points of the scattering Green function, which led us to insert the spatial density distribution into the Born series expansion. By rewriting their matrix products via a contraction with a fourth rank tensor, the

rotational and spatial average can be performed in general. The result is shown in chapter five. With this method the spatial extension and rotation of the particle can be taken into account for arbitrary geometric shapes of the scattering object. Finally, we presented the influence of such rotational and extension effects on the interference pattern resulting from diffraction at a dielectric sphere.

With the combination of these methods it is possible to calculate the Casimir–Polder interaction of the mentioned experimental situation. The optical response of the scattering objects can be found in the literature [RH97, BF15]. An image of the grating via a scanning tunneling microscope led us to assume a trapezoidal shape of the grating bars, which was included by the local-field corrected Born series expansion to estimate the scattering Green function of the scenarios. By applying a quantum chemistry simulation, the polarisability of the molecule Phthalocyanine for imaginary frequency arguments was obtained. Including the molecules rotation due to the long interaction time of the particles inside the grating, the Casimir–Polder potential can be calculated. The phase shift then results from the integration along straight trajectories of the molecules. With this phase shift the complex transmission function is found and by following Kirchhoff's diffraction formula the expected interference pattern can be estimated and compared with the measurements. The result was a relatively large deviation between the calculations and the measurements - the discrepancy is by a factor of between two and eight, and it is natural to ask about the origin of this deviation.

At first, we take a closer look to the approximations which were performed for the calculation. One point is the used Born approximation that neglects scattering processes inside the macroscopic object. In order to justify this assumption, we compared its result for a well-known situation, where the molecule is in front of a half-space, with its exact solution. Here, we found a deviation of twenty percent, which we afterwards included in the calculations by a scaling factor. Hence, we can confirm the validity of this assumption.

Another point is the enormous number of input parameters that constitute the polarisability of the molecule, the susceptibility of the grating, the grating structure, the rotational parameter of Phthalocyanine and the involved temperatures. The dependency of the temperature is negligible due to the fact that the molecules will not be excited by it. A variation of the moments of inertia will also have a negligible influence on the estimation, because the molecules perform more than one complete rotation during passing the grating. This means that the assumption of a rotational averaged Casimir–Polder potential is justified. The Casimir–Polder force is robust as well with respect to small variations of the geometric structure. These variations are caused

on the one hand by the tilt angles of the grating bar.

In our opinion the largest inaccuracy is caused by the unknown properties of the optical response of the gratings. The silicon nitride gratings have an unknown stoichiometry that results in a wide range of variation of the susceptibility. This is caused by the manufacturing processes of the gratings. Another aspect, which has a large influence on the interference patterns, is the possibility of localised charges inside the grating bars. This does not influence the Casimir–Polder potential, but it means that the interaction is not completely described by the dipole-electric field interaction and the interaction Hamiltonian has to be complemented with the electrostatic forces acting between the grating and the particle. This argument is based on experimental results in accordance with other investigations on the dielectric properties of silicon nitride depending on the wafer growth process [S95] and on the charging of wafers after their treatment with a focused ion beam [YL08]. Further investigations are needed to confirm these results. This could be a measurement of the charge density, which yields difficulties due to the small structure of the gratings. An exchange of the material of the gratings to conductive materials results in a decrease of the electrostatic potential, whereas it goes hand in hand with an increase of the Casimir–Polder interaction, that supplies decoherence effects and yields a vanishing of the interference pattern. Another option would be a more precise analysis of the interference pattern in such a way that an estimation of the interaction potential can be determined from the measurements. Due to the additivity of the interaction potentials, they can be separated into the different contributions via their different power-laws.

The last part of this thesis was dedicated to the reconstructive estimation of the interaction potentials based on the measured interference patterns. We followed the descriptions for the estimation of the interference patterns introduced in the second chapter - Kirchhoff's diffraction formula. This method is commonly used for the analysis of the interference pattern. By applying a rotation of the grating, the estimation of the spatial dependency of the phase shift is equivalent to a Radon transformation of the potential landscape, which is a consequence of the eikonal approximation. The important aspect of this theory is the calculation of the square of the absolute value of the amplitude of the wave which causes a loss of phase information. Hence, an estimation of the properties of the wave can only be performed up to an arbitrary phase, which includes most of the properties which we want to estimate. This yields the task that a measurement method has to be developed which lets us estimate the phase distribution. Inspired by electromagnetic waves, one finds the Hartmann–Shack sensor solving this task. In analogy to this method, we propose a measuring process performing the same task for matter waves by an exchange of the optical lenses with standing laser fields

which act on the particles in a similar way. Therefore, we call this method Hartmann–Shack sensor for matter waves, and its principle and realisation are presented in the seventh chapter. By repeating the measurements with this sensor the phase distribution of the matter wave in front of the screen can be estimated. Together with the measurements of the amplitude the complete wave can be constructed. Reducing the phase by the geometric phase of the interferometer, the transmission function can be obtained in the far-field regime by applying the inverse Fourier transform to this reduced wave. It results in an interaction potential integrated along the trajectories of the particles. This method implies a second measurement and results directly in the marginal potential. Even by performing one such measurement, one finds the complete interaction between the particle and the scattering object. Therefore, a separation of the potential with respect to different power-laws can be made. Hence, parts of the electrostatic interaction can be determined.

This method proposes additional investigation instruments to estimate the unknown properties of the matter-wave interference experiments. In combination with the rotation of the scattering object even the complete spatial dependency of the interaction can be determined. A consequence of this separation is that the complete Casimir–Polder potential is available. With the assumption that the interaction is not limited to the retarded or non-retarded regimes, which is mostly satisfied, an estimation of the scalar polarisability of the particle can follow. This is shown at the end of the seventh chapter. If the dyadic scattering Green function is known, which can be achieved by a numerical solution of the Helmholtz equation, e.g. with scuff-em [SC], the anisotropy of the polarisability can be approximated and with investigations on different scattering objects the complete dyadic polarisability can be determined via different weights for the rotational average. Otherwise this method can also be applied to investigations of the scattering object. The introduced method for the estimation of the polarisability can be adopted for a determination of the trace of the scattering Green function. Analogously, its anisotropic diagonal elements can be approximated by diffraction of different anisotropic particles. These methods open a wide range of applications and investigation methods.

In conclusion, the methods developed here help in the understanding of matter-wave experiments which themselves are designed to improve our comprehension of quantum mechanics. All of this thesis deals with coherent interference patterns, but the methods can also be applied to investigation of decoherence effects. Interference patterns that consist of coherent and incoherent parts can be analysed due to the separation described here, and the decoherence rate can be compared with the interaction energy, which should define a measure for the decoherence.

appendix A

Dielectric function for carbon

The modulation of the dielectric susceptibility of the amorphous carbon grating (graphite grating) ensued the established model from [RH97]. This model is separated into two parts: the one representing the electric transitions and a second one describing the vibrational transitions, which is a LORENTZ model and reads as [RH97]

$$\varepsilon(\omega) = \varepsilon_\infty + \frac{S\omega_T^2}{\omega_T^2 - \omega^2 - i\Gamma\omega}\,, \tag{A.1}$$

where the oscillator strength S, the phonon frequency ω_T, the phenomenological damping constant Γ and the dielectric function ε_∞ depend on the orientation of the electromagnetic field, parallel ($\parallel$) and perpendicular ($\perp$). The corresponding parameters are tabled in Table A.1. The dielectric function ε_∞ determines the electric transitions and are based on experimental measurements Tables A.2-A.4. The LORENTZ model with the corresponding parameters S, Γ, ω_T describes the motion of the phonons.

orientation	S	ω_T [rad/s]	Γ [rad/s]	ε_∞
$\parallel$	0.004	$1.634 \cdot 10^{14}$	$1.89 \cdot 10^{8}$	5.78
$\perp$	0.031	$2.99 \cdot 10^{14}$	$5.65 \cdot 10^{8}$	$\varepsilon_\infty(\omega)$

Table A.1: Parameter for the dielectric function for amorphous carbon, depending on the orientation: S denotes the oscillator strength, ω_T the phonon frequency, Γ the damping constant. The dielectric constant ε_∞ is a real constant for parallel. Whereas for perpendicular it depends on the inter- and intraband electronic transitions. See App. A.

ω [eV]	$n_\parallel$	$k_\parallel$	$n_\perp$	$k_\perp$	ω [eV]	$n_\parallel$	$k_\parallel$	$n_\perp$	$k_\perp$
40	0.91	0.3	0.75	0.1	23	0.95	0.28	0.41	0.6
39.5	0.89	0.29	0.75	0.1	22.5	0.93	0.28	0.4	0.66
39	0.88	0.28	0.75	0.1	22	0.91	0.29	0.41	0.7
38.5	0.86	0.27	0.74	0.1	21.5	0.88	0.31	0.43	0.76
38	0.85	0.26	0.74	0.1	21	0.84	0.33	0.45	0.82
37.5	0.85	0.26	0.72	0.1	20.5	0.81	0.35	0.51	0.92
37	0.85	0.27	0.72	0.1	20	0.77	0.38	0.55	1.01
36.5	0.85	0.27	0.72	0.1	19.5	0.74	0.42	0.58	1.05
36	0.84	0.28	0.71	0.1	19	0.71	0.47	0.58	1.07
35.5	0.85	0.3	0.7	0.1	18.5	0.71	0.51	0.58	1.1
35	0.86	0.31	0.68	0.1	18	0.77	0.53	0.58	1.12
34.5	0.88	0.33	0.68	0.1	17.5	0.85	0.56	0.58	1.15
34	0.89	0.34	0.67	0.12	17	0.92	0.6	0.61	1.25
33.5	0.9	0.35	0.67	0.12	16.5	0.99	0.65	0.75	1.36
33	0.91	0.36	0.66	0.12	16	1.05	0.68	0.98	1.63
32.5	0.92	0.36	0.66	0.12	15.5	1.1	0.71	1.09	1.92
32	0.93	0.37	0.64	0.13	15	1.1	0.69	1.33	2.15
31.5	0.94	0.37	0.61	0.13	14.5	1.1	0.91	1.84	2.25
31	0.95	0.38	0.6	0.14	14	1.06	0.48	2.31	1.5
30.5	0.97	0.38	0.58	0.16	13.5	1.02	0.34	2.72	1.03
30	0.99	0.39	0.57	0.16	13	1.02	0.33	2.67	0.83
29.5	1.01	0.4	0.55	0.17	12.5	1.04	0.37	2.48	0.7
29	1.02	0.4	0.52	0.19	12	1.06	0.42	2.25	0.63
28.5	1.04	0.39	0.49	0.21	11.5	1.05	0.47	2.03	0.58
28	1.05	0.38	0.47	0.24	11	1.03	0.52	1.81	0.57
27.5	1.06	0.37	0.45	0.27	10.5	1.02	0.53	1.65	0.53
27	1.07	0.35	0.46	0.31	10	0.98	0.5	1.52	0.46
26.5	1.06	0.33	0.47	0.35	9.5	1.01	0.39	1.38	0.37
26	1.05	0.32	0.48	0.38	9	1.05	0.29	1.25	0.27
25.5	1.03	0.31	0.47	0.43	8.5	1.1	0.2	1.1	0.18
25	1.02	0.3	0.47	0.47	8	1.15	0.12	0.96	0.15
24.5	1	0.29	0.46	0.51	7.5	1.18	0.06	0.82	0.2
24	0.99	0.28	0.46	0.54	7	1.2	0.03	0.65	0.44
23.5	0.97	0.28	0.44	0.56	6.5	1.23	0.01	0.66	0.84

Table A.2: Parameter for the dielectric function for graphite [RH97] Part I.

ω [eV]	$n_\parallel$	$k_\parallel$	$n_\perp$	$k_\perp$	ω [eV]	$n_\parallel$	$k_\parallel$	$n_\perp$	$k_\perp$
6	1.27	0.02	0.94	1.35	1.8	0	0	2.96	1.81
5.5	1.31	0.04	1.25	1.85	1.7	0	0	3.01	1.84
5	1.46	0.71	1.39	2.48	1.6	0	0	3.06	1.86
4.9	1.44	0	1.66	2.56	1.5	0	0	3.1	1.9
4.8	1.43	0	1.95	2.65	1.4	0	0	3.14	1.95
4.7	1.42	0	2.18	2.64	1.3	0	0	3.2	2.02
4.6	1.41	0	2.38	2.54	1.2	0	0	3.25	2.07
4.5	1.4	0.84	2.53	2.41	1.16	0	0	3.33	2.07
4.4	1.4	0	2.64	2.26	1.12	0	0	3.19	2.07
4.3	1.39	0	2.71	2.1	1.08	0	0	3.16	2.17
4.2	1.38	0	2.75	1.94	1.04	0	0	3.16	2.28
4.1	1.37	0	2.75	1.79	1	0	0	3.18	2.4
4	1.37	0.83	2.73	1.66	0.9	0	0	3.39	2.7
3.9	1.36	0	2.69	1.56	0.8	0	0	3.69	2.91
3.8	1.36	0	2.66	1.49	0.7	0	0	3.94	3.02
3.7	1.36	0	2.64	1.43	0.6	0	0	4.24	3.25
3.6	1.36	0	2.63	1.39	0.5	0	0	4.5	3.41
3.5	1.36	0.69	2.62	1.36	0.4	0	0	4.83	3.82
3.4	1.35	0	2.62	1.33	0.3	0	0	5.36	4.48
3.3	1.35	0	2.61	1.31	0.2294	0	0	5.866	5.124
3.2	1.35	0	2.61	1.29	0.2232	0	0	5.923	5.217
3.1	1.35	0	2.62	1.29	0.217	0	0	6	5.318
3	1.35	0.62	2.32	1.28	0.2108	0	0	6.07	5.42
2.9	1.35	0	2.63	1.28	0.2046	0	0	6.129	5.52
2.8	1.36	0	2.63	1.28	0.2002	0	0	6.15	5.597
2.7	1.36	0	2.64	1.28	0.1996	0	0	6.145	5.611
2.6	1.36	0	2.64	1.3	0.199	0	0	6.135	5.627
2.5	1.36	0.64	2.65	1.31	0.1984	0	0	6.12	5.656
2.4	1.36	0	2.66	1.33	0.1977	0	0	6.097	5.721
2.3	1.36	0	2.67	1.34	0.1971	0	0	6.131	5.948
2.2	1.36	0	2.68	1.36	0.197	0	0	6.212	6.036
2.1	1.37	0	2.7	1.39	0.1969	0	0	6.378	6.094
2	0	0.72	2.86	1.73	0.1967	0	0	6.59	6.016
1.9	0	0	2.91	1.77	0.1966	0	0	6.687	5.813

Table A.3: Parameter for the dielectric function for graphite [RH97] Part II.

ω [eV]	$n_\parallel$	$k_\parallel$	$n_\perp$	$k_\perp$	ω [eV]	$n_\parallel$	$k_\parallel$	$n_\perp$	$k_\perp$
0.1965	0	0	6.46	5.644	0.1085	2.353	3.7	0	0
0.1959	0	0	6.371	5.498	0.1084	2.345	4.15	0	0
0.1952	0	0	6.291	5.515	0.1082	2.334	5.92	0	0
0.1946	0	0	6.258	5.53	0.1081	2.317	0.00911	0	0
0.1922	0	0	6.217	5.56	0.108	2.291	0.015	0	0
0.186	0	0	6.205	5.6	0.1079	2.241	0.033	0	0
0.1798	0	0	6.238	5.663	0.1077	2.124	0.108	0	0
0.1736	0	0	6.323	5.775	0.1076	2.196	0.75	0	0
0.1674	0	0	6.476	5.955	0.1075	2.735	0.166	0	0
0.1612	0	0	6.712	6.218	0.1074	2.587	0.042	0	0
0.16	0	0	6.77	6.29	0.1071	2.496	0.01	0	0
0.14	0	0	6.91	6.63	0.1069	2.465	0.00451	0	0
0.12	0	0	6.96	7.38	0.1066	2.45	0.00252	0	0
0.1165	2.399	3e-05	0	0	0.1054	2.424	0.00049	0	0
0.1153	2.398	4.05	0	0	0.1041	2.417	0.000201	0	0
0.1141	2.397	5.75	0	0	0.1	2.41	4.08e-05	7.14	8.75
0.1128	2.395	8.1e-05	0	0	0.08	2.406	3.08e-06	7.68	10.8
0.1115	2.393	0.000151	0	0	0.06	2.405	9.77e-07	8.86	14.02
0.1103	2.388	0.000319	0	0	0.04	2.405	4.17	11.75	20
0.1091	2.374	0.00106	0	0	0.02	2.404	1.65e-07	22.42	33.49

Table A.4: Parameter for the dielectric function for graphite [RH97] Part III.

Bibliography

[EA1873] E. Abbe. *Archiv für mikroskopische Anatomie* **9**, 413 (1873).

[AT77] D.L. Andrews, T. Thirunamachandran. *J. Chem. Phys.* **67**, 5026 (1977).

[MA99] M. Arndt, O. Nairz, J. Vos-Andreae, C. Keller, G. van der Zouw, A. Zeilinger. *Nature* **401**, 680 (1999).

[HHB84] H.H. Barrett. *The Radon transform and its applications.* In: Wolf, E. Progress in Optics, Vol. XXI, Elsevier (1984).

[BS08] H. Behnke, F. Sommer. *Theorie der analytischen Funktionen einer komplexen Veränderlichen.* Springer Berlin, Heidelberg, (2008).

[HB14] H. Bender, C. Stehle, C. Zimmermann, S. Slama, J. Fiedler, S. Scheel, S.Y. Buhmann, V.N. Marachevsky. *Phys. Rev. X* **4**, 011029 (2014).

[EB06] E. Betzig, G.H. Patterson, R. Sougrat, O.W. Lindwasser, S. Olenych, J.S. Bonifacino, M.W. Davidson, J. Lippincott-Schwartz, H.F. Hess. *Science* **313**, 1642 (2006).

[BW99] M. Born and E. Wolf. *Principles of optics: Electromagnetic theory of propagation, interference and diffraction of light*, Cambridge University Press (1999).

[RNB96] R.N. Bracewell. *The Fourier transform and its applications*, McGraw-Hill, New York (1986).

[BF15] C. Brand, J. Fiedler, T. Juffmann, M. Sclafani, C. Knobloch, S. Scheel, Y. Lilach, O. Cheshnovsky, M. Arndt. *Ann. Phys. (Berlin)* **527**, 580 (2015).

[CB16] C. Brand *private communications.*

[BB02] B. Brezger, L. Hackermüller, S. Uttenthaler, J. Petschinka, M. Arndt, A. Zeilinger. *Phys. Rev. Lett.* **88**, 100404 (2002).

[LdB1923] L. de Broglie. *Nature* **112**, 540-540 (1923).

[SYB12-I] S.Y. Buhmann. *Dispersion Forces I: Macroscopic quantum electrodynamics and ground-state Casimir, Casimir–Polder and van der Waals forces*, Springer Heidelberg (2012).

[SYB12-II] S.Y. Buhmann. *Dispersion Forces II: Many-Body Effects, Excited Atoms, Finite Temperature and Quantum Friction*, Springer Heidelberg (2012).

[BS12] S.Y. Buhmann, S. Scheel, S.Å. Ellingsen, K. Hornberger, A. Jacob. *Phys. Rev. A* **85**, 042513 (2012).

[CS1991] O. Carnal, M. Sigel, T. Sleator, H. Takuma, J. Mlynek. *Phys. Rev. Lett.* **67**, 3231 (1991).

[HC1948] H.B.G. Casimir. *Proc. K. Ned. Akad. Wet.* **51**, 793 (1948).

[CP1948] H.B.G. Casimir, D. Polder. *Phys. Rev.* **73**, 360 (1948).

[CC07] C. Cerjan. *J. Opt. Soc. Am. A* **6**, 1609-1616 (2007).

[WCC95] Weng Cho Chew. *Waves and Fields in Inhomogeneous Media*, IEEE Press (1995).

[AC10] A.M. Contreras-Reyes, R. Guérout, P.A.M. Neto, D.A.R. Dalvit, A. Lambrecht, S. Reynaud. *Phys. Rev. A* **82**, 052517 (2010).

[ADC2009] A.D. Cronin, J. Schmiedmayer, D.E. Pritchard. *Rev. Mod. Phys.* **81**, 1051-1129 (2009).

[JAC2010] J.A. Crosse, S.Å. Ellingsen, K. Clements, S.Y. Buhmann, S. Scheel. *Phys. Rev. A* **82**, 010901(R) (2010).

[DG1927] C. Davisson, L.H. Germer. *Nature* **119**, 558-560 (1927).

[DG27] C. Davisson, L. H. Germer. *Phys. Rev.* **30**, 705 (1927).

[HTD98] H.T. Dung, L. Knöll, D.G. Welsch. *Phys. Rev. A* **57**, 3931 (1998).

[SE13] S. Eibenberger, S. Gerlich, M. Arndt, M. Mayor, J. Tüxen. *Phys. Chem. Chem. Phys.* **15**, 14696 (2013).

[AE1905] A. Einstein. *Ann. Physik* **17**, 132-148 (1905).

[ERKD09] R. Erni, M.D. Rossell, C. Kisielowski, U. Dahmen, *Phys. Rev. Lett.* **102**, 096101 (2009).

[OS30] I. Estermann, O. Stern. *Zeitschrift für Physik* **61**, 95 (1930).

[JF99] J.A. Ferrari, D. Perciante, A. Dubra. *J. Opt. Soc. Am. A* **10**, 2581-2582 (1999).

[FS15] J. Fiedler, S. Scheel. *Ann. Phys. (Berlin)* **527**, 570 (2015).

[FS17] J. Fiedler, W.H. Broer, S. Scheel. *J. Phys. B: At. Mol. Opt. Phys.* **50**, 155501 (2017).

[SG07] S. Gerlich, L. Hackermüller, K. Hornberger, A. Stibor, H. Ulbricht, M. Gring, F. Goldfarb, T. Savas, M. Müri, M. Mayor, M. Arndt. *Nat. Phys.* **3**, 711 (2007).

[JWG68] J.W. Goodman. *Introduction to Fourier Optics*, McGraw-Hill Book company (1968).

[REG2000] R.E. Grisenti, W. Schöllkopf, J.P. Toennies, G.C. Hegerfeldt, T. Kohler, M. Stoll. *Phys. Rev. Lett.* **85**, 2284 (2000).

[HP1936] H. v. Halban Jnr., P. Preiswerk. *C.R. Acad. Sci. Paris* **203**, 73-75 (1936).

[HCH37] H.C. Hamaker. *Physica* **4**, 1058 (1937).

[JH1900] J. Hartmann. *Zeitschrift für Instrumentenkunde (Berlin)* **20**, 17-27, 47-58 (1900).

[FH10] F. Hasselbach. *Rep. Prog. Phys.* **73**, 016101 (2010).

[JH16] J.L. Hemmerich, R. Bennett, T. Reisinger, S. Nimmrichter, J. Fiedler, H. Hahn, H. Gleiter, S.Y. Buhmann. *Phys. Rev. A* **94**, 023621 (2016).

[HH1887] H. Hertz. *Ann. Phys.* **267**, 983 (1887).

[WH10] W.F. Holmgren, M.C. Revelle, V.P.A. Lonij, A.D. Cronin. *Phys. Rev. A* **81**, 053607 (2010).

[JH58] J.J. Hopfield. *Phys. Rev.* **112**, 1555 (1958).

[KH09] K. Hornberger, S. Gerlich, H. Ulbricht, L. Hackermüller, S. Nimmrichter, I.V. Goldt, O. Boltalina, M. Arndt. *New J. Phys.* **11**, 043032 (2009).

[RH97] R.E. Hummel, P. Wibmann. *Handbook of optical properties*, CRC Press (1997).

[HB92a] B. Huttner, S.M. Barnett. *Phys. Rev. A* **46**, 4306 (1992).

[HB92b] B. Huttner, S.M. Barnett. *Europhys. Lett.* **18**, 487 (1992).

[JDJ02] J.D. Jackson. *Klassische Elektrodynamik*, 3th edition, Walter de Gruyter (2002).

[JUA13] T. Juffmann, H. Ulbricht, M. Arndt. *Rep. Prog. Phys.* **76**, 086402 (2013).

[TJ12] T. Juffmann, A. Millic, M. Mullneritsch, P. Asenbaum, A. Tsukernik, J. Tüxen, M. Mayor, O. Cheshnovsky, M. Arndt. *Nature Nanotechnology* **7**, 297 (2012).

[TJ10] T. Juffmann, S. Nimmrichter, M. Arndt, H. Gleiter, K. Hornberger. *Found. Phys.* **42**, 98 (2010).

[KS88] A.C. Kak, M. Slaney. *Principles of computerized tomographic imaging*, IEEE Press, New York (1988).

[KS1988] D.W. Keith, M.L. Schattenburg, H.I. Smith, D.E. Pritchard. *Phys. Rev. Lett.* **61**, 1580 (1988).

[LK01] L. Knöll, S. Scheel, D.-G. Welsch. *QED in dispersing and absorbing media*, in *Coherence and Statistics of Photons and Atoms*, ed. J. Piřina, Wiley, New York (2001).

[LL69] L.D. Landau, E.M. Lifschitz. *Mechanics. Vol. 1*, Pergamon Press (1969).

[AM14] A. Messiah. *Quantum Mechanics*, Dover Books on Physics (2014).

[NH08] S. Nimmrichter and K. Hornberger. *Phys. Rev. A* **78**, 023612 (2008).

[EP85] E.D. Palik. *Handbook of Optical Constants of Solids*, Academic Press, Inc. (1985).

[PN09] D.F. Parsons, B.W. Ninham. *J. Phys. Chem. A* **113**, 1141 (2009).

[JDP05] J.D. Perreault, A.D. Cronin, T.A. Savas. *Phys. Rev. A* **71**, 053612 (2005).

[JDP06] J.D. Perreault, A.D. Cronin. *Phys. Rev. A* **73**, 033610 (2006).

[MP1900] M. Planck. *Verhandlungen der Deutschen Physikalischen Gesellschaft* **2**, 237-245 (1900).

[PG90] A. Piccirillo, A.L. Gobbi. *J. Electrochem. Soc.* **137**, 3910 (1990).

[JR17] J. Radon. *Berichte der Sächsischen Akademie der Wissenschaft - Math.-phys. Klasse* **69**, 262-277 (1917).

[RS09] R. Ramprasad, N. Shi. *Appl. Phys. Lett.* **88**, 222903 (2006).

[TR11] T. Reisinger, G. Bracco, B. Holst. *New J. Phys.* **13**, 065016 (2011).

[LR00] L.C.G. Rogers, D. Williams. *Diffusions, Markov Processes, and Martingales*, Cambridge University Press, Cambridge (2000).

[MER95] M.E. Rose. *Elementary Theory of Angular Momentum*, John Wiley & Sons (1995).

[ER32] E. Ruska. *Zeitschrift für Physik* **78**, 318 (1932).

[KS15] K. Sander, C. Peltz, C. Varin, S. Scheel, T. Brabec, T. Fennel. *J. Phys. B: At. Mol. Opt. Phys.* **48**, 204004 (2015).

[S95] T.A. Savas, S.N. Shah, M.L. Schattenburg, J.M. Carter, H.I. Smith. *J. Vac. Sci. Technol. B* **13**, 2732 (1995).

[BS70] B.H. Schechtman, W.E. Spicer. *Journal of molecular spectroscopy* **33**, 28-48 (1970).

[SB08] S. Scheel and S.Y. Buhmann. *Acta Physica Slovaca* **58**, 675 (2008).

[SB02] W. Schlegel, J. Bille. *Medizinische Physik 2*, Springer (2002).

[WS01] W.P. Schleich. *Quantum Optics in Phase Space*, Wiley-VCH (2001).

[SR15] G. Schütz, A. Rembold, A. Pooch, H. Prochel, A. Stibor. *Ultramicroscopy* **158**, 65 (2015).

[MS13] M. Sclafani. *Dissertation: Molecular beam methods for quantum optics experiments: sources, detection schemes and coherent manipulation.* University of Vienna (2013).

[SC] SCUFF-EM, `http://homerreid.com/scuff-EM`.

[SP71] R.V. Shack, B.C. Platt. *J. Opt. Soc. Am.* **61**, 656-660 (1971).

[DAS09] D.A. Steck. *Rubidium 87D Line Data*, http://steck.us/alkalidata (2009).

[SH15] B.A. Stickler, K. Hornberger. *Phys. Rev. A* **92**, 023619 (2015).

[VBS08] V.B. Svetovoy, P.J. van Zwol, G. Palasantzas, J.Th.M. De Hosson. *Phys. Rev. B* **77**, 035439 (2008).

[HTD03] H. Trung Dang, S.Y. Buhmann, L. Knöll, D.-G. Welsch, S. Scheel, J. Kästel. *Phys. Rev. A* **68**, 043816 (2003).

[Turb] University of Karlsruhe and Forschungszentrum Karlsruhe GmbH, *TURBOMOLE*, (2010).

[VW06] W. Vogel, D.-G. Welsch. *Quantum Optics*, Wiley-VCH (2006).

[SH08] V. Westphal, S.O. Rizzoli, M.A. Lauterbach, D. Kamin, R. Jahn, S.W. Hell. *Science* **320**, 246-249 (2008).

[EPW1932] E.P. Wigner. *Phys. Rev.* **40**, 749 (1932).

[WM1989] W.E. Moerner, L. Kador. *Phys. Rev. Lett.* **62**, 2535 (1989).

[YL08] S. Yogev, J. Levin, M. Molotskii, A. Schwarzmann, O. Avayu, Y. Rosenwaks. *J. Appl. Phys.* **103**, 064107 (2008).

[TY1807] T. Young. *Lectures on Natural Philosophy* **1** (1807).

[DWZ02] D.W. Zhang, X.-C. Yuan, N.Q. Ngo, P. Shum. *Opt. Express* **12**, 521-525 (2002).